

# DYNAMICS OF QUASI-THREE DIMENSIONAL AND TWO-PHASE MASS FLOWS

DISSERTATION  
SUBMITTED FOR THE  
PARTIAL FULFILLMENT OF THE REQUIREMENT FOR  
THE MASTER OF PHILOSOPHY (M. Phil.) DEGREE  
IN MATHEMATICS

BY

PARAMESHWARI KATTEL



DEPARTMENT OF NATURAL SCIENCES  
SCHOOL OF SCIENCE  
KATHMANDU UNIVERSITY, DHULIKHEL, KAVRE, NEPAL  
FEBRUARY, 2014

# Dedication

.....to my parents

Bimala Kattel

*and*

Ishwari Prasad Kattel

## Certificate by the Supervisors

The dissertation entitled **Dynamics of Quasi-Three-Dimensional and Two-Phase Mass Flows** presented by Parameshwari Kattel under our supervision is hereby submitted for the partial fulfillment of the Master of Philosophy (M. Phil.), degree in Mathematics to the Department of Natural Sciences, School of Science, Kathmandu University, Dhulikhel, Kavre, Nepal.

---

Dr. Shiva P. Pudasaini

(Supervisor)

Professor, Kathmandu University

School of Science, Department of Natural Sciences

Dhulikhel, Kavre, Nepal

and

University of Bonn

Faculty of Mathematical and Natural Sciences

Department of Geodynamics and Geophysics

Meckenheimer Allee 176, D-53115 Bonn, Germany.

Date:

---

Dr. Dil B. Gurung

(Co-supervisor)

Associate Professor, Kathmandu University

School of Science, Department of Natural Sciences

Dhulikhel, Kavre, Nepal.

Date:

# Certificate of Approval

This dissertation entitled **Dynamics of Quasi-Three-Dimensional and Two-Phase Mass Flows** is submitted for the partial fulfillment of the Master of Philosophy (M. Phil.) degree in Mathematics to the Department of Natural Sciences, School of Science, Kathmandu University, in February 2014, by Parameshwari Kattel.

## Approved by

---

Dr. Shiva P. Pudasaini

(Supervisor)

Professor, Kathmandu University, School of Science

Department of Natural Sciences, Dhulikhel, Kavre, Nepal and

University of Bonn, Faculty of Mathematical and Natural Sciences

Department of Geodynamics and Geophysics

Meckenheimer Allee 176, D-53115 Bonn, Germany.

Date:

---

Dr. Dil B. Gurung

(Co-supervisor)

Associate Professor, Kathmandu University, School of Science,

Department of Natural Sciences, Dhulikhel, Kavre, Nepal.

Date:

---

Dr. Jyoti Upadhaya

Head of Department, Department of Natural Sciences

Professor, Kathmandu University, School of Science, Dhulikhel, Kavre, Nepal.

Date:

---

Dr. Dal B. Adhikary

(External Examiner)

Professor, Tribhuvan University, Tri-Chandra Multiple Campus, Kathmandu, Nepal

Date:

## Acknowledgements

I would like to express my sincere gratitude to my supervisor Prof. Dr. Shiva P. Pudasaini and co-supervisor and the coordinator of the M. Phil. Programme in Mathematics Assoc. Prof. Dr. Dil B. Gurung, for their continuous support and suggestions for this work. I will ever remain grateful to Prof. Pudasaini for his wonderful lectures during M. Phil. studies, for his motivation and incessant guidance from the inception to the completion of the work.

I would like to express my sincere gratitude to the external examiner Prof. Dr. Dal B. Adhikary for his interest, valuable time, kind support and the suggestions. I would also like to thank all my batch-mates for their company, especially to Mr. Jeevan Kafle, Mr. Khim B. Khattri and Mr. Puskar R. Pokhrel with whom I discussed several aspects related to this work and benefited substantially.

Parameshwari Kattel

Kathmandu University Registration Number: 012661 – 11

## Student's Declaration

I, Parameshwari Kattel, hereby declare that the research work entitled **Dynamics of Quasi-Three-Dimensional and Two-Phase Mass Flows** submitted for the partial fulfillment of the Master of Philosophy (M. Phil.) degree in Mathematics to the Department of Natural Sciences, School of Science, Kathmandu University, Dhulikhel, Kavre in February 2014 is a genuine work which I carried out under the guidance of my supervisors and has not been published or submitted elsewhere for the requirement of any degree. Any literature, data or work done by others cited within this dissertation has been given due acknowledgement and are listed in the Bibliography.

---

Parameshwari Kattel

Batch: 2011

Kathmandu University Registration Number: 012661 – 11

## Abstract

Landslides, debris flows and debris avalanches are large mass movements, and extremely destructive natural hazards that often occur as the motion of the mixture of soil, rock and fluid down mountain slopes. Their occurrence is largely unpredictable. Therefore, the study of their dynamics is important for mountainous countries. So, reliable methods are needed to accurately predict the flow evolution, run-out distances, inundation areas, deposition behavior, impact forces, and the overall dynamics of the flows from inception to its standstill for the prevention measures and mitigation strategies in geo-hazard-prone regions, such as Nepal. To do so, the general two-phase mass flow model presented by Pudasaini (2012) [84] is considered. This model is a comprehensive theory that accounts for strong interactions between the solid and the fluid phases. Besides buoyancy, the model includes three further important and dominant physical aspects of mass flows, such as the enhanced non-Newtonian viscous stress, virtual mass force, and generalized drag. Model equations reveal strong coupling between the solid and fluid momentum transfer, both through interfacial momentum transfer and the enhanced viscous stresses.

Here, new simulation results for three-dimensional and two-phase solid-fluid mixture flows down a slope are presented. The simulation provides, as out-put, the time and spatial evolution of the solid and fluid components, solid or fluid volume fraction, geometrical evolution of the debris mixture as a whole, and the solid and fluid velocities in the flow directions. Simulation results reveal some observable phenomena in real two-phase debris flows, namely, the development of a solid volume fraction dominated strong front surge head followed by a relatively long tail, mainly consisting of the fluid component. Such typical debris flow characteristics are obtained here for the first time for three-dimensional flow configurations with a real two-phase debris flow model for different parameters and physical settings with a high-resolution numerical simulation technique. The results obtained for different physical and material parameters, including the virtual mass coefficient, the drag coefficient, the density ratio and the basal friction angle for effectively two-phase mass flow and the geometrically simple three-dimensional topography, imply that the considered physical-mathematical model, as a set of non-linear PDEs, and simulation strategies, can be applied to a wide range of mass flows. This includes dry granular flows, snow/rock avalanches, and flow of powders/grains in process engineering, as well as debris flows/flash floods, and Glacial Lake Outburst Floods (GLOF) in the Himalaya. This helps in constructing mitigation strategies, land use planning and designing defense measures against natural hazards as well as in enhancing production processes in flows and transportation of mixture materials in industries.

## List of Symbols

$A$	mobility number.
$b$	basal surface of flow.
$C_{DG}$	generalized drag coefficient.
$C$	virtual mass coefficient.
$f$	fluid phase.
$\mathcal{F}$	fluid-like contribution in generalized drag, $C_{DG}$ .
$\mathcal{G}$	solid-like contribution in generalized drag, $C_{DG}$ .
$g$	gravity constant.
$\mathbf{g}$	acceleration due to gravity.
$g^x, g^y, g^z$	components of gravitational acceleration.
$H$	typical height of debris flow.
$h$	debris flow height, $h = h_s + h_f$ .
$h_f$	fluid contribution to flow height, $h_f = \alpha_f h$ .
$h_s$	solid contribution to flow height, $h_s = \alpha_s h$ .
$\mathbf{I}$	identity matrix.
$J$	exponent for linear or quadratic drag.
$K, K_x, K_y$	earth pressure coefficients.
$L$	typical extent of debris flow.
$m_f$	fluid momentum flux, $m_f = \alpha_f h u_f$ .
$m_s$	solid momentum flux, $m_s = \alpha_s h u_s$ .
$\mathbf{M}$	interfacial momentum transfer.
$M$	a parameter depending on Reynolds number.
$N_R$	Reynolds number, $N_R = \sqrt{gL\rho_f H}/\alpha_f \eta_f$ .
$N_{RA}$	quasi-Reynolds number/mobility number.
$p$	fluid pressure.
$\mathcal{P}$	parameter combining solid-like and fluid-like drag contributions.
$p_{bf}$	effective fluid pressure at base.
$p_{bs}$	effective solid pressure at base.
$Re_p$	particle Reynolds number, $Re_p = \rho_f d \mathcal{U}_T / \eta_f$ .

<b>S</b>	shear stress.
<b>S</b>	source terms.
<i>s</i>	solid-phase.
<i>t</i>	time.
<b>T</b>	total stress.
$\mathbf{u}_f$	velocity for fluid, $\mathbf{u}_f = (u_f, v_f, w_f)$ .
$\mathbf{u}_s$	velocity for solid, $\mathbf{u}_s = (u_s, v_s, w_s)$ .
$\mathcal{U}_s$	particle sedimentation velocity.
$\mathcal{U}_T$	particle terminal velocity.
<b>W</b>	vector of conservative variables, $\mathbf{W} = (h_s, h_f, m_s, m_f)^t$ .
$x, y, z$	spatial coordinates.
$\alpha_f$	volume fraction for fluid.
$\alpha_s$	volume fraction for solid.
$\beta_{x_s}, \beta_{y_s}$	lateral hydraulic pressure parameters for solid.
$\beta_{x_f}, \beta_{y_f}$	lateral hydraulic pressure parameters for fluid.
$\gamma$	density ratio, $\gamma = \rho_f / \rho_s$ .
$\delta$	basal friction angle.
$\varepsilon$	aspect ratio, $\varepsilon = H/L$ .
$\zeta$	channel slope angle.
$\eta_f$	fluid viscosity.
$\mu$	basal friction coefficient, $\mu = \tan \delta$ .
$\xi$	vertical distribution of $\alpha_s$ .
$\rho$	debris bulk density.
$\rho_f$	fluid phase density.
$\rho_s$	solid phase density.
$\boldsymbol{\tau}_f$	extra stress for fluid.
$\boldsymbol{\tau}_s$	extra stress for solid.
$\phi$	internal friction angle.
$\chi$	vertical shearing of fluid velocity.
$\nabla$	gradient operator.
$\otimes$	tensor product.

# Publications

## A. Published Papers

1. Kafle, J., Kattel, P., Pokhrel, P. R., Khattri, K. B., Gurung, D. B., Pudasaini, S. P., 2013: Dynamic Interaction Between a Two-Phase Submarine Landslide and a Fluid Reservoir. *Int. J. Lslid. Env.* 1(1), 35-36.
2. Kattel, P., Kafle, J., Khattri, K. B., Pokhrel, P. R., Gurung, D. B., Pudasaini, S. P., 2013: Dynamics of Three-Dimensional, Two-Phase Landslides and Debris Flows. *Int. J. Lslid. Env.* 1(1), 39-40.
3. Khattri, K. B., Pokhrel, P. R., Kafle, J., Kattel, P., Gurung, D. B., Pudasaini, S. P., 2013: Some New Insights into the Fluid Flows in Debris Material and Porous Landscape. *Int. J. Lslid. Env.* 1(1), 43-44.
4. Pokhrel, P. R., Khattri, K. B., Kattel, P., Kafle, J., Gurung, D. B., Pudasaini, S. P., 2013: Enhanced Descriptions of Real Two-Phase Landslides and Debris Flows. *Int. J. Lslid. Env.* 1(1), 75-76.

## B. Submitted Papers

1. Kafle, J., Kattel, P., Pokhrel, P. R., Khattri, K. B., Gurung, D. B., Pudasaini, S. P., 2013: Dynamic Interaction Between a Two-Phase Submarine Landslide and a Reservoir.
2. Kattel, P., Kafle, J., Khattri, K. B., Pokhrel, P. R., Gurung, D. B., Pudasaini, S.P., 2013: Dynamic Simulation of Three-dimensional, Two-phase Landslides and Debris Flows.
3. Khattri, K. B., Pokhrel, P. R., Kafle, J., Kattel, P., Gurung, D. B., Pudasaini, S. P., 2013: Fluid Flows in Porous Landscape and Debris Material: Some New Insights.
4. Pokhrel, P. R., Khattri, K. B., Kattel, P., Kafle, J., Gurung, D. B., Pudasaini, S. P., 2013: Real Two-Phase Landslides and Debris Flows: Enhanced Simulations.

## Presentations

1. Kattel, P., 2013: *High-resolution, three-dimensional simulations of real two-phase debris mass flows.*  
In: The DAAD Partnership Activities Workshop organized by Department of Natural Sciences, School of Science, Kathmandu University on “Numerical Methods for Ordinary and Partial Differential equations”, September 2-13, 2013, Kathmandu University, Dhulikhel, Kavre, Nepal.
2. Kafle, J., Kattel, P., Pokhrel, P. R., Khattri, K. B., Gurung, D. B., Pudasaini, S. P., 2013: *Dynamic interaction between a two phase submarine landslide and a fluid reservoir.*  
In: The 11th International Symposium on Mitigation of Geo-disasters in Asia (MGDA-11), 22-28 October, 2013, Kathmandu and Pokhara, Nepal.
3. Kattel, P., Kafle, J., Khattri, K. B., Pokhrel, P.R., Gurung, D. B., Pudasaini, S. P., 2013: *Dynamics of three-dimensional, two phase landslides and debris flows.*  
In: The 11th International Symposium on Mitigation of Geo-disasters in Asia (MGDA-11), 22-28 October, 2013, Kathmandu and Pokhara, Nepal.
4. Khattri, K. B., Pokhrel, P. R., Kafle, J., Kattel, P., Gurung, D. B., Pudasaini, S. P., 2013: *Some new insights into the fluid flows in debris material and porous landscape.*  
In: The 11th International Symposium on Mitigation of Geo-disasters in Asia (MGDA-11), 22-28 October, 2013, Kathmandu and Pokhara, Nepal.
5. Pokhrel, P. R., Khattri, K. B., Kattel, P., Kafle, J., Gurung, D. B., Pudasaini, S. P., 2013: *Enhanced descriptions of real two phase landslides and debris flows.*  
In: The 11th International Symposium on Mitigation of Geo-disasters in Asia (MGDA-11), 22-28 October, 2013, Kathmandu and Pokhara, Nepal.
6. Kafle, J., Kattel, P. , Pokhrel, P. R., Khattri, K. B., Gurung, D. B., Pudasaini, S. P., 2014: *A two-phase, 3D subaerial debris-flow impinging a reservoir: Dynamics of induced tsunami and submarine debris flows.*  
In: The 5th National Conference of Mathematics (NCM-2014), Nepal Mathematical Society, January 28-30, 2014, Surkhet, Nepal.

7. Kattel, P., Kafle, J., Pokhrel, P. R., Khattri, K. B., Gurung, D. B., Pudasaini, S. P., (Best Presentation Award at NMS-2014 Conference), 2014: *Physical-mathematical modeling and high-resolution simulations of a real two-phase, three dimensional debris flow dynamics*.  
In: The 5th National Conference of Mathematics (NCM-2014), Nepal Mathematical Society, January 28-30, 2014, Surkhet, Nepal.
8. Khattri, K. B., Pokhrel, P. R., Kafle, J., Kattel, P., Gurung, D. B., Pudasaini, S. P., 2014: *Some exact and numerical solutions for fluid flows in debris and porous media with sub-diffusive and sub-advective Model*.  
In: The 5th National Conference of Mathematics (NCM-2014), Nepal Mathematical Society, January 28-30, 2014, Surkhet, Nepal.
9. Pokhrel, P. R., Khattri, K. B., Kattel, P., Kafle J., Gurung, D. B., Pudasaini, S. P., 2014: *General phase-eigenvalues for two-phase mass flows and their implications in enhanced simulations*.  
In: The 5th National Conference of Mathematics (NCM-2014), Nepal Mathematical Society, January 28-30, 2014, Surkhet, Nepal.

# List of Figures

1.1	Three different zones describing a complete debris flow dynamics, an example from Daniao debris flow induced by the Typhoon Morakot, Eastern Taiwan: (a) initiation zone, (b) track, and (c) run out zone [114]. . . . .	4
1.2	Dig Tsho Lake in April 2009 in Nepal; the GLOF event of 1985 destroyed the moraine dam [41]. . . . .	6
1.3	Palcacocha Glacial Lake in Peru (photo by Colette Simonds) [103]. . . . .	6
1.4	Formation of moraine-dammed lake in glaciated high mountain and a possible scenario of GLOF due to wave overtopping and erosion [3]. . . . .	7
1.5	Glacial lakes and their potential hazards in Nepal: a) Tsho Rolpa, a moraine-dammed lake, and b) Gokyo Tsho, a glacier dammed lake in November 2007 [29]. . . . .	7
1.6	The view of Seti River in Kharapani, Kaski District, Western Nepal, after the destruction by the debris and mud flow of 5 May, 2012. (Left) During the flood: There were several houses at the left bank of the flow direction of the river. (Right) After the flood: The houses were swept away. The almost fine debris deposit fan is seen on the right. The photo was taken by an unknown picnic boy, provided to us by Ranjan K. Dahal. . . . .	8
1.7	(a) Engineering, and (b) bio-engineering techniques to protect the part of the Prithvi Highway at Krishnabhir, Central Nepal. Before the mitigation measures had been applied on 2003, the recurrent landslide and debris flows used to block the highway for weeks in every Monsoon (rainy) season. (Photo: Field excursion during the symposium, MGDA-11). . . . .	10
1.8	Torrential control and mitigation of a mountain slope and a torrent by check-dams against a torrential flood and debris flows in Ruwa Khola at Tanahu District, west Nepal. (Photo: Field excursion during the symposium, MGDA-11). . . . .	11

2.1	Different rheological models to show the relationship between the shear stress $\tau$ and the shear-rate $\gamma$ . The figure has been reproduced from the Lecture Notes by Pudasaini (2007) [82]. . . . .	15
2.2	Coulomb envelop ( $\tau = c + \sigma \tan \phi$ ), Mohr-circle, and the Mohr-Coulomb failure as the Mohr circle hits the Coulomb strength envelope in the $\sigma - \tau$ plane. This figure has been reproduced from the lecture notes by Pudasaini (2007) [82]. . . . .	20
3.1	<b>a)</b> The two-dimensional NOC scheme with the staggered grid: The staggered averages at $(x_{p\pm 1/2}, y_{q\pm 1/2}, t^{n+1})$ , denoted by “o”, are computed by the averages at $(x_p, y_q, t^n)$ , represented by “•”. <b>b)</b> The two-dimensional NOC scheme and a floor plan of the staggered grid, where the cell $C_{p+1/2, q+1/2}$ consists of four intersecting cells $C_{p,q}$ , $C_{p+1,q}$ , $C_{p+1,q+1}$ and $C_{p,q+1}$ , denoted by $C_{p,q}^{SW}$ , $C_{p+1,q}^{SE}$ , $C_{p+1,q+1}^{NE}$ and $C_{p,q+1}^{NW}$ , respectively. “•” indicates the computed cell center and “□” denotes the center of the intersecting cells. The numerical fluxes are considered as the values across the corresponding faces, East (E), North (N), West (W) and South (S), respectively. (The figure has been reproduced from Pudasaini and Hutter (2007) [89]). . . . .	41
4.1	Simulation set-up and the slope-fitted coordinate system for a three-dimensional and two-phase debris mass moving down an inclined slope. Here, $x, y, z$ are the coordinates along the down-slope, cross-slope and the surface normal directions, respectively, and $\zeta$ is the slope angle. The hemispherical cap indicates the initial debris mass. . . . .	49
4.2	The three-dimensional geometry of the solid, fluid and total debris height at time $t = 0.18$ s after the two-phase debris material is released from a hemispherical cap (Fig. 4.1) that moves down an inclined plane with inclination angle $\zeta = 45^\circ$ , $\gamma = 1100/1500$ , $\mathcal{C} = 0.2$ , $\phi = 35^\circ$ , $\delta = 20^\circ$ , $\mathcal{P} = 0.5$ . It is important to observe that the solid and the fluid components evolve completely differently, both geometrically and dynamically. . . . .	51
4.3	The three-dimensional geometry of the solid, fluid and total debris height at time $t = 0.18$ s after the two-phase debris material is released from a hemispherical cap that moves down an inclined plane with inclination angle $\zeta = 45^\circ$ , $\gamma = 1100/2500$ , $\mathcal{C} = 0.2$ , $\phi = 35^\circ$ , $\delta = 20^\circ$ , $\mathcal{P} = 0.5$ . . . . .	53

4.4	The three-dimensional geometry of the solid, fluid and total debris height at time $t = 0.18$ s after the two-phase debris material is released from a hemispherical cap that moves down an inclined plane with inclination angle $\zeta = 45^\circ$ , $\gamma = 1100/1100$ , $\mathcal{C} = 0.2$ , $\phi = 35^\circ$ , $\delta = 20^\circ$ , $\mathcal{P} = 0.5$ . . . . .	54
4.5	The three-dimensional geometry of the solid, fluid and total debris height at time $t = 0.18$ s after the two-phase debris material is released from a hemispherical cap that moves down an inclined plane with inclination angle $\zeta = 45^\circ$ , $\gamma = 1100/2000$ , $\mathcal{C} = 0.2$ , $\phi = 15^\circ$ , $\delta = 10^\circ$ , $\mathcal{P} = 0.5$ . . . . .	55
4.6	The three-dimensional geometry of the solid, fluid and total debris height at time $t = 0.18$ s after the two-phase debris material is released from a hemispherical cap that moves down an inclined plane with inclination angle $\zeta = 45^\circ$ , $\gamma = 1100/2000$ , $\mathcal{C} = 0.2$ , $\phi = 15^\circ$ , $\delta = 10^\circ$ , $\mathcal{P} = 0.9$ . . . . .	57
4.7	The three-dimensional geometry of the solid, fluid and total debris height at time $t = 0.18$ s after the two-phase debris material is released from a hemispherical cap that moves down an inclined plane with inclination angle $\zeta = 45^\circ$ , $\gamma = 1100/2000$ , $\mathcal{C} = 0.2$ , $\phi = 15^\circ$ , $\delta = 10^\circ$ , $\mathcal{P} = 0.1$ . . . . .	58
4.8	The three-dimensional geometry of the solid, fluid and total debris height at time $t = 0.18$ s after the two-phase debris material is released from a hemispherical cap that moves down an inclined plane with inclination angle $\zeta = 45^\circ$ , $\gamma = 1100/2000$ , $\mathcal{C} = 0.2$ , $\phi = 15^\circ$ , $\delta = 15^\circ$ , $\mathcal{P} = 0.5$ . . . . .	59
4.9	The three-dimensional geometry of the solid, fluid and total debris height at time $t = 0.18$ s after the two-phase debris material is released from a hemispherical cap that moves down an inclined plane with inclination angle $\zeta = 45^\circ$ , $\gamma = 1100/2000$ , $\mathcal{C} = 0.5$ , $\phi = 15^\circ$ , $\delta = 10^\circ$ , $\mathcal{P} = 0.5$ . . . . .	60
4.10	The evolution of the solid-phase at time slices: $t = 0.006$ s, $t = 0.06$ s, $t = 0.12$ s and $t = 0.18$ s after the two-phase debris material is released from a hemispherical cap that moves down an inclined plane with inclination angle $\zeta = 45^\circ$ , $\gamma = 1100/2000$ , $\mathcal{C} = 0.2$ , $\phi = 15^\circ$ , $\delta = 10^\circ$ , $\mathcal{P} = 0.5$ . . . . .	61
4.11	The evolution of the fluid-fluid at time slices: $t = 0.006$ s, $t = 0.06$ s, $t = 0.12$ s and $t = 0.18$ s after the two-phase debris material is released from a hemispherical cap that moves down an inclined plane with inclination angle $\zeta = 45^\circ$ , $\gamma = 1100/2000$ , $\mathcal{C} = 0.2$ , $\phi = 15^\circ$ , $\delta = 10^\circ$ , $\mathcal{P} = 0.5$ . . . . .	63
4.12	The evolution of the total debris mass at time slices: $t = 0.006$ s, $t = 0.06$ s, $t = 0.12$ s and $t = 0.18$ s after the two-phase debris material is released from a hemispherical cap that moves down an inclined plane with inclination angle $\zeta = 45^\circ$ , $\gamma = 1100/2000$ , $\mathcal{C} = 0.2$ , $\phi = 15^\circ$ , $\delta = 10^\circ$ , $\mathcal{P} = 0.5$ . . . . .	64

# Contents

<b>Dedication</b>	<b>ii</b>
<b>Certificate by the Supervisors</b>	<b>iii</b>
<b>Certificate of Approval</b>	<b>iv</b>
<b>Acknowledgements</b>	<b>v</b>
<b>Student’s Declaration</b>	<b>vi</b>
<b>Abstract</b>	<b>vii</b>
<b>List of Symbols</b>	<b>vii</b>
<b>Publications</b>	<b>x</b>
<b>Presentations</b>	<b>xi</b>
<b>List of Figures</b>	<b>xvi</b>
<b>1 Debris Flows: Impact, Mechanics, Counter Measures and Modeling</b>	<b>1</b>
1.1 Different Types of Geophysical Mass Flows . . . . .	1
1.2 Single- and Two-Phase Flows . . . . .	3
1.3 General Aspects of Debris Flows . . . . .	3
1.4 Different Mass Flow Events and Associated Hazards in Nepal . . . . .	4
1.5 Prevention and Mitigation Measures . . . . .	9
1.6 Mechanics of Debris Flows and Their Modeling . . . . .	12
<b>2 Modeling the Dynamics of Real Two-Phase Debris Flows</b>	<b>13</b>
2.1 Rheology Related to Two-Phase Debris Flows . . . . .	13
2.2 Major Advancements in Modeling Geophysical Mass Flows . . . . .	21
2.3 Advancing the Two-Phase Flow Simulation . . . . .	23

2.4	Physical-Mathematical Model for Two-Phase Debris Flows . . . . .	24
2.4.1	A Three-Dimensional, Real Two-Phase Debris Flow Model . . . . .	24
2.4.2	A Velocity-wise Two-Dimensional, Two-Phase Debris Flow Model . . . . .	26
2.5	Some Important Features of the Two-Phase Debris Flow Model Equations . . . . .	29
2.5.1	Inertial Terms . . . . .	29
2.5.2	Source Terms . . . . .	30
2.5.3	Viscous Terms . . . . .	31
2.5.4	Drag Coefficients . . . . .	31
2.5.5	Diffusion of Solid Volume Fraction . . . . .	32
2.5.6	Reduction to Other Relatively Simple Models . . . . .	32
<b>3</b>	<b>High-Resolution Numerical Integrations</b>	<b>36</b>
3.1	Elliptic, Parabolic and Hyperbolic Equations . . . . .	36
3.2	Various Numerical Schemes for Mass Flows . . . . .	37
3.3	Two-Dimensional NOC Schemes . . . . .	39
3.4	2D Shock-Capturing Method Applied to Extended Equations . . . . .	44
<b>4</b>	<b>Numerical Simulations of 3D, Two-Phase Debris Flows</b>	<b>48</b>
4.1	Simulation Set-up and Parameters . . . . .	48
4.2	Simulation Results and Discussion . . . . .	50
4.2.1	Geometry of the Solid, Fluid and the Total Debris Mass . . . . .	50
4.2.2	Effect of the Density Ratio . . . . .	52
4.2.3	Effects of the Friction Parameters . . . . .	55
4.2.4	Influence of Drag . . . . .	56
4.2.5	Influence of the Virtual Mass . . . . .	58
4.2.6	The Phase-Evolution . . . . .	60
<b>5</b>	<b>Summary</b>	<b>66</b>
	<b>Bibliography</b>	<b>77</b>

# Chapter 1

## Debris Flows: Impact, Mechanics, Counter Measures and Modeling

Mass wasting and flows are very important phenomena from process industries to geophysical contexts. The different geophysical mass flows like landslide, debris flows, rock falls, volcanic eruptions and flash floods contribute a lot in the landscape evolution and the geomorphological aspects. At the same time these phenomena may cause tremendous damages to the lives and infrastructures. So, it is very important to understand the dynamics of the mass flows, especially in the geophysical contexts. In this chapter, we introduce some basic concepts of two-phase debris flow, which is considered as a motion of a mixture of solid particles and a viscous fluid. We describe, in brief, mass flow hazards and recent research and mitigation strategies that are in practice world-wide, and particularly, in Nepal. We mainly focus on the dynamics of debris mass flows, and the need of a real two-phase debris flow model for the appropriate descriptions of the dynamics of the flow in three dimensional topographies. We provide an outline on the general aspects of different mass flow events and associated hazards in Nepal, and their mechanics and different modeling aspects.

### 1.1 Different Types of Geophysical Mass Flows

Landslides, snow, ice and rock avalanches, debris flows, mud flows, and rock falls are some common geophysical mass flow events in mountainous regions [89]. Every year, several snow avalanches are formed in the Himalayan range. *The Himalaya* means *the Home of Snow* [Him = snow, Alaya = home]. The Himalayan mountains are at adequate height, and they contain enough snow blanket, providing perfect conditions for rapidly cascading spectacular, but also very dangerous, snow avalanches [89]. Generally, the motion of snow

and ice, soil or rock down mountain sides are called avalanches if water does not play a crucial role as its triggering factor. However, if water is the triggering element of the soil motion, then, the event is called a debris flow [89].

Mud flows are the flows of soil and added debris which is substantially mixed with interstitial fluid. Mud flows are generally formed when the stagnant soil is soaked with water during heavy rainfall, e.g., during the Monsoon season, and then breaks loose [89]. Mud flows can also happen in water swollen rivers in which the bed breaks loose and develops into a devastating sediment transport [84]. Volcanic eruptions often generate spectacular avalanching debris of pyroclastic material, which is very hot and consists of fragmented rocks and also fine particles. They are typically called pyroclastic debris flows. Lahar is a muddy debris flow, or mud flow, which is a mixture of fine pyroclastic particles and fluid, mainly water. So, lahar flows are associated with the volcanic eruptions and when the erupted material is mixed with ice, snow, or water, the volcanic debris flow becomes lahar. The lahar flow events are common in volcanically active areas, e.g, in Indonesia, the Philippines, and Japan [89]. Such geophysical mass flows as landslides, snow, ice and rock avalanches, debris flows, mud flows, and rock falls are observed in nature in a very wide range of length scale: up to  $10^{10}$  to  $10^{12}$  m<sup>3</sup> of material and  $250 \text{ kmh}^{-1}$  in speed [30, 35, 59, 74, 89, 93].

Although the landslides, snow and rock avalanches, debris flows, mud flows, mud floods, and flash floods are very common natural catastrophic events in the Himalayan range, these events and their associated dynamics, and impacts to the society are very poorly investigated. Similarly, the development and applications of the mitigation measures are also in their infancy. On the other hand, recent records clearly indicate that the economically important, touristic and mountaineering attractions, the high Himalayan regions, are increasingly prone to catastrophic snow avalanches, landslides, debris flows, and rock-falls [7]. Similarly, the monsoon and torrential rain storms are increasing, resulting in devastating landslides and floods as witnessed in the West of Nepal, and the North-West of India in the Monsoon of 2013<sup>1,2</sup>. This undoubtedly demands for more advanced scientific research in understanding the initiation mechanics of these events, their complex flow dynamics, impacts to the society and civil structures, and also the design, development and application of appropriate mitigation measures, hazard mappings and planning in the Himalayan range. The fundamental understanding of the flow dynamics is an important aspect in this direction, and that this work may provide some advancements.

---

<sup>1</sup>[www.abc.net.au/news/2013-06-18/...india-monsoon-floods/4763808](http://www.abc.net.au/news/2013-06-18/...india-monsoon-floods/4763808).

<sup>2</sup>[floodlist.com/asia/nepal-July-2013-update](http://floodlist.com/asia/nepal-July-2013-update).

## 1.2 Single- and Two-Phase Flows

Generally, geo-physical mass flows can be categorized into *(i)* single-phase flows, and *(ii)* multi-phase flows. Under natural conditions, the earth materials are always mixtures of a loose solid phase, a liquid and/or a gas. If the interstitial fluid does not play a significant role in the transportation of momentum, such flows can be considered as single-phase flows. Snow avalanches, landslides and rockfalls are some examples of single-phase flows. When the amount of the interstitial fluid is not negligible in comparison to that of the solids, the interaction between the fluid and the solid phases in the mixture is significant [74, 89]. The fluid can play an important role as the triggering factor for the flow of solid phase, e.g., by weakening the cohesive forces between the solid particles, or by reducing the shear strength of the material [44, 45, 74, 93, 94]. This results in the detachment of the saturated landmass, that later in the course of deformation and motion, with sufficient mixing with the fluid, turns into a debris flow, or debris floods.

Although the dynamics of dense flow avalanches and debris flows in many situations can sufficiently be described by a single phase continuum, the flows like water saturated debris flows and mud flows must be described by a two-phase model of solids and water [74, 75, 83, 89]. The dilute particle laden motion of powder snow avalanches or a subaquatic turbidity current can equally be describable by a two-phase model of turbulent flow of air or water with suspended solid particles. Gravity driven shear flows in powder snow avalanche and pyroclastic flows often comprises a combination of a lower layer of dense granular flow overlain by a turbulent two-phase flow of a dusty cloud [89, 120].

## 1.3 General Aspects of Debris Flows

When loose masses of sediment saturated with water get agitated, due to some instability, e.g., instability directly related to steep topographical and bioclimatic gradients, past bioclimatic-induced instability and morphotectonic-induced instability, they might flow down-slope in response to the gravity; a phenomenon known as debris flow [26, 40, 44, 74, 94]. The fact that distinguishes debris flow from other related phenomena such as rock avalanches and sediment-laden water floods is that in debris flow, both solid and fluid forces significantly influence the motion [26, 74, 84]. There are interactions between the solid and fluid forces in a debris flow, which provide the flow with a unique destructive power [64, 95]. Debris flows can result from individual slope failures or multiple small failures that coalesce downstream [44, 113]. Debris flows are commonly categorized as [35]:



Figure 1.1: Three different zones describing a complete debris flow dynamics, an example from Daniao debris flow induced by the Typhoon Morakot, Eastern Taiwan: (a) initiation zone, (b) track, and (c) run out zone [114].

- (i) open slope debris flows that originate from slope failures, and
- (ii) channelized debris flows that develop along pre-existing stream paths.

Debris flows have adverse effect on human life, infrastructure, and the natural environment in mountain areas and in the valleys [74, 89, 93, 113]. The region where a debris flow is triggered is called the *initiation zone*. Then, the debris material moves along the *tracks*, mainly due to gravitational force until it gets decelerated, and then, deposited in the *run out zone*, (see, Fig. 1.1). A typical debris flow surge may have a steep head with densest slurry with the highest concentration of boulders followed by a progressively more dilute and shallower tail [44, 63]. However, how, whether, and which part of the debris body behaves more like solid, or more like fluid depends on several geometrical, dynamical, boundary and initial conditions of the flow, and also the characteristics and the amount of the different constituents of the material involved in the entire flow process [84, 91, 92].

## 1.4 Different Mass Flow Events and Associated Hazards in Nepal

Being a landlocked country and being far from the seashores, Nepal is not directly affected by the tsunamis in ocean. Similarly, there is no report of significantly strong

volcanic eruptions in the recent history. However, Nepal has wide range of diversity in topography from the world's highest mountains to low and flat Terrain plains. So, time and again, every year there are several reports of frequent and devastating landslides, debris flows, and flash floods mainly during the Monsoon, or the late Monsoon season, when the soil is saturated by water.

According to Pudasaini and Hutter (2007) [89], one of the biggest and huge landslides due to the heavy monsoon rains in 15<sup>th</sup> July 2002 made 228 families homeless along with 44 fatalities in a hilly district of Khotang in Nepal, which is situated 200 km south east of the capital city Kathmandu. Not later than a week of this incident, another unpleasant incident of floods and landslide in Makwanpur district claimed 26 human lives.

In Nepal, glaciated high mountain regions are highly susceptible to the climate changes<sup>3</sup> and pose great threats to the downstream population and the settlements [5, 29, 73, 118]. Deglaciation is supposed to be the main cause of the formation and the increase of glacier lakes [99]. The melt-water contribution of glaciers are of particular importance for the hydropower plants in Nepal; at the same time, GLOF (Glacial Lake Outburst Flood), rainfall, landslides and highly particle-laden streams seem to be the main threats for these plants [98]. In a GLOF, there is a sudden discharge of substantially higher amount of water than the normal flow from a lake formed at the snout of a glacier, see, Fig. 1.4 because of a breach of the moraine dam [3]. In many GLOF events of the glaciated regions, the main trigger mechanism is the wave generated due to snow or rock avalanches into glacial lakes. Other causes may be melting of ice core of the moraine damming of a lake, overtopping of a moraine due to heavy rain, or snow and earthquakes [5].

The GLOF that occurred at the Dig Tsho lake in the Khumbu Himal of Nepal in August 4, 1985 due to ice avalanche from Langmoche hanging glacier was one of the most destructive events of its kind. When the ice-rock avalanche cascaded into the lake, it resulted in a huge surge wave which overtopped the moraine and  $6 - 10 \times 10^5 \text{ m}^3$  of water downstream, which is large mass flow event [41]. The GLOF had hit Namche Hydropower Plant, 11 km downstream and 14 bridges causing a loss of \$500 million<sup>4</sup> along with many casualties [99]. Now, the reformed lake seems to be threatless, see, Fig. 1.2.

Lake Palcacocha is situated at an elevation of 4567 m in the Quillcay catchment of the

---

<sup>3</sup>IPCC, Climate change 2007 synthesis report. In: Pachauri, R.K., Reisinger, A. (Eds.), Contribution of Working Groups I, II and III to the Fourth Assessment Report of the Intergovernmental Panel on Climate Change. IPCC, Geneva, 104 pp.

<sup>4</sup>G. Rees: Glaciar retreat and glacier lake outburst floods in the Himalaya: WATCH-HighNoon Open Science Seminar Future of water resources in India under a changing climate 13-14 May 2009.



Figure 1.2: Dig Tsho Lake in April 2009 in Nepal; the GLOF event of 1985 destroyed the moraine dam [41].

Cordillera Blanca in Peru. The lake has drawn attention since the city of Humraz was devastated due to a GLOF that surged down the lake on December 13, 1941 claiming the lives of more than 5000 people [115]. As the water level is higher than the safe level, still there is a threat of potential landslide or ice avalanche that could lead to the moraine

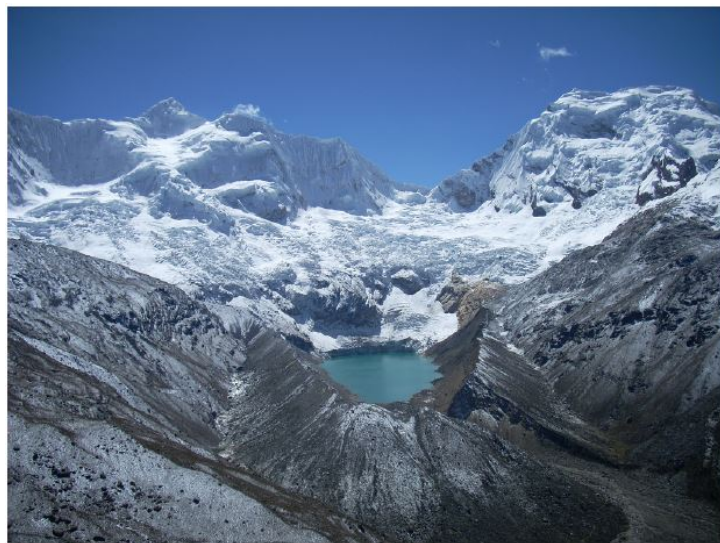


Figure 1.3: Palcacocha Glacial Lake in Peru (photo by Colette Simonds) [103].

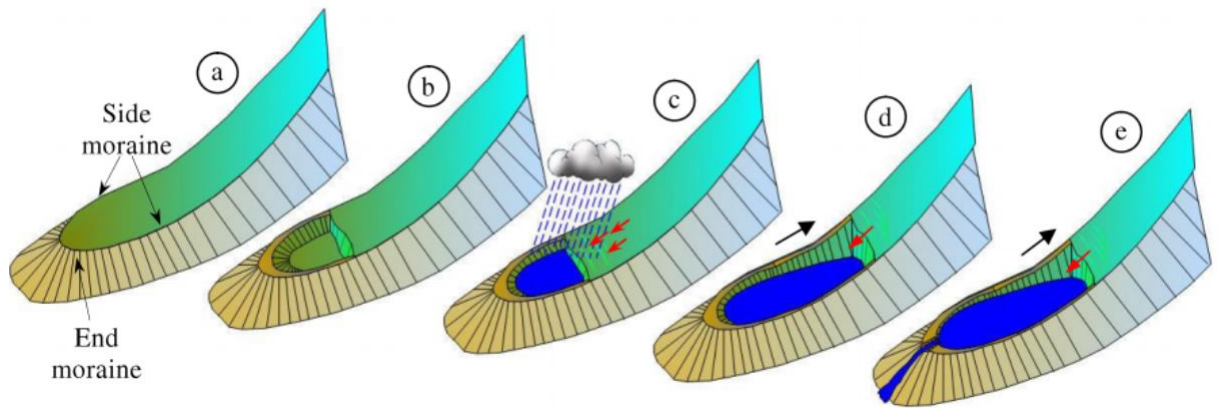


Figure 1.4: Formation of moraine-dammed lake in glaciated high mountain and a possible scenario of GLOF due to wave overtopping and erosion [3].

failure to release abruptly a huge mass of water to create a GLOF [103], see, Fig. 1.3.

In Nepal, one of the lakes with great potential flood volume is Tsho Rolpa Lake of Dolkha district, as an example of moraine-dammed lake, see, Fig. 1.5a. Similarly, Gokyo Tsho (Fig. 1.5b) is an example of glacier-dammed lake [29]. For the safety of the people and the infrastructure in the downstream of the glacial lakes, better, advanced and timely understanding of the GLOF hazards and associated phenomena is needed.

As the scenic and touristic Pokhara Valley, Nepal, itself is believed to be formed due to

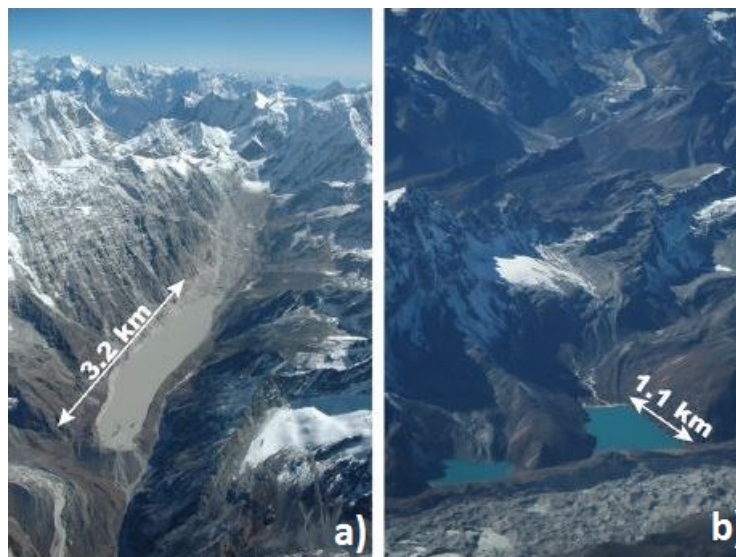


Figure 1.5: Glacial lakes and their potential hazards in Nepal: a) Tsho Rolpa, a moraine-dammed lake, and b) Gokyo Tsho, a glacier dammed lake in November 2007 [29].



Figure 1.6: The view of Seti River in Kharapani, Kaski District, Western Nepal, after the destruction by the debris and mud flow of 5 May, 2012. (Left) During the flood: There were several houses at the left bank of the flow direction of the river. (Right) After the flood: The houses were swept away. The almost fine debris deposit fan is seen on the right. The photo was taken by an unknown picnic boy, provided to us by Ranjan K. Dahal.

a fanglomeratic aggradation, transported alternately by massive mud flows, debris flows and torrential discharges, catastrophic and unpredictable geomorphological hazards that might occur at any time are always posing a significant threat to the local population and infrastructure [26].

In May 5, 2012, the rock-ice avalanche or landslide and subsequent debris flow in the Seti River of Pokhara valley swept away several houses along the river bank of Kharapani (see, Fig. 1.6). From comparing the pre- and post-disaster images, it is inferred that the debris-flood in the Seti River might have been triggered by the high-altitude massive rock slope failure [7]. The rock-ice avalanche that initiated due to the collapse of the rock-ice wall at the southwest flank of the Annapurna IV caused the massive debris-flood as it suddenly plunged into the Seti River [7]. The massive landslide rapidly mixed with Seti River triggered the tremendous floods that devastated the downstream Pokhara valley. As it cascaded downstream, the landslide gained high momentum, also entrained substantial amount of loose material from the path and the banks of the river on its way. Following the collapse of the rock wall at high elevation steep flank of Annapurna IV, the huge impact at the ground, rapid shearing, and internal and basal friction in the falling mass might have added much of the melt water from the ice that might have resulted

in largely fluidized flow [90] of the debris material in the Seti River, forming a rapidly moving debris flow consisting of a mixture of highly viscous mud, sand, gravel, rocks, silt and clay saturated with water [84]. Observers described the flow of the mud-choked river as thick and like a swamp<sup>5</sup>. 71 people were either killed or forced missing, which include the trekkers and people enjoying on picnic and hot water spring. The debris flood traveled about 20 km (elevation difference: about 1800 m) in about 35 minutes, which is a very common, but, relatively a fast speed for a debris flow (mean slope  $5^\circ$  and average speed of  $10 \text{ ms}^{-1}$ ) [7].

The climate changes might have increased the frequency and magnitudes of such landslides, avalanches and mud/debris flows, and GLOF. The increase of such events has drawn the attention of national and international organizations to carry out research for preventive and mitigative measures. The increasing need for the fundamental, scientific and technological research on the dynamics of different geophysical mass flows in Asia, and particularly, in Nepal, has been, in some extent, realized and addressed in the recent *11th International Symposium on Mitigation of Geo-disaster in Asia (MGDA-11) held in Kathmandu and Pokhara, Nepal, during 22 – 28 October, 2013*. Our present work is a step forward in establishing and enhancing the scientific foundation to the proper and advanced simulations of such disastrous debris flow events and their associated dynamics. This helps in designing appropriate defense structures, mitigation measures, and land use planning.

## 1.5 Prevention and Mitigation Measures

Every year all around the globe, debris flows cause an immense amount of damage to the people and their properties [44, 45, 70, 74, 89, 94, 113]. The growing population and the ongoing development activities have put inevitable pressure on planners and developers to build infrastructures even in areas that have elevated risk of different geophysical mass flows [38, 39, 89, 104]. From technical and application point of view, the main purpose of research activities on the dynamics of geophysical mass flows is to protect the people and infrastructures that are exposed to increased risk of debris flows and other related geophysical mass flows.

Industrialized and developed mountainous countries, including the United States, Canada, Japan, France, Austria, Italy, Norway, Russia, and Switzerland have practised several protection measures to safeguard the densely populated areas, traffics or, power supply lines

---

<sup>5</sup><http://earthobservatory.nasa.gov/NaturalHazards/view.php?id=78117>.



Figure 1.7: (a) Engineering, and (b) bio-engineering techniques to protect the part of the Prithvi Highway at Krishnabhir, Central Nepal. Before the mitigation measures had been applied on 2003, the recurrent landslide and debris flows used to block the highway for weeks in every Monsoon (rainy) season. (Photo: Field excursion during the symposium, MGDA-11).

[89]. The protection measures that are related to engineering or bioengineering ones may differ according to the slope, orientation, topography, geology, surface and sub-surface hydrology of the slope, vegetation and the nature of the area or the structure that are to be protected [13, 16, 67, 89, 107]. After the massive failure of landslide and resulting debris flow in 2003, the major steps taken as an effective mitigation measures against the recurrent landslide of Krishnabhir along the Prithvi Highway, central Nepal (see, Fig. 1.7) included the removal of loose debris from the slope surfaces [16]. The bio-engineering technique has been used, especially to strengthen the slope surface against further erosion [16]. The slope stability has been strengthened by using plant materials and by developing appropriate vegetation. Such a technique takes quite a while to be fully established for the method to function [16]. Soil Bioengineering is considered to be effective and sustainable, though it is time consuming. It helps to tackle with the soil erosion and also to control the shallow landslide by improving the soil water condition to stabilize the slope<sup>6</sup>.

Another common method used in Nepal as a control measure applied to slope, torrent and gully control is the classical check dam. Check dams consist of series of sills which reduce the destructive power, or momentum, thus, the velocity of the flood or debris flow

---

<sup>6</sup>Recommendations for future installation and implementation of countermeasures against rapid mass movements: WSL Swiss Federal Institute for Snow and Avalanche Research, 2008.

by changing the hydraulic condition from supercritical (high) to subcritical (low) flow [78, 107]. Check dams effectively reduce the slope so that the solid mass tends to sediment and hence, the destructive power reduces the erosion activities [108]. After falling down from a height, debris flows lose dynamic forces while flowing in a relatively flat surface [22, 23, 34, 76, 107]. To protect the highways and bridges from the landslides and recurrence of debris flows, some engineering and bioengineering techniques including debris flow catch dams, wire barriers and defense structures, appropriate vegetation in the area of significant to high water table are becoming popular in Nepal (Fig. 1.8).

A monsoon cloudburst and the resulting downpour of July 31, 2003 caused several landslides in the catchment of Ruwa Khola of Tanahu District of west Nepal and that carried down massive flood and debris flow with big boulders (up to 2 m in diameter) causing the damages to the Prithvi Highway (Fig. 1.8) and 69 MW Marshyandi Hydroelectric power station [16]. In 2005, two main concrete debris flow catch dams were constructed upstream from the bridge of the Prithvi Highway as an effective measure to control debris flows and debris floods [16].



Figure 1.8: Torrential control and mitigation of a mountain slope and a torrent by check-dams against a torrential flood and debris flows in Ruwa Khola at Tanahu District, west Nepal. (Photo: Field excursion during the symposium, MGDA-11).

## 1.6 Mechanics of Debris Flows and Their Modeling

To assign a fixed rheology to interpret or predict any debris-flow motion may not be accurate. The evolving behavior of debris flows is very complex, and therefore cannot be represented by only one rheological equation [38, 39].

On the Earth in natural condition, granular materials are present as a mixture of loose solid, liquid and/or gas. If the interstitial fluid does not play a significant role in the transportation of mass and momentum, such materials can be considered as dispersed single-phase flows [89]. Not only the rockfalls, landslides and snow avalanches, but also pipe and channel flows of grains and pills in the biotechnological and pharmaceutical industries, agricultural and process engineering [88, 89] fall in this category. In view of simple modeling, in many cases, debris flows can be described with sufficient accuracy by single-phase flow models [47, 83, 113]. However, in general, in a debris flow, the interstitial fluid is comparable to that of the solids [74, 89]. As the solid phase and the fluid phase show different flow behaviour, two phase modeling of debris flows is required in many realistic situations [74, 84]. Since it contains (significant amount of) both the solid and the fluid phases, a real two-phase debris flow is an advection-diffusion process. To model such complicated advective-diffusive processes of two-phase debris flows, a set of mass and momentum conservation equations are needed, separately, for both phases, in all possible flow directions [74, 84]. However, our simulation and analysis is based on the most generalized and comprehensive mechanical model proposed by Pudasaini (2012) [84]. This model is enriched with several dominant physical aspects of the real two-phase debris flow with strong interaction between the solid and the fluid phases, including, generalized drag, virtual mass, buoyancy, and solid-volume fraction-gradient-enhanced non-Newtonian viscous stress.

We also mention that, although the constituent materials and the flow dynamics may vary in different geophysical mass flows, similar modeling and simulation techniques can be used to describe the flow of granular materials and snow avalanches [30, 74, 75, 89, 113].

# Chapter 2

## Modeling the Dynamics of Real Two-Phase Debris Flows

Geophysical mass flows, such as landslides, avalanches, debris flows, tsunamis, and also the industrial flows of granular materials are usually modeled by a set of non-linear partial differential equations as derived from the basic continuum mechanical mass and momentum balance equations. While developing the model equations, these balance equations are closed by appropriate rheological equations that describe the relationship between the applied forces and deformations for any given material. Similarly, the balance equations are also complemented by suitable initial and boundary conditions. In this chapter, we present different rheological models that are often in use in modeling the mass flows, including rheological models for bulk deformations and the deformation of the solid and the fluid phases in a real two-phase debris motion. We present three dimensional, real two phase debris flow model of Pudasaini (2012) [84] and pay special attention on the depth-averaged model equations to be used for numerical integration. We discuss on the major advancements in modeling geophysical mass flows, in general, and in particular, the (geometrically) three-dimensional and two-phase debris flow simulations that will be presented in Chapter 4. We discuss the special features of the model equations along with the reduction of the real two-phase debris flow model to other relatively simple debris flow and avalanche models.

### 2.1 Rheology Related to Two-Phase Debris Flows

<sup>1</sup>Before presenting the full three-dimensional and two-phase model for the motion of the mixture of solid particles and the fluid, we present a short description on the basic flow

---

<sup>1</sup>This section closely follows the Lecture Notes: *Dynamics of Geophysical Mass Movements, Vol. I, and Vol. II, 2007*, by Shiva P. Pudasaini, Department of Geodynamics and Geophysics, University of Bonn, Germany [82].

rheologies associated with the deformation of the solid and the fluid phases, respectively. Material response to a stress is known as rheology, and a relationship between stress and strain is called a constitutive model [82]. In a continuum mechanics, a material is considered to be a continuum rather than a set of discrete constituents [37]. A moving continuum material may be described by the balance laws [32]:

$$\frac{\partial \rho}{\partial t} + \rho \nabla \cdot \mathbf{u} = 0, \quad (\text{mass balance equation}), \quad (2.1)$$

$$\rho \frac{d\mathbf{u}}{dt} - \nabla \cdot \boldsymbol{\sigma} - \rho \mathbf{b} = 0, \quad (\text{momentum balance equation}), \quad (2.2)$$

where,  $\rho$  is bulk density,  $\mathbf{u}$  is velocity,  $\boldsymbol{\sigma}$  is Cauchy stress tensor,  $\mathbf{b}$  is body force density and  $d/dt$  is the material derivative. For geophysical mass flows, the body force density is usually given by the acceleration due to gravity  $\mathbf{g}$ . The balance equations (2.1)-(2.2), along with appropriate constitutive equations for  $\boldsymbol{\sigma}$  and suitable initial and boundary conditions, result in a system of partial differential equations modeling the geophysical mass flows. However, note that, depending on the effectively single-phase or a two-phase mass flows, we would need two separate mass and momentum balance equations for the solid and the fluid phases, respectively [74, 84]. If the moving mass is considered to be incompressible, i.e.,  $\rho = \text{constant}$ , then the mass balance equation (2.1) becomes  $\nabla \cdot \mathbf{u} = 0$ , which is called the continuity equation.

**A. Elasticity:** Under the same applied stress, different materials may behave differently. Ideally, materials can be modeled as a simple elastic, plastic, or viscous material. An *elastic* material shows a conservative property in which a part of the mechanical energy is used to produce deformation which is stored within the material and the material regains its original configuration when the stress is removed [82, 89]. Under normal conditions and under relatively low loads, solid materials generally behave as an elastic material.

**B. Plasticity:** In general, a solid body behaves as an elastic material (i.e., the material regains its original configuration when the applied stress is released) under some threshold value of stress, called the *yield stress*. However, beyond that threshold value, the material shows non-recoverable deformation even if the stress is released. Such deformation is called *plastic* deformation and the material is said to be in a plastic state. During a plastic deformation, energy dissipation and stress are independent of the rate of deformation [32, 82, 102]. Hence, plasticity is a property of a material to undergo non-recoverable change of configuration in response to an applied force. Granular materials, mild steel and clay are some examples of plastic materials [32].

**C. Viscosity:** *Viscosity* is the tendency of a liquid to resist flow due to its internal friction. During a viscous deformation, mechanical energy is dissipated into heat [102].

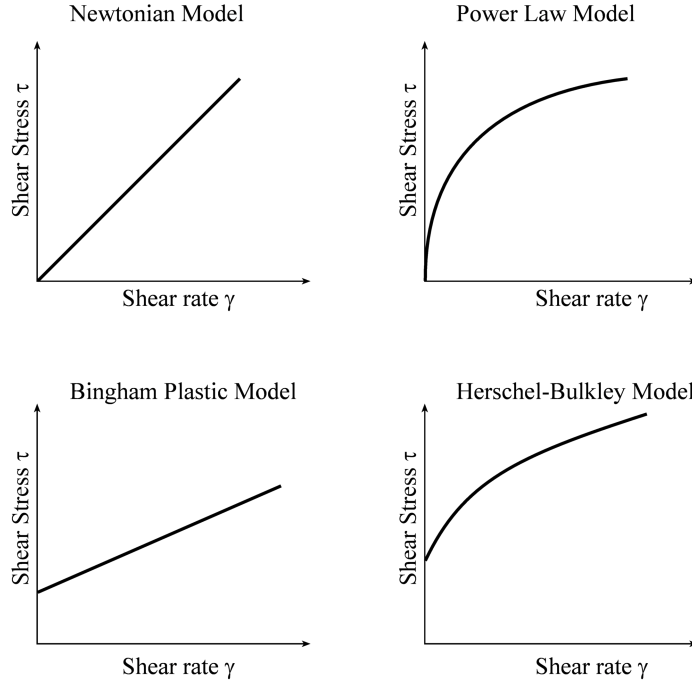


Figure 2.1: Different rheological models to show the relationship between the shear stress  $\tau$  and the shear-rate  $\gamma$ . The figure has been reproduced from the Lecture Notes by Pudasaini (2007) [82].

A viscous deformation is non-recoverable. For viscous material, the stress is proportional to the strain rate [82]. A viscous material is described by [4, 83, 111]

$$\tau = K_D(\partial u/\partial y)^n, \quad (2.3)$$

where,  $\tau$  is the applied stress,  $\partial u/\partial y$  is the strain-rate,  $K_D$  is the consistency index,  $n$  is an exponent. The flow that satisfies (2.3) with linear exponent ( $n = 1$ ) is called the Newton's law of viscosity, for which  $K_D = \eta$  is the fluid viscosity. Some examples of Newtonian fluids include water, air and the organic fluid with low molecular weights like ethanol, glycerine and benzene [62, 83, 102]. The flow which is not Newtonian is called non-Newtonian, examples include, non-linear, or power laws, see, Fig.2.1, with  $n > 1$ , or  $n < 1$ . Fluids like blood, paints and polymer of high molecular weight show non-Newtonian behaviour [62, 83, 102]. So, the viscous materials show time dependent behaviour. Less viscous materials deform relatively faster and easily than more viscous materials [32]. So, the viscosity corresponds to the fluid behaviour, whereas the elasticity is related to the solid deformation.

**D. Viscoelasticity:** In reality, materials can be much more complex than the ideal elastic, plastic, or viscous materials. So, to describe the behaviour of a real material in

a better way, a combination of elastic, plastic, and viscous materials may be needed [82]. However, it also depends on how we combine and arrange different material components in order to produce a more complex and composite material [82]. One of such many combinations is viscoelasticity. *Viscoelasticity* is a time-dependent property in which a material under the given stress produces both an elastic and a viscous response. A viscoelastic material shows viscous flow behaviour under an applied stress, but a portion of mechanical energy is conserved and is recovered after the stress is relaxed. Viscoelastic materials possess the abilities like creeping, recovering, undergoing stress relaxation and absorbing energy as in cohesive dry snow avalanche, wood, metal, polymer, etc. [32, 82].

When the elastic (solid,  $E$ , which is related to the Young's modulus, or the modulus of elasticity, i.e., the Hook's law) and viscous (fluid,  $\eta$ , which corresponds to the Newtonian viscosity) elements are arranged in series, we obtain a composite *Maxwell* viscoelastic material. For a Maxwell viscoelasticity, the total strain-rate is given by [32, 82]:

$$\frac{d\varepsilon}{dt} = \frac{1}{E} \frac{d\sigma}{dt} + \frac{\sigma}{\eta}, \quad (2.4)$$

where  $\sigma$  is the stress,  $E$  is the elastic constant (solid property),  $\eta$  is the dynamic viscosity (fluid property) and  $\varepsilon$  is the strain [32].

**E. Bingham Plastic:** *Viscoplasticity* is another hybrid material property in which a material acts like a solid until a critical stress value, called the *yield stress*, but flows like a viscous fluid beyond this yield stress,  $\tau_y$  [18, 19, 32]. The velocity gradient for a viscoplastic material is described by [62]

$$\frac{\partial u}{\partial y} = \begin{cases} 0, & \text{if } \tau < \tau_y, \\ \frac{\tau - \tau_y}{\eta}, & \text{if } \tau \geq \tau_y, \end{cases} \quad (2.5)$$

where,  $x$  is the coordinate in the flow (down-slope direction),  $u$  is the (fluid) velocity in the flow, or  $x$ -direction, and  $y$  is the direction perpendicular to the channel (slope). So, (2.5) means that the material is rigid for shear stress  $\tau$  less than a threshold value  $\tau_y$ , but it deforms as if it was a Newtonian viscous material once the yield strength is reached ( $\tau \geq \tau_y$ ), (see, Fig. 2.1). The material described by (2.5) is called *Bingham plastic* material, which can also be written as

$$\tau = \tau_y + \eta \frac{\partial u}{\partial y}. \quad (2.6)$$

For highly concentrated sediment water mixture, the Bingham model can be used with  $\tau_y = \tau_{yc} + N \tan \phi$ , where  $\tau_{yc}$  denotes cohesive yield stress,  $N$  is the normal stress,  $\phi$  is the internal friction angle for the solid particles [48, 83]. Viscoplastic materials are used

in modeling mud and debris flows [83].

**F. Herschel-Bulkley:** In many situations, the flow can be better modeled by three parameter *Herschel-Bulkley* rheology, which is the extension of the Bingham plasticity, and extends the linear viscous to include the non-linear viscous deformation. The stress-strain non-linear relationship is given by [83, 101, 102] (see, Fig. 2.1):

$$\tau = \tau_y + K_{HB} \left( \frac{\partial u}{\partial y} \right)^n, \quad (2.7)$$

where  $K_{HB}$  and  $n$ , are, respectively, the Herschel-Bulkley consistency index, and non-linearity parameters that are to be determined by experiments [14]. Depending on the value of the exponent  $n$ , i.e.,  $n > 1$ , or  $n < 1$ , the flow can be shear-thickening, or dilatant fluid (e.g., some types of honey, 40% raw corn starch solution), or shear-thinning or pseudoplastic (e.g., apple sauce, banana puree) above some yield point [8, 32, 62, 84]. The Herschel-Bulkley model can be used to describe composite materials, such as, concrete, mud, and toothpaste [83]. The Herschel-Bulkley model reduces to the power-law, when the yield-stress is zero, to the Bingham plastic model when the flow behavior exponent is unity, and to the Newton's law for viscous fluids when both the yield-stress is zero and the flow behavior exponent is unity, i.e.,  $K_{HB} = \eta$  [8, 102].

**G. Pressure- and Rate-Dependent Coulomb-Viscoplasticity:** Recently, Domnik and Pudasaini (2012) [18], and Domnik et al. (2013) [19] have proposed more advanced viscoplastic models to better describe the full dynamics of the rapid flows of granular materials down the channels impinging on rigid walls or, transiting into the deposition. Their models are called the pressure and rate-dependent Coulomb-viscoplastic rheological models [18, 19]. In contrast to the Herschel-Bulkley, or Bingham plasticity, the models presented by Domnik and Pudasaini (2012) [18] and Domnik et al. (2013) [19] do not include any fit parameters, and these models are thus fully described by the phenomenological parameters of the materials. By presenting several flow simulations, from the material collapse and silo outlet to the final depositions, they have demonstrated the applicability of their new rheological models with very high computational performances while coupling between the full-dimensional and reduced dimensional models in a novel multi-scaling modeling and simulation strategy [18, 19]. Their novel model describes several important and unique behaviour observed in geophysical mass flows, such as avalanches and debris flows, including the solid-fluid and fluid-solid transitions, during the mass collapse, or release, flow obstacle interactions and deposition processes.

For incompressible dry granular flows, Domnik and Pudasaini (2012) [18] and Domnik et

al. (2013) [19] began with the fluid mechanical mass and momentum balance equations

$$\nabla \cdot \mathbf{u} = 0, \quad (2.8)$$

$$\frac{d\mathbf{u}}{dt} = \nabla \cdot \boldsymbol{\sigma} + \mathbf{g}, \quad (2.9)$$

where  $\boldsymbol{\sigma}$  is the Cauchy stress tensor normalized by the bulk density  $\rho$ , and the gravitational components for channel flows are given by  $\mathbf{g}(\zeta) = (g \sin \zeta, -g \cos \zeta)^T$ , with gravity constant  $g$ ,  $\zeta$  is the channel inclination angle, and  $d/dt$  is the material derivative. The motion and the settlement are described by constitutive laws [1, 6, 27, 49]

$$\boldsymbol{\sigma} = -p\mathbf{I} + 2\nu\mathbf{D} + 2\tau_y \frac{\mathbf{D}}{\|\mathbf{D}\|}, \quad (2.10)$$

which is the normalized stress tensor for a viscoplastic material (fluid), where  $p$  is the normalized pressure. The symmetric part of the velocity gradient  $\mathbf{D} = \frac{1}{2}[(\nabla\mathbf{u}) + (\nabla\mathbf{u})^T]$  is the strain-rate tensor,  $\nu$  is the kinematic viscosity, and  $\tau_y$  is the yield stress. The norm of the strain-rate tensor is defined by  $\|\mathbf{D}\| = \sqrt{2\text{tr}(\mathbf{D}^2)}$ . In terms of an effective viscosity:

$$\nu_{eff} = \nu + \frac{\tau_y}{\|\mathbf{D}\|}, \quad (2.11)$$

equation (2.10) can be written as  $\boldsymbol{\sigma} = -p\mathbf{I} + 2\nu_{eff}\mathbf{D}$ . However,  $\nu_{eff} \rightarrow \infty$  as  $\|\mathbf{D}\| \rightarrow 0$ . To overcome this problem in computation, Domnik et al. (2013) [19] introduced the exponential factor  $m_y$  as

$$\nu_{eff} = \nu + \frac{\tau_y}{\|\mathbf{D}\|} (1 - e^{-m_y\|\mathbf{D}\|}). \quad (2.12)$$

The material behaves as a Newtonian fluid for  $\tau_y = 0$ .

As explained above, a Bingham material is described by a constant yield stress. However, in granular flows, this may not be enough to describe a complex dynamical pressure-dependent yield property of the material. To capture such typical flow behaviour of a geophysical mass flows, Domnik et al. (2013) [19] proposed a pressure dependent yield stress

$$\tau_y = \tau_p p, \quad (2.13)$$

for describing the frictional nature of the granular material in a better way. This forms a Drucker-Prager yield criterion [81] with no cohesion

$$\sqrt{II_{\sigma D}} \geq \tau_p p, \quad (2.14)$$

where,  $II_{\sigma D}$  is the second invariant of the deviatoric stress tensor [81]. The relation (2.14) simply tells us that material undergoes plastic yielding when deviatoric stress is greater

than the yield stress. In two dimensional space, the Drucker-Prager yield surface is equivalent to Mohr-Coulomb yield surface with  $\tau_p = \sin \phi$  where,  $\phi$  is the internal friction angle, usually  $\phi$  is on the order of  $30^\circ$ . With several complex flow simulations, from silo outlet to the flow obstacle interactions, and depositions with solid-fluid and fluid-solid transitions, Domnik et al. (2013) [19] demonstrated that the pressure-dependent yield stress is a very good rheological model. They have shown that, the classical Bingham plastic model cannot appropriately describe the depositional behaviour of the granular material which can very well be described and simulated by the rate- and pressure-dependent Coulomb-viscoplastic model. Furthermore, cohesion can easily be included in the model (2.10) by  $\tau_y = \tau_c + \tau_p p$ , where,  $\tau_c$  is tensile stress. However, for dry granular materials, usually,  $\tau_c = 0$  [19, 89].

**H. Quadratic Model:** O'Brien and Julien (1985) [69] proposed a quadratic rheological model to apply in sediment transport and hyper-concentrated flows:

$$\tau = \tau_y + \eta \left( \frac{\partial u}{\partial y} \right) + K_D \left( \frac{\partial u}{\partial y} \right)^2, \quad (2.15)$$

where, the first term includes the cohesive and Mohr-Coulomb yield strength (so, the solid property), the second term takes into account the viscous (fluid) effects, and the last term corresponds to the turbulent (inertial shear stress) and dispersive stresses [69, 82, 89].

**I. Bagnold Grain Inertia:** Owing to the complexity of the system, it is less probable to describe debris flows by any constitutive equations. However, in many cases, debris flow events can well be described by Bagnold-type dilatant fluid [4, 111] with  $\tau = K_D (\partial u / \partial y)^n$ , where  $K_D$  is a consistency index [83]. If the shear and normal stresses in the mixture (suspension) vary quadratically ( $n = 2$ ) with the shear-rate, the motion is said to satisfy Bagnold's grain-inertia flow. If this relation is linear ( $n = 1$ ), then, the flow is said to satisfy Bagnold's macroviscous flow [83]. These flow laws were derived by Bagnold in 1954 after performing some novel experiments in an annular coaxial cylinder rheometer [89], where he evaluated the effects of grain interaction in the suspension. These types of relationships have also been confirmed by many subsequent shear-cell experiments for both wet and dry mixtures [11] and computer simulations [66, 100]. However, note that, Hunt et al. (2002) [36] suggested that there can be some inconsistencies and shortcomings in Bagnold's experiments and data analysis [83]. Bagnold's rheology can be rewritten and put in the form of a Newtonian fluid  $\tau = \eta_a (\partial u / \partial y)$  in which the corrected (apparent) viscosity  $\eta_a = K_D (\partial u / \partial y)^{n-1}$  turns to be a function of the shear-rate. For  $n = 1$ , this corresponds to Newtonian viscous fluid with  $K_D = \eta$  [83]. However, for  $n = 2 > 1$  (shear thickening) the apparent viscosity increases with increasing shear-rate and one obtains

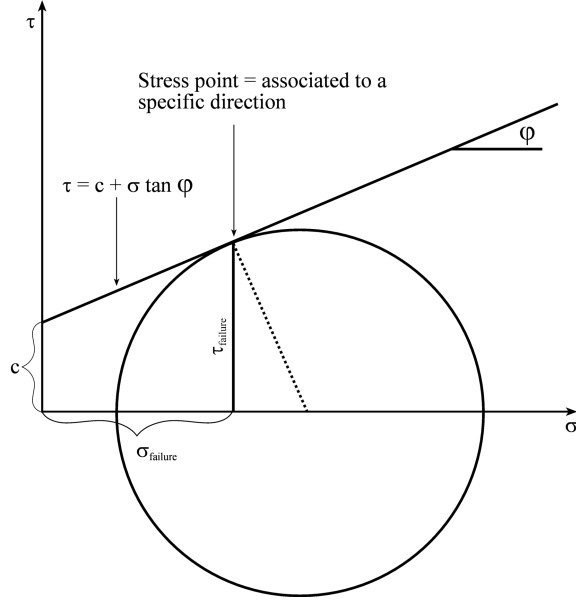


Figure 2.2: Coulomb envelop ( $\tau = c + \sigma \tan \phi$ ), Mohr-circle, and the Mohr-Coulomb failure as the Mohr circle hits the Coulomb strength envelope in the  $\sigma - \tau$  plane. This figure has been reproduced from the lecture notes by Pudasaini (2007) [82].

the Bagnold's dilatant fluid. Similarly, for  $n < 1$  the apparent viscosity decreases with increasing shear-rate and one obtains the shear thinning fluid [28, 83].

**J. Mohr-Coulomb Plasticity:** Savage and Hutter (1989) [96] proposed Mohr-Coulomb plastic yield criterion for rapid granular flows. This model has been successively and largely used for the deformation of the effectively single-phase materials, like avalanches and granular flows. This model assumes that the material fails plastically when the Mohr-circle of two-dimensional state of stress (in  $\sigma - \tau$  plane) hits the Coulomb failure envelope given by

$$\tau = c + N \tan \phi, \quad (2.16)$$

where  $\tau$ ,  $c$ ,  $N$  and  $\phi$ , respectively, are the shear strength, cohesion, normal load, and the internal friction angle of the material. The failure situations for the active and passive states are explained in detail, e.g., in Pudasaini and Hutter (2007) [89] and Savage and Hutter (1989) [96]. However, a simple Mohr-Coulomb failure condition is presented in Fig. 2.2. Similarly, how to determine the internal ( $\phi$ ) and basal ( $\delta$ ) friction angles for given granular materials and sliding surfaces have been explained in detail and collectively in Pudasaini and Hutter (2007) [89] with values for different granular materials. The friction angles are low when grains and the basal surfaces, on which they flow, are smooth, and high when the grains and the basal surface are coarse. In general,  $\phi$  is found in the range

$15^\circ - 45^\circ$ , higher values corresponds to gravel, whereas lower values may correspond to very smooth particles, such as glass beads. More complex granular flow models have also been proposed by Pouliquen and Forterre (2002) [80], Jop et al. (2006) [49], Pudasaini (2011) [83], Domnik et al. (2013) [19].

**K. Mohr-Coulomb Plasticity and Newtonian Viscous Law:** The Mohr-Coulomb failure criterion have also been extensively used to describe the debris flow motions. Iverson (1997) [44], Iverson and Denlinger (2001) [45], and later, Pitman and Le (2005) [74], and Pudasaini et al. (2005) [94] utilized Mohr-Coulomb plasticity for the solid and Newtonian viscous law for the fluid components of the debris mixture.

**L. Mohr-Coulomb Plasticity and Non-Newtonian Viscous Law:** The fluid viscosity and the viscous stress may substantially depend on the amount of the solid particles in the mixture. To take this aspect into account, Pudasaini (2012) [84] proposed a non-Newtonian fluid rheology, in which the fluid viscous stress is enhanced by the solid-volume-fraction-gradient, and the solid phase is modeled by applying the Mohr-Coulomb plastic failure criterion. This will be discussed in detail in §2.4.

## 2.2 Major Advancements in Modeling Geophysical Mass Flows

In the past, various rheological models were presented for geophysical mass flows, and they were effectively single phase models, e.g., viscoplastic continuum or Bingham model which treats the debris material as a single phase material that remains rigid up to certain threshold value of stress, called a plastic yield stress [18, 19, 44, 47, 49, 63, 112]. As mentioned in §2.1, in single-phase debris flow models, the mixture of fluid and solid particles is considered as a continuum fluid [2, 9, 17, 40, 70, 89, 110, 113]. The apparent single-phase debris fluid is characterized by the constitutive relationship between the operating shear stress and the strain-rate. Examples include the Newtonian fluids and non-Newtonian fluids, e.g., Bingham, Herschel-Bulkley, and dilatant fluid. The Newtonian fluid is represented by the flow of pure water without any solid particles [18, 19, 83]. There have been significant fundamental research activities in the past few decades in the field of debris flow and other similar mass flows. They are as follows:

- single-phase dry granular avalanches (Savage and Hutter, 1989 [96]; Hungr, 1995 [35]; Hutter et al., 1996 [40]; Gray et al., 1999 [30]; Pudasaini and Hutter, 2003 [88]; and Zahibo et al., 2010 [119]),

- single-phase debris flows (Bagnold, 1954 [4]; Chen, 1988 [12]; O' Brien et al., 1993 [70]; Takahashi, 2007 [113]; and Pudasaini, 2011 [83]),
- mixture flows (Iverson, 1997 [44]; Iverson and Denlinger, 2001 [45]; and Pudasaini et al., 2005 [94]),
- two-fluid debris flow (Pitman and Le 2005 [74]), and
- two layered model (Fernandez-Nieto et al., 2008 [24]).

Existing models have significant limitations and many assumptions are required to reproduce the field or the laboratory data of these extremely complex fluid-particle interaction flows [10]. Modeling of a debris flow is much more challenging in comparison to the water flow due to its multi-phase character as the debris flow not only includes a viscous fluid but also a wide range of interacting solid particles of various sizes and shapes, e.g., from clay to silt to big boulders, some times also including timbers, etc. [62, 84]. In fact, natural debris flows are often unsteady, and the flow regime changes in space and time. So, the flow in the leading head may behave quite differently than the other parts, typically, the tail [45, 63, 64, 94].

With the major advance in the two-phase debris flow modeling and simulation, recently, Pudasaini (2012) proposed a comprehensive theory and simulation technique [84]. The model accounts for strong interactions between the solid and the fluid phases. Beside buoyancy, the model includes three other important and dominant physical aspects of flow: solid-volume-fraction-gradient enhanced non-Newtonian viscous stress, virtual mass, and generalized drag. This model constitutes the most generalized two-phase avalanches and debris flow model to date. As special cases of the new general debris flow model, one can recover other relatively simple models available in the literature for debris flows and avalanches [84]. The major physical aspects of the model are briefly discussed below.

Debris flows are multi-phase and gravity-driven flows consisting of a broad distribution of grain sizes mixed with fluid. The rheology and flow behaviour vary depending on the sediment composition and the percentage of solid and fluid phases [84, 91, 92]. The flow of two-phase mixture of grains and fluid is characterized by the relative motion as well as the interaction between fluid and solid phases. In the debris flows that occur in nature, one can see the substantial deviation of solid and fluid phase velocities from each other, thereby affecting the flow mechanics. There are several physical aspects which account for the underlying flow mechanics. One of them is the drag force induced by the relative velocity between the phases. The drag incorporates the basic coupling between the two

phases. A small change in the fluid viscosity can substantially change the debris flow dynamics. In fact, debris-flow dynamics rely on many different factors, including flow properties, topography, and initial and boundary conditions.

Fluid pressure and simple drag between the two phases have been included in some of the previous models (e.g., Iverson and Denlinger, 2001 [45]; Pitman and Le, 2005 [74]; Pudasaini et al., 2005 [94]), but they lack three very important physical aspects that can be observed in the real two-phase natural debris flows [84].

(i) As the two different phases have different phase velocities, they may have relative accelerations as well. This produces virtual mass effect, e.g., if the solid particles accelerate relative to the fluid, a part of the ambient fluid also accelerates, inducing a virtual mass force (the change in the kinetic energy of the fluid). The virtual mass force [20] has, for the first time, been incorporated in debris flow dynamics by Pudasaini (2012) [84].

(ii) Another important physical aspect that has been exclusively included in Pudasaini (2012) model is the solid-volume-fraction-gradient enhanced non-Newtonian viscous stress. In fact, the amount and gradient of the solid particles influences the flow substantially, which can either enhance or downplay viscous effects.

(iii) In Pudasaini (2012) model, sedimentation velocity and terminal velocity of an isolated solid particle falling in a fluid [74] and the Kozeny-Carman packing of spheres [72] have been combined to form a new generalized drag coefficient that can be used from linear to quadratic drag. This has been presented as a linear combination of the fluid-like drag and the solid-like drag force in the flow. As the material composition evolves in time and space in a real two-phase debris flow, this can lead to the formation of the solid-dominated (more solid material than fluid), or fluid-dominated (more fluid than solid fraction) local regions in the same debris body. In these realistic, but complex flow situations, the drag forces in the debris flows can only be properly modeled and described by applying a generalized drag force as proposed by Pudasaini (2012) [84].

## 2.3 Advancing the Two-Phase Flow Simulation

The two-phase debris flow model [84] has been presented in a well-structured set of non-linear hyperbolic-parabolic partial differential equations. To describe the two-phase dynamics of the flow, the model has been applied to one-dimensional debris flow down an

inclined channel. To date, single phase granular flows, or effectively single-phase debris flows have been simulated for three-dimensional topography [25, 30, 45, 65, 89, 94], and two-phase flows have been simulated only in the down-hill direction presenting the explicit evolution of the solid and the fluid components for both the subaerial and submarine debris flows [84, 85, 91, 92]. In chapter 4, we present some novel and basic (geometrically) three-dimensional simulation results for flows of a real two-phase debris material down an inclined surface. The simulation results are presented for the solid- and fluid-components and the total debris material for different parameter sets. Some of the simulation results have already been presented in Kattel et al. (2013) [52] and Kattel et al. (2014) [53]. More advanced simulations with more complex eigenvalues of the model system, the three-dimensional subaerial debris flows impacting a fluid reservoir and thus generating tsunami waves, and some exact solutions to reduced model can be found in Pokhrel et al. (2013,2014) [77, 78], Kafle et al. (2013, 2014) [50, 51] and Khattri et al. (2013, 2014) [54, 55], respectively. For the evolution of the total debris motion as a mixture of solid and fluid for a Glacial Lake Outburst Flood (GLOF), we refer, e.g., to Pitman et al. (2013) [75] in which the simulation is based on Pitman and Le 2005 [74] model.

## 2.4 Physical-Mathematical Model for Two-Phase Debris Flows

### 2.4.1 A Three-Dimensional, Real Two-Phase Debris Flow Model

In two phase debris flow model, the phases are characterised by different material properties [84]. The fluid phase is specified by its true density  $\rho_f$ , viscosity  $\eta_f$  and isotropic stress distribution; whereas for the solid phase, they are described by its true density  $\rho_s$ , internal friction angle  $\phi$ , the basal friction angle  $\delta$ , an anisotropic stress distribution, and the lateral earth pressure coefficients,  $K$  (as a function of the internal and basal friction angles) [30, 84, 96, 109]. These characterizations and the presence of relative motion between phases lead to two different mass and momentum balance equations for the solid and the fluid phases separately. Let  $\mathbf{u}_s = (u_s, v_s, w_s)$ ,  $\mathbf{u}_f = (u_f, v_f, w_f)$  and  $\alpha_s$ ,  $\alpha_f (= 1 - \alpha_s)$  denote the velocities, and volume fractions for the solid and the fluid constituents, denoted by the suffices  $s$  and  $f$ , respectively. In the general two-phase debris flow model proposed by Pudasaini (2012) [84], the phase-averaged balance equations for mass and momentum conservations are considered. Some realistic assumptions are made, including [20, 42, 43, 84]:

- The solid and fluid components are incompressible (the true densities are constants).

- No phase change occurs. However, recently mechanism of the phase-changes are developed and applied as an extension of the original two-phase model [84] by Pudasaini and Krautblatter (2012) [90]. The extended new enhanced mechanical model has been utilized to simulate the rock-ice avalanches in which the ice can be melted and thus substantial amount of the initially solid material transformed into fluid that enhances the flow mobility.

The full three-dimensional and two-phase debris flow model as developed by Pudasaini (2012) [84] is:

$$\frac{\partial \alpha_s}{\partial t} + \nabla \cdot (\alpha_s \mathbf{u}_s) = 0, \quad (2.17)$$

$$\frac{\partial \alpha_f}{\partial t} + \nabla \cdot (\alpha_f \mathbf{u}_f) = 0, \quad (2.18)$$

$$\frac{\partial}{\partial t} (\alpha_s \rho_s \mathbf{u}_s) + \nabla \cdot (\alpha_s \rho_s \mathbf{u}_s \otimes \mathbf{u}_s) = \alpha_s \rho_s \mathbf{f} - \nabla \cdot \alpha_s \mathbf{T}_s + p \nabla \alpha_s + \mathbf{M}_s, \quad (2.19)$$

$$\frac{\partial}{\partial t} (\alpha_f \rho_f \mathbf{u}_f) + \nabla \cdot (\alpha_f \rho_f \mathbf{u}_f \otimes \mathbf{u}_f) = \alpha_f \rho_f \mathbf{f} - \alpha_f \nabla p + \nabla \cdot \alpha_f \boldsymbol{\tau}_f + \mathbf{M}_f. \quad (2.20)$$

Equations (2.17) and (2.18) are the mass balance equations for the solid and the fluid, and equation (2.19) and (2.20) are the momentum balance equations for the solid and the fluid, respectively, where

$$\mathbf{M}_s = \frac{\alpha_s \alpha_f (\rho_s - \rho_f) g}{[\mathcal{U}_T \{ \mathcal{P} \mathcal{F}(Re_p) + (1 - \mathcal{P}) \mathcal{G}(Re_p) \}]^J} (\mathbf{u}_f - \mathbf{u}_s) |\mathbf{u}_f - \mathbf{u}_s|^{J-1} + \alpha_s \rho_f C_{VM} \left[ \left( \frac{\partial \mathbf{u}_f}{\partial t} + \mathbf{u}_f \cdot \nabla \mathbf{u}_f \right) - \left( \frac{\partial \mathbf{u}_s}{\partial t} + \mathbf{u}_s \cdot \nabla \mathbf{u}_s \right) \right], \quad (2.21)$$

$$|\mathbf{S}| = N \tan \phi, \quad T_{xx} = K_x T_{zz}, \quad T_{yy} = K_y T_{zz}, \quad (2.22)$$

$$\boldsymbol{\tau}_f = \eta_f [\nabla \mathbf{u}_f + (\nabla \mathbf{u}_f)^t] - \eta_f \frac{\mathcal{A}(\alpha_f)}{\alpha_f} [(\nabla \alpha_s)(\mathbf{u}_f - \mathbf{u}_s) + (\mathbf{u}_f - \mathbf{u}_s)(\nabla \alpha_s)], \quad (2.23)$$

and,  $\mathbf{M}_f = -\mathbf{M}_s$ .

In the above equations,  $\mathbf{S}$  is the shear stress,  $N$  is the normal load, and  $T_{xx}$ ,  $T_{yy}$  and  $T_{zz}$  are the normal stress components in the coordinate directions [30, 88, 89, 96, 109]. Similarly,  $p$  is the fluid pressure, and  $\mathcal{A}$  is the mobility of fluid at interface. There is strong coupling between the solid and the fluid momentum transfer both through the interfacial momentum transfer  $\mathbf{M}$ , which includes the viscous drag and the virtual mass force  $C_{VM}$ , and the enhanced non-Newtonian viscous fluid stress  $\boldsymbol{\tau}_f$ .  $C_{VM}$  can be considered differently depending upon the problem. One of the possibilities is  $C_{VM} = 0.5 \left( \frac{1 + 2\alpha_s}{\alpha_f} \right)$ . In case,  $\alpha_f$  is very small, we can choose some suitable numerical values. There are eight equations, with eight unknowns ( $u_s, v_s, w_s; u_f, v_f, w_f; \alpha_s, p$ ). So, the system is closed and can be solved numerically.

## 2.4.2 A Velocity-wise Two-Dimensional, Two-Phase Debris Flow Model

If we want to apply the full and velocity-wise three-dimensional model equations (2.17)-(2.20) to the large scale geographical mass flows consisting of  $10^6 - 10^{13} \text{ m}^3$  of materials, that typically travel tens to hundreds of kilometers in nature [15, 59, 74, 89, 104, 105], it is almost impossible to manage to simulate these flows within a short time and limited computational resources. Or, they require very high computational cost. This is even more complicated for the real two-phase mass flows. So, the best way to simulate the general geophysical mass flows is, for the sake of more feasible computation, to assume that the mass is incompressible and the flow depth is much smaller in comparison to its length, or aerial extents [45, 74, 89, 94]. This allows for the depth-averaging in the  $z$ -direction that drastically reduces the computational complexity and cost [19, 84]. Following this rational, here we present and utilize the depth-averaged two-phase debris flow model developed by Pudasaini (2012) [84]. Here, the model equations and their main physical aspects are briefly outlined.

Let  $(u_s, v_s)$  and  $(u_f, v_f)$  be the depth-averaged velocity components for the solid and fluid components in the down-slope ( $x$ ) and the cross-slope ( $y$ ) directions, respectively, and  $h$  be the total debris flow height. Then, the depth-averaged solid and fluid mass and the momentum balance equations in the down-slope and the cross-slope directions as proposed by Pudasaini (2012) [84] are as follows:

$$\frac{\partial}{\partial t}(\alpha_s h) + \frac{\partial}{\partial x}(\alpha_s h u_s) + \frac{\partial}{\partial y}(\alpha_s h v_s) = 0, \quad (2.24)$$

$$\frac{\partial}{\partial t}(\alpha_f h) + \frac{\partial}{\partial x}(\alpha_f h u_f) + \frac{\partial}{\partial y}(\alpha_f h v_f) = 0, \quad (2.25)$$

$$\begin{aligned} \frac{\partial}{\partial t} [\alpha_s h (u_s - \gamma \mathcal{C} (u_f - u_s))] + \frac{\partial}{\partial x} \left[ \alpha_s h \left( u_s^2 - \gamma \mathcal{C} (u_f^2 - u_s^2) + \frac{\beta_{x_s} h}{2} \right) \right] \\ + \frac{\partial}{\partial y} [\alpha_s h (u_s v_s - \gamma \mathcal{C} (u_f v_f - u_s v_s))] = h S_{x_s}, \end{aligned} \quad (2.26)$$

$$\begin{aligned} \frac{\partial}{\partial t} [\alpha_s h (v_s - \gamma \mathcal{C} (v_f - v_s))] + \frac{\partial}{\partial x} [\alpha_s h (u_s v_s - \gamma \mathcal{C} (u_f v_f - u_s v_s))] \\ + \frac{\partial}{\partial y} \left[ \alpha_s h \left( v_s^2 - \gamma \mathcal{C} (v_f^2 - v_s^2) + \frac{\beta_{y_s} h}{2} \right) \right] = h S_{y_s}, \end{aligned} \quad (2.27)$$

$$\begin{aligned} \frac{\partial}{\partial t} \left[ \alpha_f h \left( u_f + \frac{\alpha_s}{\alpha_f} \mathcal{C}(u_f - u_s) \right) \right] + \frac{\partial}{\partial x} \left[ \alpha_f h \left( u_f^2 + \frac{\alpha_s}{\alpha_f} \mathcal{C}(u_f^2 - u_s^2) + \frac{\beta_{x_f} h}{2} \right) \right] \\ + \frac{\partial}{\partial y} \left[ \alpha_f h \left( u_f v_f + \frac{\alpha_s}{\alpha_f} \mathcal{C}(u_f v_f - u_s v_s) \right) \right] = h S_{x_f}, \end{aligned} \quad (2.28)$$

$$\begin{aligned} \frac{\partial}{\partial t} \left[ \alpha_f h \left( v_f + \frac{\alpha_s}{\alpha_f} \mathcal{C}(v_f - v_s) \right) \right] + \frac{\partial}{\partial x} \left[ \alpha_f h \left( u_f v_f + \frac{\alpha_s}{\alpha_f} \mathcal{C}(u_f v_f - u_s v_s) \right) \right] \\ + \frac{\partial}{\partial y} \left[ \alpha_f h \left( v_f^2 + \frac{\alpha_s}{\alpha_f} \mathcal{C}(v_f^2 - v_s^2) + \frac{\beta_{y_f} h}{2} \right) \right] = h S_{y_f}. \end{aligned} \quad (2.29)$$

Here,

$$\beta_{x_s} = \varepsilon K_x p_{b_s}, \quad \beta_{y_s} = \varepsilon K_y p_{b_s}, \quad \beta_{x_f} = \beta_{y_f} = \varepsilon p_{b_f}, \quad p_{b_f} = -g^z, \quad p_{b_s} = (1 - \gamma) p_{b_f}.$$

The first two equations (2.24)-(2.25) are the depth-averaged mass balances for solid and fluid phases, respectively, and the last four equations are the depth-averaged momentum balances for solid (2.26)-(2.27); and fluid (2.28)-(2.29) in the  $x$ - and  $y$ -directions, respectively. The source terms are [84]:

$$\begin{aligned} S_{x_s} = \alpha_s \left[ g^x - \frac{u_s}{|\mathbf{u}_s|} \tan \delta p_{b_s} - \varepsilon p_{b_s} \frac{\partial b}{\partial x} \right] - \varepsilon \alpha_s \gamma p_{b_f} \left[ \frac{\partial h}{\partial x} + \frac{\partial b}{\partial x} \right] \\ + C_{DG}(u_f - u_s) \left| \mathbf{u}_f - \mathbf{u}_s \right|^{J-1}, \end{aligned} \quad (2.30)$$

$$\begin{aligned} S_{y_s} = \alpha_s \left[ g^y - \frac{v_s}{|\mathbf{u}_s|} \tan \delta p_{b_s} - \varepsilon p_{b_s} \frac{\partial b}{\partial y} \right] - \varepsilon \alpha_s \gamma p_{b_f} \left[ \frac{\partial h}{\partial y} + \frac{\partial b}{\partial y} \right] \\ + C_{DG}(v_f - v_s) \left| \mathbf{u}_f - \mathbf{u}_s \right|^{J-1}, \end{aligned} \quad (2.31)$$

$$\begin{aligned} S_{x_f} = \alpha_f \left[ g^x - \varepsilon \left[ \frac{1}{2} p_{b_f} \frac{h}{\alpha_f} \frac{\partial \alpha_s}{\partial x} + p_{b_f} \frac{\partial b}{\partial x} - \frac{1}{\alpha_f N_R} \left\{ 2 \frac{\partial^2 u_f}{\partial x^2} + \frac{\partial^2 v_f}{\partial y \partial x} + \frac{\partial^2 u_f}{\partial y^2} - \frac{\chi u_f}{\varepsilon^2 h^2} \right\} \right. \right. \\ \left. \left. + \frac{1}{\alpha_f N_{R_A}} \left\{ 2 \frac{\partial}{\partial x} \left( \frac{\partial \alpha_s}{\partial x} (u_f - u_s) \right) + \frac{\partial}{\partial y} \left( \frac{\partial \alpha_s}{\partial x} (v_f - v_s) + \frac{\partial \alpha_s}{\partial y} (u_f - u_s) \right) \right\} \right. \right. \\ \left. \left. - \frac{\xi \alpha_s (u_f - u_s)}{\varepsilon^2 \alpha_f N_{R_A} h^2} \right] \right] - \frac{1}{\gamma} C_{DG}(u_f - u_s) \left| \mathbf{u}_f - \mathbf{u}_s \right|^{J-1}, \end{aligned} \quad (2.32)$$

$$\begin{aligned}
S_{y_f} = & \alpha_f \left[ g^y - \varepsilon \left[ \frac{1}{2} p_{b_f} \frac{h}{\alpha_f} \frac{\partial \alpha_s}{\partial y} + p_{b_f} \frac{\partial b}{\partial y} - \frac{1}{\alpha_f N_R} \left\{ 2 \frac{\partial^2 v_f}{\partial y^2} + \frac{\partial^2 u_f}{\partial x \partial y} + \frac{\partial^2 v_f}{\partial x^2} - \frac{\chi v_f}{\varepsilon^2 h^2} \right\} \right. \right. \\
& + \left. \frac{1}{\alpha_f N_{R_A}} \left\{ 2 \frac{\partial}{\partial y} \left( \frac{\partial \alpha_s}{\partial y} (v_f - v_s) \right) + \frac{\partial}{\partial x} \left( \frac{\partial \alpha_s}{\partial y} (u_f - u_s) + \frac{\partial \alpha_s}{\partial x} (v_f - v_s) \right) \right\} \right. \\
& \left. \left. - \frac{\xi \alpha_s (v_f - v_s)}{\varepsilon^2 \alpha_f N_{R_A} h^2} \right] \right] - \frac{1}{\gamma} C_{DG} (v_f - v_s) \left| \mathbf{u}_f - \mathbf{u}_s \right|^{J-1}, \tag{2.33}
\end{aligned}$$

where,

$$\begin{aligned}
C_{DG} = & \frac{\alpha_s \alpha_f (1 - \gamma)}{[\varepsilon \mathcal{U}_T \{ \mathcal{P} \mathcal{F}(Re_p) + (1 - \mathcal{P}) \mathcal{G}(Re_p) \}]^J}, \quad \mathcal{F} = \frac{\gamma}{180} \left( \frac{\alpha_f}{\alpha_s} \right)^3 Re_p, \\
\mathcal{G} = & \alpha_f^{M(Re_p)-1}, \quad \gamma = \frac{\rho_f}{\rho_s}, \quad Re_p = \frac{\rho_f d \mathcal{U}_T}{\eta_f}, \quad N_R = \frac{\sqrt{g L H} \rho_f}{\alpha_f \eta_f}, \quad N_{R_A} = \frac{\sqrt{g L H} \rho_f}{\mathcal{A} \eta_f}. \tag{2.34}
\end{aligned}$$

In the above model equations (2.24)-(2.29),  $t$  is time,  $x$ ,  $y$  and  $z$  are coordinates along the flow directions, and  $g^x$ ,  $g^y$  and  $g^z$  are the components of gravitational acceleration.  $L$  and  $H$  are the typical length and depth of the flow,  $\varepsilon = H/L$  is the aspect ratio, and  $\mu = \tan \delta$  is the basal friction coefficient.  $K$  is the earth pressure coefficient (function of  $\delta$  and  $\phi$ , basal and internal friction angles of solid),  $C_{DG}$  is the generalized drag coefficient,  $J = 1$  or  $2$  represents linear or quadratic drag. Simple linear (laminar-type, at low velocity) or quadratic (turbulent-type, at high velocity) drag is associated with  $J = 1$  or  $2$ , respectively.  $\mathcal{U}_T$  is the terminal velocity of a particle and  $\mathcal{P} \in [0, 1]$  is a parameter which combines the solid-like ( $\mathcal{G}$ ) and fluid-like ( $\mathcal{F}$ ) drag contributions to flow resistance [84].  $p_{b_f}$  and  $p_{b_s}$  are the effective fluid and solid pressures.  $\gamma$  is the density ratio,  $\mathcal{C}$  is the virtual mass coefficient (solid particles induced kinetic energy of fluid phase),  $\eta_f$  is the fluid viscosity,  $M$  is a function of the particle Reynolds number ( $Re_p$ ),  $\chi$  includes vertical shearing of fluid velocity, and  $\xi$  takes into account different distributions of  $\alpha_s$ .  $\mathcal{A} = \mathcal{A}(\alpha_f)$  is the mobility of the fluid at the interface, and  $N_R$  and  $N_{R_A}$  are Reynolds numbers associated with the classical Newtonian, and enhanced non-Newtonian fluid viscous stresses.

As for single-phase [96] or mixture flows [44, 94] or two-fluid flows [24, 74], it is assumed that solid-fluid mixture, and the solid- and fluid-phase constituents separately satisfy the kinematic free-surface and bottom boundary conditions [84]. The top surface is traction-free, and Coulomb sliding (for solid) and no-slip (for fluid) conditions are satisfied at the flow base [44, 89, 94].

In (2.24)-(2.29) there are six equations, and six number of unknowns. So, these equations can be integrated numerically. Given the material parameters listed in (2.34) and the

basal topography,  $b = b(x, y)$ , equations (2.24)-(2.29) allow the debris flow depth  $h$ , volume fraction of the fluid  $\alpha_f$  (or solid  $\alpha_s$ ), and the depth-averaged velocity components for solid  $u_s$  and  $v_s$ , and for fluid  $u_f$  and  $v_f$ , parallel to the basal surface, to be computed as functions of space and time, once appropriate initial and (numerical) boundary conditions are prescribed [84].

## 2.5 Some Important Features of the Two-Phase Debris Flow Model Equations

The depth averaged model equations (2.24)-(2.29) are well structured hyperbolic-parabolic partial differential equations in conservative form. Following Pudasaini (2012) [84] and Pudasaini and Miller (2012a,b) [91, 92], some of the important features of the model are discussed below.

### 2.5.1 Inertial Terms

In (2.24)-(2.29), there are four important aspects in the inertial and pressure terms. For elaborated discussion, we refer to Pudasaini (2012) [84]:

- (i) The terms associated with  $\beta$  in the solid momentum equations (2.26) and (2.27) are responsible for the buoyancy-reduced lateral pressures. The solid load is reduced by the buoyancy force by the factor  $(1-\gamma)$ . When  $\gamma \rightarrow 1$ , the solid normal load vanishes and so hydraulic pressure gradient due to solids disappears. As the flow is neutrally buoyant for  $\gamma \rightarrow 1$ , the left hand sides of (2.26) and (2.27) are purely inertial. By analysing buoyant and non-buoyant flows, Pudasaini and Miller (2012b) [92] showed that buoyancy enhances flow mobility in two-phase debris flow. They demonstrated that buoyancy significantly affects the flow dynamics, and produces realistic run-out and depositional behaviors, and deposition morphology and mobility as observed in two-phase natural debris flows. As the simulation results were compatible with the physics of flow, they hypothesized that buoyancy is a mechanism that controls the mobilization of two-phase mass flows, and thus proper modeling of two-phase debris-flow should include buoyancy.
- (ii) The density ratio  $\gamma$  is present only in solid momentum equations (2.26) and (2.27).
- (iii) The presence of virtual mass coefficient  $\mathcal{C}$  provides a strong coupling between the solid  $(u_s, v_s)$  and the fluid  $(u_f, v_f)$  components. Not only the coupling occurs between the stream wise  $(u_s$  and  $u_f)$  and cross-stream velocity components  $(v_s$  and

$v_f$ ) but there are also interphase couplings between  $(u_s, v_s)$  and  $(u_f, v_f)$ . All the terms associated to  $\mathcal{C}$  vanish if there is no relative acceleration between the solid and fluid. Velocity couplings still remain effective in the left hand side through  $\mathcal{C}$  even if the source terms in the right hand side are neglected.

(iv) If the relative phase velocity is negligible (i.e., the solid and fluid components are interlocked), then all the terms associated with  $\mathcal{C}$  vanish. In this case, there will be only two momentum balance equations stream-wise and cross-stream-wise bulk momentum equations instead of four for the two-phases [45, 94].

## 2.5.2 Source Terms

As explained in Pudasaini (2012) [84], the source terms (2.30)-(2.31) for the solid momentum equations (2.26) and (2.27) have the following multiple contributions to force.

- The first three terms in the first square brackets are, respectively, the gravity, coulomb friction and topographic slope gradients.
- The terms associated with second square brackets are due to the buoyancy force which includes the free-surface and the basal surface gradients.
- The generalized drag terms  $C_{DG}$  associated with uniform flows, as described by last terms, strongly couple stream-wise solid and fluid velocities. The generalized drag is modeled by a linear combination of the fluid-like ( $\mathcal{F}$ ) and solid-like ( $\mathcal{G}$ ) drags with an interpolation parameter  $\mathcal{P}$ .  $\mathcal{F}$  represents fluid flow through a solid skeleton (e.g., granular-rich debris flows) (see, Takahashi (2007) [113]; Pudasaini (2012)[84]), whereas  $\mathcal{G}$  represents solid particles moving through fluid (e.g., particle-laden flows).  $\mathcal{F}$  and  $\mathcal{G}$  may have different degrees of importance depending on the nature of the flow. Therefore, the generalized drag coefficient is modeled by a linear combination of these contributions.

The source terms (2.32)-(2.33) for the fluid momentum equations (2.28) and (2.29) also have the multiple contribution to force [84].

- The first three terms in (2.32)-(2.33) emerge due to the gravity load applied to fluid phase (first term), the fluid pressure at the bed (second term) and the topographic slope (third term).
- The fourth group of terms associated with  $N_R$  appears from the viscous force contribution of the fluid phase. The fifth group of terms associated with  $N_{R_A}$  is due to

the fact that viscous shear stress is enhanced by the solid-volume-fraction gradient. These are the non-Newtonian viscous contributions.

- The last terms in equations (2.32) and (2.33) are due to drag force induced by relative phase velocities between the solid and fluid constituents.

### 2.5.3 Viscous Terms

When the solid grains in a debris mass are dispersed in a fluid and the grain - grain friction vanishes or the earth pressure coefficient  $K = 1$  (i.e.,  $\delta = 0$ ,  $\phi = 0$ ,  $\mathcal{F} = 0$ ), the pressure of viscous terms is effective as the shear stress terms for grains in both  $x$ - and  $y$ - directions  $-\alpha_s(u_s/|\mathbf{u}_s|) \tan \delta p_{b_s}$  and  $-\alpha_s(v_s/|\mathbf{u}_s|) \tan \delta p_{b_s}$  can be ignored. This results in buoyant grain flows which are opposed by viscous, and virtual mass forces [84]. Due to buoyancy, the basal solid stress  $p_{b_s}$  is written in terms of the fluid pressure,  $p_{b_f}$ , that reflects the buoyancy reduced solid load. If  $\gamma = 1$ , i.e., the debris mass is neutrally buoyant, the basal solid weight ( $p_{b_s}$ ) vanishes [84, 91, 92]. In this situation Coulomb friction disappears, the generalized drag coefficient  $C_{DG}$  becomes zero and also the basal slope has no effect on solid grains [85]. So, only effective solid forces are due to gravity and the force associated with buoyancy. But, in case of fluid phase, the force induced by the solid-volume fraction gradient ( $\nabla\alpha_s$ ) is also effective besides the viscous and gravity forces. The Newtonian and non-Newtonian viscous terms (associated with  $N_R$  and  $N_{R_A}$ ) are equally important as compared to the basal gradient terms ( $\varepsilon\alpha_s p_{b_s} \partial b/\partial x$ ) and ( $\varepsilon\alpha_s p_{b_s} \partial b/\partial y$ ) and the pressure gradient terms  $\partial(\alpha_s\beta_{x_s} h^2/2)/\partial x$  and  $\partial(\alpha_s\beta_{y_s} h^2/2)/\partial y$  in the solid momentum equations (2.26), (2.27), (2.30), (2.31) and similar terms in the remaining fluid momentum equations. The importance of such terms is revealed by Savage and Hutter (1989) [96], Pudasaini and Hutter (2003, 2007) [88, 89], and Pitman and Le (2005) [74]. Since the viscosity  $\eta_f$  as present in equation (2.34) is in the denominator of  $N_R$  and  $N_{R_A}$ , the influence of the terms associated with  $\varepsilon$  in the fluid momentum equations increases along with the increase of the magnitude of  $(u_f - u_s)$  [84].

### 2.5.4 Drag Coefficients

The generalized drag terms play important role in the dynamics of two-phase debris flows as these coefficients explicitly incorporate many essential physical parameters, including the volume fractions of the solid and fluid, the solid and fluid densities, terminal velocity of solid particles, particle diameter, and fluid viscosity [84]. The parameter  $\mathcal{P}$  can play a crucial role to fit the data and the model calibration. Two limiting cases are of particular importance:  $\mathcal{P} = 0$  is more suitable when solid particles are moving through a fluid.

In contrast,  $\mathcal{P} = 1$  is more suitable for flows of fluids through dense packing of grains [57, 71, 72, 74]. Thus, the generalized drag coefficient proposed by Pudasaini (2012) offers the opportunity to simulate a wide spectrum of geophysical mass flows, and also possibly industrial mixture flows [84]. By setting  $\mathcal{P} = 0$  and  $J = 1$ , one recovers the drag coefficient of Pitman and Le (2005) [74], and  $\mathcal{P} = 1$  and  $J = 1$  corresponds to the drag coefficient in Pailha and Pouliquen (2009) [72]. This also shows that the model equations proposed by Pudasaini (2012) are more general.

### 2.5.5 Diffusion of Solid Volume Fraction

In (2.32), the expression associated with  $N_{R_A}$  and inside braces can be written in the form

$$h \left[ \frac{\partial}{\partial x} \left\{ \frac{2}{N_{R_A}} (u_f - u_s) \frac{\partial \alpha_s}{\partial x} \right\} + \frac{\partial}{\partial y} \left\{ \frac{1}{N_{R_A}} (v_f - v_s) \frac{\partial \alpha_s}{\partial x} \right\} + \frac{\partial}{\partial y} \left\{ \frac{1}{N_{R_A}} (u_f - u_s) \frac{\partial \alpha_s}{\partial y} \right\} \right].$$

The quantities  $(u_f - u_s)/N_{R_A}$  and  $(v_f - v_s)/N_{R_A}$  are velocity-dependent dynamic diffusion coefficients for the solid volume fraction  $\alpha_s$  [84, 91]. So, the intensity of the diffusion of  $\alpha_s$  depends mainly on the magnitude of the relative velocity of solid with respect to the fluid. Clearly, there is no diffusion of  $\alpha_s$  in the case:  $u_f - u_s = v_f - v_s = 0$ , i.e., effectively single-phase model. Most of the previous models did not take into account of the evolving solid concentration. The diffusion of  $\alpha_s$  is inversely proportional to  $N_{R_A}$ . The advection of  $\alpha_s$  has also been included in the inertial terms in (2.24) and (2.25) as a field variable, and there also appears  $\alpha_s$  in the mass balance equations (2.24) and (2.25).

### 2.5.6 Reduction to Other Relatively Simple Models

As mentioned in Pudasaini (2012) [84], the model presented in (2.24)-(2.29) unifies the three pioneering theories in geophysical mass flows, the dry granular avalanche model of Savage and Hutter (1989) [96], the debris-flow model of Iverson (1997) [44] and Iverson and Denlinger (2001) [45], and the two-fluid debris-flow model of Pitman and Le (2005) [74], and result in a generalized two-phase debris-flow model. As special cases of the general debris flow model [84], one recovers these relatively simple models for debris flows and avalanches. For the detailed discussions on the similarities and differences between the reduced model and the relatively simple classical models, we refer to Pudasaini (2012) [84]. However, here we outline some important aspects in brief.

#### A. Two Fluid Model of Pitman and Le (2005)

The model equations (2.24)-(2.29) and the respective source terms (2.30)-(2.33) reduce to those similar to Pitman and Le (2005) model [74], if both types of viscous terms

(associated with  $N_R$  and  $N_{R_A}$ ), and the diffusion of solid volume fractions are neglected, the virtual mass coefficient  $\mathcal{C} = 0$ , and the interpolation parameter  $\mathcal{P} = 0$  are taken and  $J = 1$  (i.e., only the linear drag force) is considered. In this case, solid-fluid interaction is only through the drag terms, whereas it is through the generalized drag ( $C_{DG}$ ), virtual mass force ( $\mathcal{C}$ ) and the solid-volume-fraction-gradient enhanced viscous terms in Pudasaini (2012) model [84]:

$$\frac{\partial}{\partial t} [\alpha_s h u_s] + \frac{\partial}{\partial x} \left[ \alpha_s h \left( u_s^2 + \frac{\beta_{x_s} h}{2} \right) \right] + \frac{\partial}{\partial y} [\alpha_s h u_s v_s] = h S_{x_s}, \quad (2.35)$$

$$\frac{\partial}{\partial t} [\alpha_s h v_s] + \frac{\partial}{\partial x} [\alpha_s h u_s v_s] + \frac{\partial}{\partial y} \left[ \alpha_s h \left( v_s^2 + \beta_{y_s} \frac{h}{2} \right) \right] = h S_{y_s}, \quad (2.36)$$

$$\frac{\partial}{\partial t} [\alpha_f h u_f] + \frac{\partial}{\partial x} [\alpha_f h u_f^2] + \frac{\partial}{\partial y} [\alpha_f h u_f v_f] = h S_{x_f}, \quad (2.37)$$

$$\frac{\partial}{\partial t} [\alpha_f h v_f] + \frac{\partial}{\partial x} [\alpha_f h u_f v_f] + \frac{\partial}{\partial y} [\alpha_f h v_f^2] = h S_{y_f}, \quad (2.38)$$

where the source terms are:

$$S_{x_s} = \alpha_s \left[ g^x - \frac{u_s}{|\mathbf{u}_s|} \tan \delta p_{b_s} - \varepsilon p_{b_s} \frac{\partial b}{\partial x} \right] - \varepsilon \alpha_s \gamma p_{b_f} \left[ \frac{\partial h}{\partial x} + \frac{\partial b}{\partial x} \right] + C_{DG}(u_f - u_s), \quad (2.39)$$

$$S_{y_s} = \alpha_s \left[ g^y - \frac{v_s}{|\mathbf{u}_s|} \tan \delta p_{b_s} - \varepsilon p_{b_s} \frac{\partial b}{\partial y} \right] - \varepsilon \alpha_s \gamma p_{b_f} \left[ \frac{\partial h}{\partial y} + \frac{\partial b}{\partial y} \right] + C_{DG}(v_f - v_s), \quad (2.40)$$

$$S_{x_f} = \alpha_f \left[ g^x - \varepsilon \left\{ \frac{1}{h} \frac{\partial}{\partial x} \left( \frac{h^2}{2} p_{b_f} \right) + p_{b_f} \frac{\partial b}{\partial x} \right\} \right] - \frac{1}{\gamma} C_{DG}(u_f - u_s), \quad (2.41)$$

$$S_{y_f} = \alpha_f \left[ g^y - \varepsilon \left\{ \frac{1}{h} \frac{\partial}{\partial y} \left( \frac{h^2}{2} p_{b_f} \right) + p_{b_f} \frac{\partial b}{\partial y} \right\} \right] - \frac{1}{\gamma} C_{DG}(v_f - v_s). \quad (2.42)$$

Here,

$$\beta_{x_s} = \varepsilon K_x p_{b_s}, \quad \beta_{y_s} = \varepsilon K_y p_{b_s}, \quad p_{b_f} = -g^z, \quad p_{b_s} = (1 - \gamma) p_{b_f},$$

$$C_{DG} = \frac{\alpha_s \alpha_f (1 - \gamma)}{\varepsilon \mathcal{U}_T \alpha_f^{M(Re_p - 1)}}, \quad \gamma = \frac{\rho_f}{\rho_s}, \quad Re_p = \frac{\rho_f d \mathcal{U}_T}{\eta_f}.$$

Yet, there are many differences in this reduced model and that in Pitman and Le (2005)[74].

In Pudasaini (2012) model [84],

- Generalized drag coefficients are developed and utilized.
- Basal slope effects are also taken into account in the fluid momentum equations.
- Pressure induced by topography is included.

For further details, we refer to Pudasaini (2012) [84].

### B. Mixture Model of Iverson and Denlinger (2001) and Pudasaini et al. (2005)

If we set the solid and fluid velocities equal (i.e.,  $u_s = u_f = u$  and  $v_f = v_s = v$ ) [44, 45, 94], the model equations (2.24)-(2.29) reduce to the following single mass balance equation (2.43) and two momentum balance equations(2.44) and (2.45) for the bulk in  $x$ - and  $y$ -directions respectively:

$$\frac{\partial h}{\partial t} + \frac{\partial}{\partial x}(hu) + \frac{\partial}{\partial y}(hv) = 0, \quad (2.43)$$

$$\frac{\partial}{\partial t}(hu) + \frac{\partial}{\partial x} \left[ hu^2 + \alpha_s \beta_x \frac{h^2}{2} \right] + \frac{\partial}{\partial y} [huv] = hS_x, \quad (2.44)$$

$$\frac{\partial}{\partial t}(hv) + \frac{\partial}{\partial x} [huv] + \frac{\partial}{\partial y} \left[ hv^2 + \alpha_s \beta_y \frac{h^2}{2} \right] = hS_y, \quad (2.45)$$

where  $u$  and  $v$  are the  $x$ - and  $y$ -velocity components of the bulk. The source terms are

$$S_x = S_{x_s} + S_{x_f}, \quad S_y = S_{y_s} + S_{y_f}, \quad (2.46)$$

$$S_{x_s} = \alpha_s \left[ g^x - \frac{u}{|\mathbf{u}|} \tan \delta p_{b_s} - \varepsilon p_{b_s} \frac{\partial b}{\partial x} \right] - \varepsilon \alpha_s \gamma p_{b_f} \left[ \frac{\partial h}{\partial x} + \frac{\partial b}{\partial x} \right], \quad (2.47)$$

$$S_{y_s} = \alpha_s \left[ g^y - \frac{v}{|\mathbf{u}|} \tan \delta p_{b_s} - \varepsilon p_{b_s} \frac{\partial b}{\partial y} \right] - \varepsilon \alpha_s \gamma p_{b_f} \left[ \frac{\partial h}{\partial y} + \frac{\partial b}{\partial y} \right], \quad (2.48)$$

$$S_{x_f} = \alpha_f \left[ g^x - \varepsilon \left[ \frac{1}{h} \frac{\partial}{\partial x} \left( \frac{h^2}{2} p_{b_f} \right) + p_{b_f} \frac{\partial b}{\partial x} - \frac{1}{\alpha_f N_R} \left\{ 2 \frac{\partial^2 u}{\partial x^2} + \frac{\partial^2 v}{\partial y \partial x} + \frac{\partial^2 u}{\partial y^2} - \frac{\chi u}{\varepsilon^2 h^2} \right\} \right] \right], \quad (2.49)$$

$$S_{y_f} = \alpha_f \left[ g^y - \varepsilon \left[ \frac{1}{h} \frac{\partial}{\partial y} \left( \frac{h^2}{2} p_{b_f} \right) + p_{b_f} \frac{\partial b}{\partial y} - \frac{1}{\alpha_f N_R} \left\{ 2 \frac{\partial^2 v}{\partial y^2} + \frac{\partial^2 u}{\partial x \partial y} + \frac{\partial^2 v}{\partial x^2} - \frac{\chi v}{\varepsilon^2 h^2} \right\} \right] \right], \quad (2.50)$$

where,

$$\beta_x = \varepsilon K_x p_{b_s}, \quad \beta_y = \varepsilon K_y p_{b_s}, \quad p_{b_f} = -g^z, \quad p_{b_s} = (1 - \gamma) p_{b_f},$$

$$\gamma = \frac{\rho_f}{\rho_s}, \quad N_R = \sqrt{g L H} \rho_f / \alpha_f \eta_f.$$

These equations appear to be the important extensions of Coulomb classical mixture model of Iverson and Denlinger (2001) and Pudasaini et al. (2005) [45, 84, 94]. Still, in the reduced model (2.43)-(2.50), the following aspects are included that are not present in the classical models:

- $(1 - \gamma)$  includes buoyancy force.
- Different physical properties of the constituents  $\alpha_s, \alpha_f$ , and the physical parameters  $\eta_f$  and  $\gamma$  are involved.
- The buoyancy reduced (solid) normal loads are present in the lateral pressures associated with  $\beta$ .

For further details, we refer to Pudasaini (2012) [84].

This reduced system (2.43)-(2.50) recovers the mixture models of Iverson and Denlinger (2001) and Pudasaini et al. (2005) by

- (i) realizing  $(1 - \Lambda_f)$  by  $\alpha_s$ ,
- (ii) setting  $\gamma = 0$ , and
- (iii) replacing the fluid density  $\rho_f$  by the bulk density  $\rho$  in  $N_R$ .

### C. Granular Flow and Avalanche Model

If we further set  $\alpha_s = 1$  (i.e.,  $\alpha_f = 0$ ) and  $\gamma = 0$  (i.e., fluid phase is absent) in the above mixture model (2.43)-(2.50), it further reduces to the model for dry granular flows or avalanches (Savage and Hutter (1989) [96], Gray et al. (1999) [30], and Pudasaini and Hutter (2003) [88]) and for mass and momentum balance equations are:

$$\frac{\partial h}{\partial t} + \frac{\partial}{\partial x}(hu) + \frac{\partial}{\partial y}(hv) = 0, \quad (2.51)$$

$$\frac{\partial}{\partial t}[hu] + \frac{\partial}{\partial x} \left[ hu^2 + \beta_x \frac{h^2}{2} \right] + \frac{\partial}{\partial y}[huv] = hS_x, \quad (2.52)$$

$$\frac{\partial}{\partial t}[hv] + \frac{\partial}{\partial x}[huv] + \frac{\partial}{\partial y} \left[ hv^2 + \beta_y \frac{h^2}{2} \right] = hS_y, \quad (2.53)$$

where, the source, pressures and other parameters involved in these reduced equations are

$$S_x = \left[ g^x - \frac{u}{|\mathbf{u}|} \tan \delta p_{b_s} - \varepsilon p_{b_s} \frac{\partial b}{\partial x} \right], \quad (2.54)$$

$$S_y = \left[ g^y - \frac{v}{|\mathbf{u}|} \tan \delta p_{b_s} - \varepsilon p_{b_s} \frac{\partial b}{\partial y} \right], \quad (2.55)$$

$$\beta_x = \varepsilon K_x p_{b_s}, \quad \beta_y = \varepsilon K_y p_{b_s}, \quad p_{b_f} = -g^z.$$

Instead of  $\alpha_s = 1$ , if we set  $\alpha_f = 1$  (i.e., no solid phase), the reduced mixture model would further reduce to that for the viscous fluid flow, akin to Navier-Stokes equations, and equations modeling hydraulics and tsunami waves [84, 92, 85].

These reductions A, B, and C into previous models show that the general two-phase debris flow model due to Pudasaini (2012) [84] and even the reduced models (A-C) are more general than the respective previous models.

# Chapter 3

## High-Resolution Numerical Integrations for Mass Flows

<sup>1</sup>Geophysical mass flows such as landslides, avalanches and debris flows, and also tsunamis and granular flows are modeled by some partial differential equations that involve mass and momentum balance equations. In this chapter, we give a brief introduction on different types of partial differential equations (PDEs), including, elliptic, parabolic and hyperbolic equations. In general, they can also be of mixed type, e.g., hyperbolic-parabolic [84, 89]. PDEs are characterized by the eigenvalues of the systems. Along with the development of two dimensional numerical schemes, we mainly focus on presenting the two dimensional, high-resolution shock capturing methods that has been applied to the general two-phase debris flow model.

### 3.1 Elliptic, Parabolic and Hyperbolic Equations

The general second-order partial differential equation (PDE) in two independent variables  $x$  and  $y$  is in the form [21, 79]

$$Au_{xx} + 2Bu_{xy} + Cu_{yy} + 2Du_x + 2Eu_y + F = 0, \quad (3.1)$$

where  $A$ ,  $B$ ,  $C$ ,  $D$ ,  $E$  and  $F$  may depend on  $x$  and  $y$  and the suffices on the dependent variable  $u$  denote the partial differentiation. If  $A^2 + B^2 + C^2 > 0$  over a region in the  $xy$  plane, the PDE is of second-order in that region. The PDE (3.1) can be classified as [21, 79]:

- elliptic, if  $B^2 - AC < 0$ ,

---

<sup>1</sup>This chapter closely follows Chapter 7 and Chapter 8 in the book *Avalanche Dynamics* by Pudasaini and Hutter (2007) [89].

- parabolic, if  $B^2 - AC = 0$ , and
- hyperbolic, if  $B^2 - AC > 0$ .

If there are  $n$  independent variables, say  $x_1, x_2, \dots, x_n$ , then, a general linear partial differential equation of second order takes the form

$$Lu = \sum_{i=1}^n \sum_{j=1}^n a_{ij} \frac{\partial^2 u}{\partial x_i \partial x_j} + \dots = 0. \quad (3.2)$$

Now, the classification depends upon the signature of the eigenvalues of the coefficient matrix  $(a_{ij})_{n \times n}$ . The PDE (3.2) will be [21, 79]:

- elliptic, if the eigenvalues are all positive or all negative,
- parabolic, if the eigenvalues are all positive or all negative, and at least one of them is zero, and
- hyperbolic, if there is only one negative eigenvalue and all the rest are positive, or there is only one positive eigenvalue and all the rest are negative.

This classification is valid for scalar partial differential equations [87]. However, this classification can be extended to a system of PDEs [87].

The model equations (2.24)-(2.29) take the form of a set of well-structured hyperbolic-parabolic equations in conservative form so as to include advective-diffusive process of the two-phase mass flow [84]. As the model equations have to address the large and rapid deformations of the constituents in the two-phase debris flow, the classical numerical methods are not capable of absorbing the shocks or the large gradients in flow dynamical variables [85, 89, 92]. So, the model equations should be integrated numerically by using high resolution shock capturing numerical methods.

## 3.2 Various Numerical Schemes for Mass Flows

The numerical techniques for solving the dynamical mass flow equations have their history developed from simple to complex. It began with plane (chute) flows [30, 31, 96, 97] and when later sidewise confinement was relaxed [30, 31, 106, 117], the mass flow as a two-dimensional flow could be also be treated [89]. For different geophysical mass flows, the huge deformations and rapid motions are to be considered along with the resulting shocks and their propagations. So, classical numerical schemes were unable to capture the shock. To tackle with the sudden changes in the mass flow, modern numerical methods

were flourished [89, 106, 109].

Savage and Hutter (1989) [96] introduced finite difference schemes, namely Lagrangean and the other Eulerian type, to solve spatially one dimensional model equations describing the finite mass granular avalanche flow down a rough incline [89]. Lagrangean scheme was found to be simple to use and sufficient enough to predict the observable behavior of the flow [89]. A fixed spatial grid that extends upstream and downstream of the moving pile was used in Eulerian approach that yield finite velocities upstream and downstream of the pile even at those parts of the bed where the material depth was zero. This created sudden changes in the velocities corresponding to the front and rear of the pile, which destroys the stability in numerical integration. Artificial viscosity was applied to diffuse the instability but the velocities in the regions outside of that occupied by the pile began to affect the results in the region of the pile itself [89]. To overcome such difficulties, a Lagrangean scheme was implemented. The Lagrangean approach involved the computational grid which advected along with the moving material itself [89]. This approach added more in the simplicity, efficiency and reliability of the numerical integration. Yet it was unable to capture the singularities.

Greve and Hutter (1993) [31] also used Lagrangean scheme to compute, numerically, the avalanche height, velocity distribution, the front, the rear and intermediate positions of the maximum avalanche height for different numerical and material parameter values for a motion of a granular avalanche in a convex and concave chute [89]. Some traditional numerical schemes include upwind method and some second order schemes include the Lax-Wendroff method and Upwind beam-warming method. Traditional second-order central differencing methods cannot solve the problem of oscillations in the numerical solution for physical problems with steep gradients of the flow variables.

It is quite natural to observe the shock formations in geophysical mass flows encountering a sudden change in topography, especially when the velocity becomes subcritical from supercritical state [89, 116]. So it justifies the necessity of high resolution numerical techniques that are able to resolve the steep gradients and moving fronts [89, 106, 107, 116].

Generally, second-order Lagrangean finite difference methods do not have total variation diminishing properties. So, they require additional numerical diffusion. The Lagrangean integration technique is suitable particularly for two-dimensional mass flow problems, because the grid is advecting, that makes the handling of marginal lines along which the flowing mass thickness must vanish, easy. Furthermore, the Lagrangean integration technique with second order accuracy in the spatial finite difference operators and leapfrog

integration procedures in time produces accurate results, in case when only dilatational or, only compressional flows appear [89].

This integration scheme was developed by Koch et al. (1994) and Weiland et al. (1999) [56, 117] in the case of avalanche flow. The two dimensional Lagrangean numerical scheme used by Koch et al. (1999) [56] was then improved and further extended by Gray et al. (1999) [30] to study of the motion of free surface flow of granular avalanches over complex basal topography. Weiland et al. (1999) [117] implemented a mixed type of finite-volume finite difference scheme, explicit in time and spatially two-dimensional Lagrangean scheme to solve depth-averaged equations of the motion developed by Gray et al. (1991)[30]. For this, the avalanche is discretized into a finite number of triangular elements with moving grid that deforms along with its motion [89].

### 3.3 Two-Dimensional NOC Schemes

#### A Brief Description of Predictor-Corrector Solver:

The non-oscillatory central (NOC) differencing scheme proposed by Nessyahu and Tadmor [68] is a one-dimensional second order extension of Lax-Friedrichs scheme [58]. Two dimensional extension of the NOC scheme was proposed by Jiang and Tadmor [46] followed by some improvements by Lie and Noelle (2003) [61]. In numerical schemes, only values of the cell averages are available. So, with the concept of high-resolution methods, the distribution of the physical variables over the cell is reconstructed. As in the one-dimensional case, the two-dimensional NOC scheme is a predictor-corrector method which consists of two steps [89]:

- (i) The grid values are first predicted according to the non-oscillatory reconstructions from the given cell averages.
- (ii) As a corrector step, a staggered averaging is introduced, together with the predicted mid-values, to determine the full evolution of these averages.

This gives in a high-order, non-oscillatory central scheme.

The  $x$ - $y$ - $t$  space is discretised by choosing uniform and stationary spatial mesh width  $\Delta x$ ,  $\Delta y$ , and time step  $\Delta t$ . The discrete mesh points are denoted by  $(x_p, y_q, t^n)$ , and are defined as  $x_p = p\Delta x$ ,  $p = 0, 1, 2, \dots$ ;  $y_q = q\Delta y$ ,  $q = 0, 1, 2, \dots$ ;  $t^n = n\Delta t$ ,  $n = 0, 1, 2, \dots$ , where the mesh cell  $(x_p, y_q)$  is bounded by the boundaries  $(x_{p\pm\frac{1}{2}}, y_{q\pm\frac{1}{2}})$ , where  $x_{p+\frac{1}{2}} = x_p + \frac{\Delta x}{2}$ , etc. Computation of the staggered averages at  $(x_{p\pm\frac{1}{2}}, y_{q\pm\frac{1}{2}}, t^{n+1})$  by the cell averages at  $(x_p, y_q, t^n)$  is the main feature of the NOC scheme, see, Fig.3.1a.

We begin with a general two-dimensional conservation law:

$$\frac{\partial w}{\partial t} + \frac{\partial f(w)}{\partial x} + \frac{\partial g(w)}{\partial y} = s(w) \quad (3.3)$$

with initial value  $w(x, y, t = 0) = w_0(x, y)$ . Let  $C_{p,q}$  be the cell covering the region

$$C_{p,q} = \left\{ (x, y) \left| |x - x_p| \leq \frac{\Delta x}{2}, |y - y_q| \leq \frac{\Delta y}{2} \right. \right\}. \quad (3.4)$$

Next, let  $U_{p,q}^n$  denote the cell average over this region at time  $t^n$ , and

$$\tilde{w}_{p,q}(x, y, t^n) = U_{p,q}^n + \sigma_{p,q}^x(x - x_p) + \sigma_{p,q}^y(y - y_q) \quad (3.5)$$

be a piecewise linear reconstruction over the cell, where  $\sigma_{p,q}^x$  and  $\sigma_{p,q}^y$  denote the discrete slopes of  $U$  in the  $x$ - and  $y$ -directions which are decided by a TVD-limiter [60], or a central, Essentially Non-Oscillatory (ENO) cell reconstruction [33]. They are the TVD slope limiters in TVD schemes and are the mean slopes of the high-order interpolations over the cells in ENO schemes [84]. The piecewise linear cell reconstructions are at most second-order accurate. With the help of ENO schemes, it is possible to construct a polynomial approximation over the cell that is accurate pointwise to higher order [89]. In the ENO schemes, first developed by Harten (1983) [33], the cell reconstructions are approximated by an essentially non-oscillatory high-order accurate polynomial interpolation of a piecewise smooth function from its cell averages. So, it is a generalisation of the TVD method of piecewise linear cell reconstructions [33, 89, 116].

Let  $U_{p+1/2, q+1/2}$  be the staggered average. Then, integration of (3.3) over  $C_{p+1/2, q+1/2} \times [t^n, t^{n+1}]$  gives

$$\begin{aligned} U_{p+1/2, q+1/2}^{n+1} &= \frac{1}{\Delta x \Delta y} \int_{x_p}^{x_{p+1}} \int_{y_q}^{y_{q+1}} w(x, y, t^n) dy dx \\ &- \frac{1}{\Delta x \Delta y} \int_{t^n}^{t^{n+1}} \int_{y_q}^{y_{q+1}} (f(x_{p+1}, y, t) - f(x_p, y, t)) dy dt \\ &- \frac{1}{\Delta x \Delta y} \int_{t^n}^{t^{n+1}} \int_{x_p}^{x_{p+1}} (g(x, y_{q+1}, t) - g(x, y_q, t)) dx dt \\ &+ \frac{1}{\Delta x \Delta y} \int_{t^n}^{t^{n+1}} \int_{x_p}^{x_{p+1}} \int_{y_q}^{y_{q+1}} s(x, y, t) dy dx dt. \end{aligned} \quad (3.6)$$

Then, we can split the first integral on the right-hand side of (3.6) into the four parts as:

$$\begin{aligned} \int_{x_p}^{x_{p+1}} \int_{y_q}^{y_{q+1}} w(x, y, t^n) dx dy &= \iint_{C_{p,q}^{SW}} w(x, y, t^n) dx dy + \iint_{C_{p+1,q}^{SE}} w(x, y, t^n) dx dy \\ &+ \iint_{C_{p+1,q+1}^{NE}} w(x, y, t^n) dx dy + \iint_{C_{p,q+1}^{NW}} w(x, y, t^n) dx dy. \end{aligned} \quad (3.7)$$

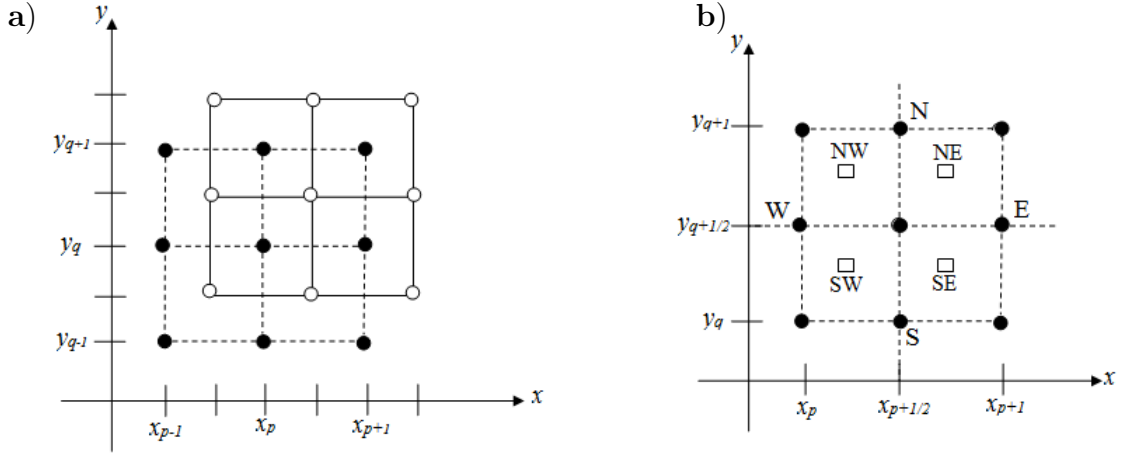


Figure 3.1: **a)** The two-dimensional NOC scheme with the staggered grid: The staggered averages at  $(x_{p\pm 1/2}, y_{q\pm 1/2}, t^{n+1})$ , denoted by “o”, are computed by the averages at  $(x_p, y_q, t^n)$ , represented by “•”. **b)** The two-dimensional NOC scheme and a floor plan of the staggered grid, where the cell  $C_{p+1/2, q+1/2}$  consists of four intersecting cells  $C_{p,q}$ ,  $C_{p+1,q}$ ,  $C_{p+1,q+1}$  and  $C_{p,q+1}$ , denoted by  $C_{p,q}^{SW}$ ,  $C_{p+1,q}^{SE}$ ,  $C_{p+1,q+1}^{NE}$  and  $C_{p,q+1}^{NW}$ , respectively. “•” indicates the computed cell center and “□” denotes the center of the intersecting cells. The numerical fluxes are considered as the values across the corresponding faces, East (E), North (N), West (W) and South (S), respectively. (The figure has been reproduced from Pudasaini and Hutter (2007) [89]).

As shown in Fig. 3.1b, the four cells are defined by:

$$\begin{aligned}
 C_{p,q}^{SW} &:= C_{p+1/2, q+1/2} \cap C_{p,q}, \\
 C_{p+1,q}^{SE} &:= C_{p+1/2, q+1/2} \cap C_{p+1,q}, \\
 C_{p+1,q+1}^{NE} &:= C_{p+1/2, q+1/2} \cap C_{p+1,q+1}, \\
 C_{p,q+1}^{NW} &:= C_{p+1/2, q+1/2} \cap C_{p,q+1}.
 \end{aligned} \tag{3.8}$$

If we begin with the intersection cell  $C_{p,q}^{SW}$ , by using the reconstructed polynomial (3.5) and the discrete slopes  $\sigma_{j,k}^x$  and  $\sigma_{j,k}^y$  of  $U$ , the first term on the right-hand side of (3.7) can be written as [89]:

$$\frac{1}{4}U_{p,q}^n + \frac{\Delta x}{16}\sigma_{p,q}^x + \frac{\Delta y}{16}\sigma_{p,q}^y. \tag{3.9}$$

The same procedure applied in counterclockwise direction results the remaining terms on the right-hand side of (3.7) as [89]:

$$\begin{aligned}
& \frac{1}{4}U_{p+1,q}^n - \frac{\Delta x}{16}\sigma_{p+1,q}^x + \frac{\Delta y}{16}\sigma_{p+1,q}^y, \\
& \frac{1}{4}U_{p+1,q+1}^n - \frac{\Delta x}{16}\sigma_{p+1,q+1}^x - \frac{\Delta y}{16}\sigma_{p+1,q+1}^y, \\
& \frac{1}{4}U_{p,q+1}^n + \frac{\Delta x}{16}\sigma_{p,q+1}^x - \frac{\Delta y}{16}\sigma_{p,q+1}^y.
\end{aligned} \tag{3.10}$$

In the next step, we compute numerical fluxes corresponding to the points  $x_{p+1}, x_p, y_{q+1}, y_q$  for (3.6) on the east and west surfaces for the flux function  $f$ , and north and south surfaces for the flux function  $g$ , see Fig. 3.1b. We approximate them by the midpoint quadrature rule for second-order accuracy by integrating with respect to time along with the second-order rectangular rule for the spatial integration across the corresponding face. So, the flux at the east face is:

$$\frac{1}{2} \frac{\Delta t}{\Delta x} \left\{ f \left( U_{p+1,q}^{n+1/2} \right) + f \left( U_{p+1,q+1}^{n+1/2} \right) \right\}. \tag{3.11}$$

Similarly, the other three fluxes in the counterclockwise direction are [89]:

$$\begin{aligned}
& \frac{1}{2} \frac{\Delta t}{\Delta y} \left\{ g \left( U_{p,q+1}^{n+1/2} \right) + g \left( U_{p+1,q+1}^{n+1/2} \right) \right\}, \\
& \frac{1}{2} \frac{\Delta t}{\Delta x} \left\{ f \left( U_{p,q}^{n+1/2} \right) + f \left( U_{p,q+1}^{n+1/2} \right) \right\}, \\
& \frac{1}{2} \frac{\Delta t}{\Delta y} \left\{ g \left( U_{p,q}^{n+1/2} \right) + g \left( U_{p+1,q}^{n+1/2} \right) \right\}.
\end{aligned} \tag{3.12}$$

**Predictor-Step:** Now, by employing the conservation law (3.3) to compute  $U_{j,k}^{n+1/2}$ , equations (3.11)–(3.12) yield [46, 68, 89]:

$$U_{j,k}^{n+1/2} = U_{j,k}^n - \frac{\Delta t}{2} (\sigma^f)_{j,k}^n - \frac{\Delta t}{2} (\sigma^g)_{j,k}^n + \frac{\Delta t}{2} s(U_{j,k}^n), \tag{3.13}$$

where  $\sigma^f$  and  $\sigma^g$  are the discrete slopes of the fluxes  $f$  and  $g$ . These can be determined by the non-oscillatory TVD limiters or ENO interpolations, or by the Jacobians,

$$(\sigma^f)_{j,k}^n = \left( \frac{\partial f(w)}{\partial w} \right)_{j,k}^n \sigma_{j,k}^x, \quad (\sigma^g)_{j,k}^n = \left( \frac{\partial g(w)}{\partial w} \right)_{j,k}^n \sigma_{j,k}^y, \tag{3.14}$$

where  $\sigma_{j,k}^x$  and  $\sigma_{j,k}^y$  are the discrete slopes of  $U$  [46, 68, 89].

Now, we need to integrate the source term. Combining contributions from the four intersecting cells, and approximating by the values at the centers of all the four intersecting cells [89] (see Fig. 3.1b), we obtain

$$\begin{aligned}
& \frac{1}{\Delta x \Delta y} \int_{t_n}^{t^{n+1}} \int_{x_p}^{x_{p+1}} \int_{y_q}^{y_{q+1}} s(x, y, t) dy dx dt \\
&= \frac{\Delta t}{4} \left\{ s \left( U_{p+1/4, q+1/4}^{n+1/2} \right) + s \left( U_{p+3/4, q+1/4}^{n+1/2} \right) \right. \\
&\quad \left. + s \left( U_{p+3/4, q+3/4}^{n+1/2} \right) + s \left( U_{p+1/4, q+3/4}^{n+1/2} \right) \right\}. \tag{3.15}
\end{aligned}$$

Using Taylor series expansion to compute the values of  $U_{p+1/4, q+1/4}^{n+1/2}$ , we get

$$U_{p+1/4, q+1/4}^{n+1/2} = U_{p, q}^{n+1/2} + \frac{\Delta x}{4} (\sigma^x)_{p, q}^n + \frac{\Delta y}{4} (\sigma^y)_{p, q}^n. \tag{3.16}$$

Hence, continuing in counterclockwise direction, all the arguments appearing in (3.15) are obtained as [89] :

$$\begin{aligned}
U_{p+1/4, q+1/4}^{n+1/2} &= U_{p, q}^{n+1/2} + \frac{\Delta x}{4} (\sigma^x)_{p, q}^n + \frac{\Delta y}{4} (\sigma^y)_{p, q}^n, \\
U_{p+3/4, q+1/4}^{n+1/2} &= U_{p+1, q}^{n+1/2} - \frac{\Delta x}{4} (\sigma^x)_{p+1, q}^n + \frac{\Delta y}{4} (\sigma^y)_{p+1, q}^n, \\
&\tag{3.17}
\end{aligned}$$

$$\begin{aligned}
U_{p+3/4, q+3/4}^{n+1/2} &= U_{p+1, q+1}^{n+1/2} - \frac{\Delta x}{4} (\sigma^x)_{p+1, q+1}^n - \frac{\Delta y}{4} (\sigma^y)_{p+1, q+1}^n, \\
U_{p+1/4, q+3/4}^{n+1/2} &= U_{p, q+1}^{n+1/2} + \frac{\Delta x}{4} (\sigma^x)_{p, q+1}^n - \frac{\Delta y}{4} (\sigma^y)_{p, q+1}^n.
\end{aligned}$$

**Corrector-Step:** Results from (3.9)-(3.10) and (3.11)-(3.12) indicate that the two dimensional NOC scheme has the first-order predictors (3.13), (3.17), and the second-order corrector steps, for the cell-mean value at the staggered grid point  $(x_{p+1/2}, q_{q+1/2}, t^{n+1})$  [89]

$$\begin{aligned}
& U_{p+1/2, q+1/2}^{n+1} \\
&= \frac{1}{4} \left\{ U_{p, q}^n + U_{p+1, q}^n + U_{p+1, q+1}^n + U_{p, q+1}^n \right\} \\
&+ \frac{\Delta x}{16} \left\{ \sigma_{p, q}^x - \sigma_{p+1, q}^x - \sigma_{p+1, q+1}^x + \sigma_{p, q+1}^x \right\} \\
&+ \frac{\Delta y}{16} \left\{ \sigma_{p, q}^y + \sigma_{p+1, q}^y - \sigma_{p+1, q+1}^y - \sigma_{p, q+1}^y \right\} \\
&- \frac{\Delta t}{2\Delta x} \left\{ f \left( U_{p+1, q}^{n+1/2} \right) + f \left( U_{p+1, q+1}^{n+1/2} \right) - f \left( U_{p, q}^{n+1/2} \right) - f \left( U_{p, q+1}^{n+1/2} \right) \right\} \\
&- \frac{\Delta t}{2\Delta y} \left\{ g \left( U_{p, q+1}^{n+1/2} \right) + g \left( U_{p+1, q+1}^{n+1/2} \right) - g \left( U_{p, q}^{n+1/2} \right) - g \left( U_{p+1, q}^{n+1/2} \right) \right\} \\
&+ \frac{\Delta t}{4} \left\{ s \left( U_{p+1/4, q+1/4}^{n+1/2} \right) + s \left( U_{p+3/4, q+1/4}^{n+1/2} \right) \right. \\
&\quad \left. + s \left( U_{p+3/4, q+3/4}^{n+1/2} \right) + s \left( U_{p+1/4, q+3/4}^{n+1/2} \right) \right\}. \tag{3.18}
\end{aligned}$$

The resulting scheme is a high-order accurate non-oscillatory, and also strongly depends on the reconstructed discrete slopes,  $\sigma^x$ ,  $\sigma^y$ ,  $\sigma^f$  and  $\sigma^g$ .

**CFL (Courant-Friedrich-Levy) Condition:** For the numerical stability, the scheme given by (3.13) and (3.18) must satisfy the CFL condition

$$\max \left( \frac{\Delta t}{\Delta x} \frac{\partial f}{\partial w}, \frac{\Delta t}{\Delta y} \frac{\partial g}{\partial w} \right) \leq 1/2. \quad (3.19)$$

The validity of this condition has been confirmed by numerical tests by Jiang and Tadmor [46] with the simple linear scalar advection equation [89].

### 3.4 Two-Dimensional Shock-Capturing Methods Applied to General Two-Phase Debris Flows

Here, we apply the two-dimensional NOC scheme discussed at §3.3 to the two-dimensional general two phase debris flows down an inclined channel proposed by Pudasaini (2012) [84]. We recall the model equations (2.24)-(2.29):

$$\begin{aligned} \frac{\partial}{\partial t}(\alpha_s h) + \frac{\partial}{\partial x}(\alpha_s h u_s) + \frac{\partial}{\partial y}(\alpha_s h v_s) &= 0, \\ \frac{\partial}{\partial t}(\alpha_f h) + \frac{\partial}{\partial x}(\alpha_f h u_f) + \frac{\partial}{\partial y}(\alpha_f h v_f) &= 0, \\ \frac{\partial}{\partial t} [\alpha_s h (u_s - \gamma \mathcal{C}(u_f - u_s))] + \frac{\partial}{\partial x} \left[ \alpha_s h \left( u_s^2 - \gamma \mathcal{C}(u_f^2 - u_s^2) + \frac{\beta_{x_s} h}{2} \right) \right] \\ + \frac{\partial}{\partial y} [\alpha_s h (u_s v_s - \gamma \mathcal{C}(u_f v_f - u_s v_s))] &= h S_{x_s}, \\ \frac{\partial}{\partial t} [\alpha_s h (v_s - \gamma \mathcal{C}(v_f - v_s))] + \frac{\partial}{\partial x} [\alpha_s h (u_s v_s - \gamma \mathcal{C}(u_f v_f - u_s v_s))] \\ + \frac{\partial}{\partial y} \left[ \alpha_s h \left( v_s^2 - \gamma \mathcal{C}(v_f^2 - v_s^2) + \frac{\beta_{y_s} h}{2} \right) \right] &= h S_{y_s}, \\ \frac{\partial}{\partial t} \left[ \alpha_f h \left( u_f + \frac{\alpha_s}{\alpha_f} \mathcal{C}(u_f - u_s) \right) \right] + \frac{\partial}{\partial x} \left[ \alpha_f h \left( u_f^2 + \frac{\alpha_s}{\alpha_f} \mathcal{C}(u_f^2 - u_s^2) + \frac{\beta_{x_f} h}{2} \right) \right] \\ + \frac{\partial}{\partial y} \left[ \alpha_f h \left( u_f v_f + \frac{\alpha_s}{\alpha_f} \mathcal{C}(u_f v_f - u_s v_s) \right) \right] &= h S_{x_f}, \\ \frac{\partial}{\partial t} \left[ \alpha_f h \left( v_f + \frac{\alpha_s}{\alpha_f} \mathcal{C}(v_f - v_s) \right) \right] + \frac{\partial}{\partial x} \left[ \alpha_f h \left( u_f v_f + \frac{\alpha_s}{\alpha_f} \mathcal{C}(u_f v_f - u_s v_s) \right) \right] \\ + \frac{\partial}{\partial y} \left[ \alpha_f h \left( v_f^2 + \frac{\alpha_s}{\alpha_f} \mathcal{C}(v_f^2 - v_s^2) + \frac{\beta_{y_f} h}{2} \right) \right] &= h S_{y_f}, \end{aligned}$$

where,

$$\beta_{x_s} = \varepsilon K_x p_{b_s}, \quad \beta_{y_s} = \varepsilon K_y p_{b_s}, \quad \beta_{x_f} = \beta_{y_f} = \varepsilon p_{b_f} \quad p_{b_f} = -g^z, \quad p_{b_s} = (1 - \gamma)p_{b_f},$$

with appropriate source terms  $s_{x_s}$ ,  $s_{x_f}$ ,  $s_{y_s}$  and  $s_{y_f}$ . These equations can be written in a compact vectorial form [84, 89]

$$\frac{\partial \mathbf{T}(\mathbf{w})}{\partial t} + \frac{\partial \mathbf{f}(\mathbf{w})}{\partial x} + \frac{\partial \mathbf{g}(\mathbf{w})}{\partial y} = \mathbf{s}(\mathbf{w}), \quad (3.20)$$

where,  $\mathbf{w}$  denotes the vector of conservative variables  $h_s, h_f, m_{x_s}(= h_s u_s), m_{x_f}(= h_f u_f), m_{y_s}(= h_s v_s)$  and  $m_{y_f}(= h_f v_f)$ ;  $\mathbf{T}$  is the vector of the virtual mass induced generalized conservative variables;  $\mathbf{f}$  and  $\mathbf{g}$  are the transport fluxes in the  $x$ - and  $y$ -directions, respectively, and  $\mathbf{s}$  denotes the source term, i.e.,

$$\mathbf{T}(\mathbf{w}) = \begin{pmatrix} h_s \\ h_f \\ m_{x_s} - \gamma \mathcal{C} \left( m_{x_f} h_s / h_f - m_{x_s} \right) \\ m_{y_s} - \gamma \mathcal{C} \left( m_{y_f} h_s / h_f - m_{y_s} \right) \\ m_{x_f} + \mathcal{C} \left( m_{x_f} h_s / h_f - m_{x_s} \right) \\ m_{y_f} + \mathcal{C} \left( m_{y_f} h_s / h_f - m_{y_s} \right) \end{pmatrix}, \quad \mathbf{w} = \begin{pmatrix} h_s \\ h_f \\ m_{x_s} \\ m_{y_s} \\ m_{x_f} \\ m_{y_f} \end{pmatrix},$$

$$\mathbf{f} = \begin{pmatrix} m_{x_s} \\ m_{x_f} \\ m_{x_s}^2 / h_s - \gamma \mathcal{C} \left( m_{x_f}^2 h_s / h_f^2 - m_{x_s}^2 / h_s \right) + \beta_{x_s} h_s h / 2 \\ m_{x_s} m_{y_s} / h_s - \gamma \mathcal{C} \left( m_{x_f} m_{y_f} h_s / h_f^2 - m_{x_s} m_{y_s} / h_s \right) \\ m_{x_f}^2 / h_f + \mathcal{C} \left( m_{x_f}^2 h_s / h_f^2 - m_{x_s}^2 / h_s \right) + \beta_{x_f} h_f h / 2 \\ m_{x_f} m_{y_f} / h_f + \mathcal{C} \left( m_{x_f} m_{y_f} h_s / h_f^2 - m_{x_s} m_{y_s} / h_s \right) \end{pmatrix},$$

$$\mathbf{g} = \begin{pmatrix} m_{y_s} \\ m_{y_f} \\ m_{x_s} m_{y_s} / h_s - \gamma \mathcal{C} \left( m_{x_f} m_{y_f} h_s / h_f^2 - m_{x_s} m_{y_s} / h_s \right) \\ m_{y_s}^2 / h_s - \gamma \mathcal{C} \left( m_{x_f}^2 h_s / h_f^2 - m_{y_s}^2 / h_s \right) + \beta_{y_s} h_s h / 2 \\ m_{x_f} m_{y_f} / h_f + \mathcal{C} \left( m_{x_f} m_{y_f} h_s / h_f^2 - m_{x_s} m_{y_s} / h_s \right) \\ m_{x_f}^2 / h_f + \mathcal{C} \left( m_{x_f}^2 h_s / h_f^2 - m_{y_s}^2 / h_s \right) + \beta_{y_f} h_f h / 2 \end{pmatrix}, \quad \mathbf{s} = \begin{pmatrix} 0 \\ 0 \\ h S_{x_s} \\ h S_{y_s} \\ h S_{x_f} \\ h S_{y_f} \end{pmatrix}, \quad (3.21)$$

where these expressions are computed in the conservative variables. The advantage of writing the two-phase debris flow model in standard, well-structured conservative form is

that the higher-order shock capturing (TVD-NOC) scheme can directly be applied to the model equation [84]. This is the main aim of this section.

From (3.18), the cell average  $\mathbf{w}_{p+1/2, q+1/2}^{n+1}$  at  $(x_{p+1/2}, y_{q+1/2}, t^{n+1})$  is given by [89]:

$$\begin{aligned}
& \mathbf{w}_{p+1/2, q+1/2}^{n+1} \\
&= \frac{1}{4} \left\{ \mathbf{w}_{p,q}^n + \mathbf{w}_{p+1,q}^n + \mathbf{w}_{p+1,q+1}^n + \mathbf{w}_{p,q+1}^n \right\} \\
&+ \frac{\Delta x}{16} \left\{ \mathbf{w}_{p,q}^x - \mathbf{w}_{p+1,q}^x - \mathbf{w}_{p+1,q+1}^x + \mathbf{w}_{p,q+1}^x \right\} \\
&+ \frac{\Delta y}{16} \left\{ \mathbf{w}_{p,q}^y + \mathbf{w}_{p+1,q}^y - \mathbf{w}_{p+1,q+1}^y - \mathbf{w}_{p,q+1}^y \right\} \\
&- \frac{\Delta t}{2\Delta x} \left\{ \mathbf{f} \left( \mathbf{w}_{p+1,q}^{n+1/2} \right) + \mathbf{f} \left( \mathbf{w}_{p+1,q+1}^{n+1/2} \right) - \mathbf{f} \left( \mathbf{w}_{p,q}^{n+1/2} \right) - \mathbf{f} \left( \mathbf{w}_{p,q+1}^{n+1/2} \right) \right\} \\
&- \frac{\Delta t}{2\Delta y} \left\{ \mathbf{g} \left( \mathbf{w}_{p,q+1}^{n+1/2} \right) + \mathbf{g} \left( \mathbf{w}_{p+1,q+1}^{n+1/2} \right) - \mathbf{g} \left( \mathbf{w}_{p,q}^{n+1/2} \right) - \mathbf{g} \left( \mathbf{w}_{p+1,q}^{n+1/2} \right) \right\} \\
&+ \frac{\Delta t}{4} \left\{ \mathbf{s} \left( \mathbf{w}_{p+1/4, q+1/4}^{n+1/2} \right) + \mathbf{s} \left( \mathbf{w}_{p+3/4, q+1/4}^{n+1/2} \right) \right. \\
&\quad \left. + \mathbf{s} \left( \mathbf{w}_{p+3/4, q+3/4}^{n+1/2} \right) + \mathbf{s} \left( \mathbf{w}_{p+1/4, q+3/4}^{n+1/2} \right) \right\}. \tag{3.22}
\end{aligned}$$

In (3.22),  $j = p, p + 1$  and  $k = q, q + 1$ , and

$$\mathbf{w}_{j,k}^x = \sigma_{j,k}^x, \quad \mathbf{w}_{j,k}^y = \sigma_{j,k}^y, \tag{3.23}$$

are the mean discrete derivatives over the cell in the  $x$ - and  $y$ -directions, respectively. The cell average at time level  $t^{n+1/2}$ , as in (3.13), is given by the conservation law (3.20):

$$\mathbf{w}_{j,k}^{n+1/2} = \mathbf{w}_{j,k}^n + \frac{\Delta t}{2} \left( \frac{\partial \mathbf{w}}{\partial t} \right)_{j,k}^n. \tag{3.24}$$

In (3.24), the derivative with respect to time is approximated by

$$\left( \frac{\partial \mathbf{w}}{\partial t} \right)_{j,k}^n = -(\sigma^{\mathbf{f}})_{j,k}^n - (\sigma^{\mathbf{g}})_{j,k}^n + \mathbf{s} \left( \mathbf{w}_{j,k}^n \right), \tag{3.25}$$

where,  $\sigma^{\mathbf{f}}$  and  $\sigma^{\mathbf{g}}$  are the one-dimensional discrete slopes of the fluxes.

If we use the cell reconstructions and the predicted values (3.24), then the arguments for the source term in (3.22) are given by [89]:

$$\begin{aligned}
\mathbf{w}_{p+1/4, q+1/4}^{n+1/2} &= \mathbf{w}_{p,q}^{n+1/2} + \frac{\Delta x}{4} \mathbf{w}_{p,q}^x + \frac{\Delta y}{4} \mathbf{w}_{p,q}^y, \\
\mathbf{w}_{p+3/4, q+1/4}^{n+1/2} &= \mathbf{w}_{p+1,q}^{n+1/2} - \frac{\Delta x}{4} \mathbf{w}_{p+1,q}^x + \frac{\Delta y}{4} \mathbf{w}_{p+1,q}^y, \\
\mathbf{w}_{p+3/4, q+3/4}^{n+1/2} &= \mathbf{w}_{p+1,q+1}^{n+1/2} - \frac{\Delta x}{4} \mathbf{w}_{p+1,q+1}^x - \frac{\Delta y}{4} \mathbf{w}_{p+1,q+1}^y, \\
\mathbf{w}_{p+1/4, q+3/4}^{n+1/2} &= \mathbf{w}_{p,q+1}^{n+1/2} + \frac{\Delta x}{4} \mathbf{w}_{p,q+1}^x - \frac{\Delta y}{4} \mathbf{w}_{p,q+1}^y.
\end{aligned} \tag{3.26}$$

**The CFL Condition:** The NOC scheme developed above must satisfy the CFL condition

$$\frac{\Delta t}{\Delta x} |C^{\max}| < \frac{1}{2}, \quad \text{for all } p, \quad (3.27)$$

with the possible global maximum wave speed

$$C^{\max} = \max\{C_s^{\max}, C_f^{\max}\}, \quad C_s^{\max} = \max\{\lambda_1, \lambda_2\}, \quad C_f^{\max} = \max\{\lambda_3, \lambda_4\},$$

over the whole computational domain (in the  $x$ -direction), where  $\lambda_{1,2}, \lambda_{3,4}$  are the associated wave speeds for the solid and the fluid phases in the two-phase mass flows:

$$\lambda_{(1,2)} = \frac{-g_1 \pm \sqrt{g_1^2 - 4h_1}}{2}, \quad (3.28)$$

$$\lambda_{(3,4)} = \frac{-g_2 \pm \sqrt{g_2^2 - 4h_2}}{2}, \quad (3.29)$$

where

$$g_{(1,2)} = \frac{a \pm \sqrt{a^2 - \frac{8b}{3} + 4y_s}}{2}, \quad (3.30)$$

$$h_{(1,2)} = \frac{y_s + \frac{b}{3} \pm \sqrt{\left(y_s + \frac{b}{3}\right)^2 - 4d}}{2}, \quad (3.31)$$

and,  $y_s$  is given by

$$y_s = 2 \left( \frac{a^2 d}{2} + \frac{c^2}{2} + \frac{b^3}{27} - \frac{abc}{6} - \frac{4bd}{3} \right)^{\frac{1}{3}}.$$

Here,  $a$ ,  $b$ ,  $c$  and  $d$  are given by

$$\begin{aligned} a &= -2(u_s + u_f), \\ b &= u_s^2 + 4u_s u_f + u_f^2 - h_s(\beta_{x_s} + 0.5\beta_{x_f}) - h_f(\beta_{x_f} + 0.5\beta_{x_s}), \\ c &= -2u_s u_f^2 - 2u_s^2 u_f + 2h_s \beta_{x_s} u_f + h_s \beta_{x_f} u_s + 2h_f \beta_{x_f} u_s + h_f \beta_{x_s} u_f, \\ d &= -0.5h_f \beta_{x_s} u_f^2 - h_s \beta_{x_s} u_f^2 - 0.5h_s \beta_{x_f} u_s^2 - h_f \beta_{x_f} u_s^2 + 0.5h_s^2 \beta_{x_s} \beta_{x_f} \\ &\quad + h_s h_f \beta_{x_s} \beta_{x_f} + 0.5h_f \beta_{x_s} \beta_{x_f} + u_s^2 u_f^2. \end{aligned}$$

For the computations of these general wave speeds, we refer to Pokhrel et al. (2014) [78]. One can obtain similar CFL condition with respective wave speeds in  $y$ -direction, too.

# Chapter 4

## Numerical Simulations of 3D, Two-Phase Debris Flows

In this chapter, we present the simulation results obtained by using the high resolution shock capturing TVD-NOC schemes (Chapter 3) to integrate the model equations (2.24)-(2.29) for a real two-phase debris flow down an inclined slope. We analyze the spatial and temporal evolution of the solid, fluid and total debris mass so as to explain the dynamics of two-phase debris flow in down-slope and cross slope directions. We mainly focus on the effects of the various physical aspects and parameters, including the friction angles, material densities, virtual mass, buoyancy, the drags and viscous forces. Simulation results reveal many basic and realistic features observed in two-phase debris flows in nature and laboratory, such as the typical development and evolution of the solid and fluid components, and also the dynamics and geometric form of the total debris bulk down the slope.

### 4.1 Simulation Set-up and Parameters

Landslides and debris flows are triggered to a larger extent depending upon different topographic, meteorological, and thermo-hydro-mechanical conditions. Some of the major factors contributing to the triggering and subsequent dynamics are the steepness, elevation, orientation, shape of the terrain and the amount of rainfall [89]. To model the topographic conditions, many generalizations have been presented in the past along with the different coordinate systems from one-dimension to three-dimensions with and without the curvature and the twist of the slope [24, 25, 30, 56, 65, 74, 88, 89, 90, 109].

In order to gain some fundamental insights into the dynamics of the real two-phase debris flows, here, we present some basic simulations on geometrically relatively simple inclined

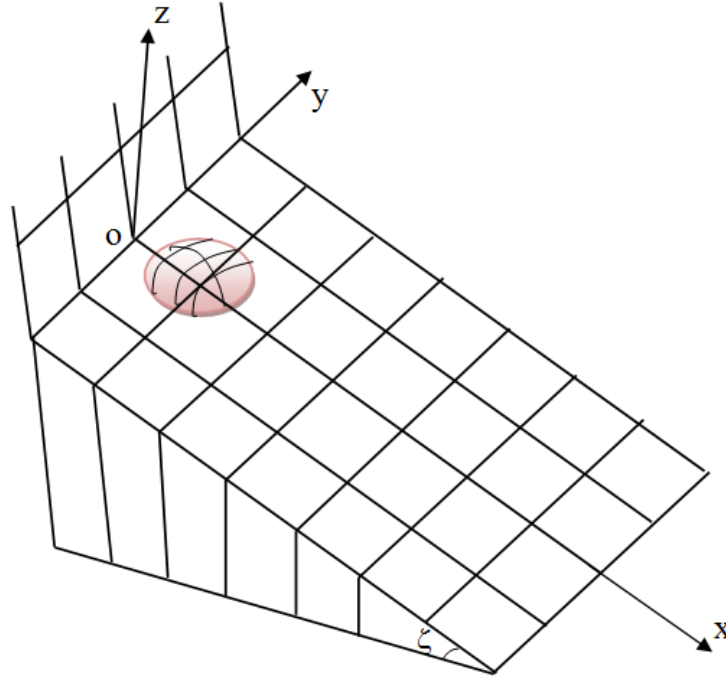


Figure 4.1: Simulation set-up and the slope-fitted coordinate system for a three-dimensional and two-phase debris mass moving down an inclined slope. Here,  $x, y, z$  are the coordinates along the down-slope, cross-slope and the surface normal directions, respectively, and  $\zeta$  is the slope angle. The hemispherical cap indicates the initial debris mass.

surface as shown in Fig. 4.1 in which the coordinates are aligned along the down-slope ( $x$ ) and cross-slope ( $y$ ) flow directions. The  $z$  coordinate is perpendicular to the surface made by the coordinate lines  $x$  and  $y$ . Initially, a homogeneous mixture of the two-phase debris mass is kept inside a hemispherical cap centered at point  $(x_0 = 23\text{ m}, y_0 = 0, z_0 = 0)$ . The channel inclination angle with the horizontal is  $\zeta$ . The height of the cap is 6.13 m and the radius of the cap is 15.32 m. The cap consists of about 64% solid and 36% fluid so as to represent a real two phase debris mass. The parameters involved in the model equations are grouped into the geometrical and material parameters.  $\phi$  is the collision angle between solid grains and is called the internal friction angle in equilibrium [83].  $\delta$  is the basal friction angle.  $\chi$  is a shape factor which includes vertical shearing of fluid velocity and we have taken  $\chi = 3$  [45, 94].  $K_x$  and  $K_y$  that are present in  $\beta$  are the  $x$  and  $y$  components of the earth pressure coefficient  $K$ , which is a soil mechanical parameter depending on  $\phi$  and  $\delta$ . When the flow is anisotropic, the value of  $K$  is derived from the soil mechanics theory. For simplicity, for isotropic, or extensional flows, one can also take  $K = 1$  [86].

Although the Reynolds number  $N_R$  and the mobility (or the quasi-Reynolds) number  $N_{RA}$  depend on different flow situations, in the simulations, following Pudasaini (2012) [84], we consider  $N_R = 300$  and  $N_{RA} = 14$ . We have taken the particle Reynolds number  $Re_p = 1$ , the terminal velocity of a particle  $\mathcal{U}_T = 1$ , the exponent of drag  $J = 1$  and the vertical distribution of solid volume fraction  $\xi = 5$ . Other parameters vary subject to different simulations.

## 4.2 Simulation Results and Discussion

Since the employed model equations are conservative in structure, numerical integration is possible even when the shocks are produced in the field variables [94, 109]. Model equations are applied for two-phase and three-dimensional debris flows down an inclined plane. Equations (2.24)-(2.29) are solved in conservative variables,  $\mathbf{w} = (h_s, h_f, m_s, m_f)^t$ , where  $h_s = \alpha_s h$  and  $h_f = \alpha_f h$  are the solid and fluid contributions in the total flow heights, and  $m_s = \alpha_s h u_s$ ,  $m_f = \alpha_f h u_f$  are solid and fluid momentum fluxes, respectively. To solve the model equations numerically, high-resolution, shock capturing, Total Variation Diminishing Non-oscillatory Central (TVD-NOC) scheme (Chapter 3) has been used [68, 89, 94, 109]. The model equations are integrated for a flow configuration in which debris mass is instantaneously released from a hemispherical cap and moves down an inclined plane, at an angle  $\zeta$  (Fig.4.1).

### 4.2.1 Geometry of the Solid, Fluid and the Total Debris Mass

Figure 4.2 describes the dynamics of the two-phase and three-dimensional debris flow moving down an inclined plane. Other parameter values are  $\rho_f = 1100 \text{ kgm}^{-3}$ ,  $\rho_s = 1500 \text{ kgm}^{-3}$ ,  $\mathcal{P} = 0.5$ ,  $\mathcal{C} = 0.2$ ,  $\zeta = 45^\circ$ ,  $\phi = 35^\circ$ , and  $\delta = 20^\circ$ . Here, we focus on analyzing the result at a particular time slice,  $t = 0.18 \text{ s}$ . The figures are produced by filling the gaps between contour lines and producing the colour maps to visualize the effective volume fraction of the solid (panel **a**), fluid (panel **b**) and the total debris material (panel **c**) [52, 53].

As soon as the hemispherical cap is opened, the debris mass collapses and starts moving down-slope. Then, both the solid and the fluid spread rapidly to both the front and the rear edges. Due to the very positive gradient (the slope of the hemispherical cap is about  $67^\circ$ ) of the trailing edge of the initial debris mass, some portion of the fluid (and also a bit of solid) flows back. Moreover, the drag evolves and increases due to the higher solid volume fraction in the central to frontal part of the debris mass. These are responsible for

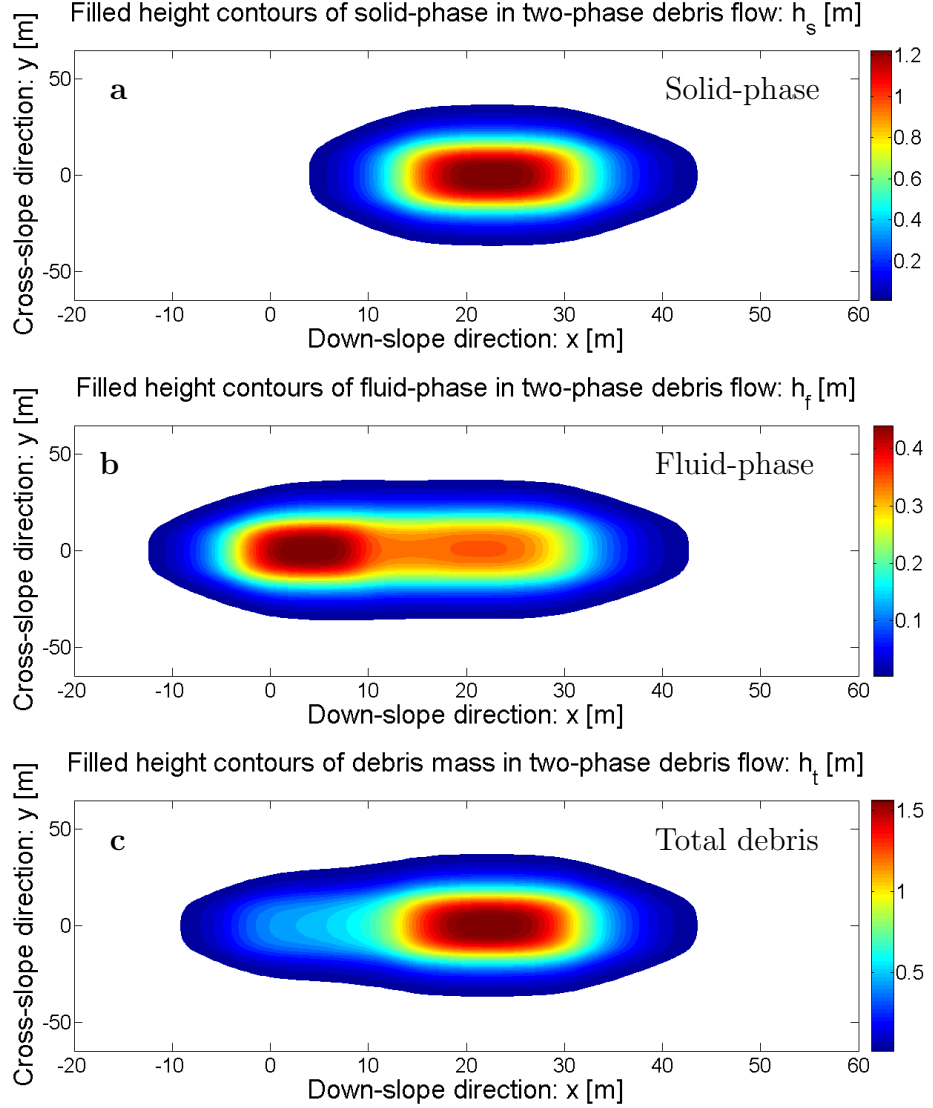


Figure 4.2: The three-dimensional geometry of the solid, fluid and total debris height at time  $t = 0.18$  s after the two-phase debris material is released from a hemispherical cap (Fig. 4.1) that moves down an inclined plane with inclination angle  $\zeta = 45^\circ$ ,  $\gamma = 1100/1500$ ,  $\mathcal{C} = 0.2$ ,  $\phi = 35^\circ$ ,  $\delta = 20^\circ$ ,  $\mathcal{P} = 0.5$ . It is important to observe that the solid and the fluid components evolve completely differently, both geometrically and dynamically.

the increased resistance of the fluid motion, thereby opposing the fluid movement through the solid matrix, mainly in the frontal part. Since the virtual mass force has also been considered, the kinetic energy of the fluid could have been changed [84].

Many interesting phenomena can be seen in Fig. 4.2. Although the initial debris material is a uniform and homogeneous mixture of the solid and the fluid, as the debris material

moves down, due to the strong solid-fluid interactions as prevailing in the model equations, the solid and the fluid volume fractions evolve strongly (during the dominant down-slope motion). As the mixture debris material slides down, it evolves into a typical dynamics for the solid (panel **a**) and the fluid (panel **b**). Comparing the panel **a** and panel **b** and viewing from the total debris material prospective (panel **c**), it is revealed that middle to the frontal part of the debris body is dominated by the solid fraction while the back-side consists of much more fluid than the solid. The fluid volume fraction or the fluid component (panel **b**) shows a double-surge, one in the middle-front and the other in the middle-back which is stronger than the first. Note that, although in the figures, the area covered by the colour map in the fluid panel seems to be larger than the area covered by the colour map in the total mass (panel **c**), the magnitude of the maximum colour depth in the fluid panel is much lower than the same in the total mass panel.

Another more interesting point is that, comparing panel **a** (solid) and panel **b** (fluid), and considering the very high (e.g., the maximum) concentration magnitude of the solid than the same for the fluid, we observe that in the total debris body (panel **c**), the middle-to-front part is clearly dominated by the solid volume fraction and that the middle-to-rear part is much more dominated by the fluid [53]. Furthermore, the three-dimensional geometric shape of the total debris body (panel **c**) reveals that a strong debris flow surge-head is quickly developed in the frontal part. And the debris height slowly decreases to the back forming a long tail. All these are observable phenomena in real two-phase debris flows in nature [45, 84, 94].

## 4.2.2 Effect of the Density Ratio

### A. Naturally Buoyant Flow:

Now, we present the simulation result for lower density ratio between the fluid and the solid mass. Figure 4.3 involves all the parameter values as that of Fig. 4.2 except now with more realistic density ratio,  $\gamma = 1100/2500$ . The solid and fluid masses, and thus the total debris mass, has been dispersed less in all directions. As  $\gamma$  decreases,  $(1 - \gamma)$  increases. This implies higher friction and higher drag. This means that the material behaves more like solid. This is the reason for the less spreading and reduced mobility. In this case, only a single fluid surge has been developed in the time slice  $t = 0.18$  s. As compared to Fig. 4.2, the flowing back of fluid is not that much substantial and that solid, fluid and total debris mass advect down-slope. As the solid volume fraction is higher than that of fluid in the initial debris mass, the flow dynamics of solid (panel **a**) and that of total debris bulk (panel **c**) seem to be similar. Importantly, in this naturally buoyant flow,

the friction, drag and pressure have been substantially decreased resulting substantially increased resistance of the flow in both directions.

### B. Neutrally Buoyant Flow:

It is interesting to analyze the neutrally buoyant flow (which corresponds to Bagnold) as shown in Fig. 4.4 with  $\gamma = 1100/1100$ . In this situation, the fluid and solid masses are largely dispersed as compared to the naturally buoyant flows in Fig. 4.3 and Fig. 4.2, both in the downstream and the cross-wise directions. This resulted in the decrease

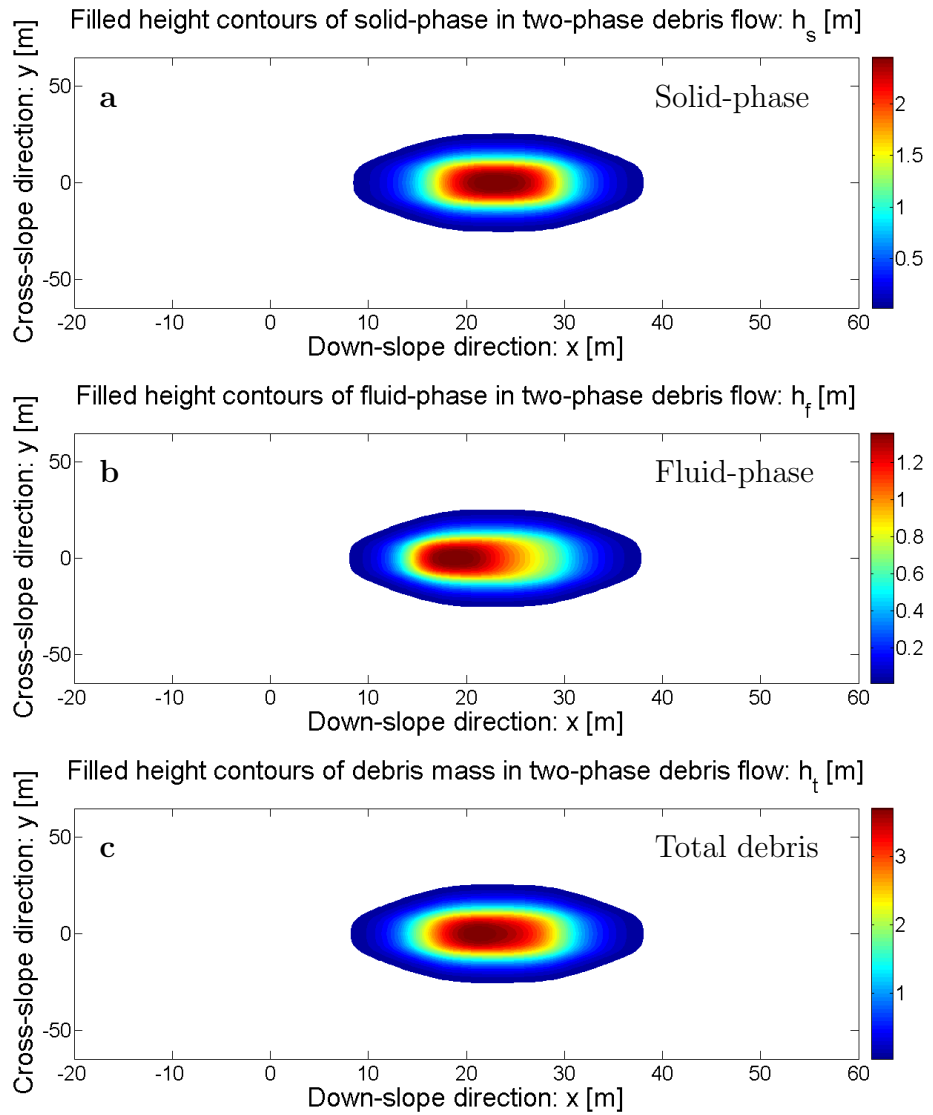


Figure 4.3: The three-dimensional geometry of the solid, fluid and total debris height at time  $t = 0.18$  s after the two-phase debris material is released from a hemispherical cap that moves down an inclined plane with inclination angle  $\zeta = 45^\circ$ ,  $\gamma = 1100/2500$ ,  $\mathcal{C} = 0.2$ ,  $\phi = 35^\circ$ ,  $\delta = 20^\circ$ ,  $\mathcal{P} = 0.5$ .

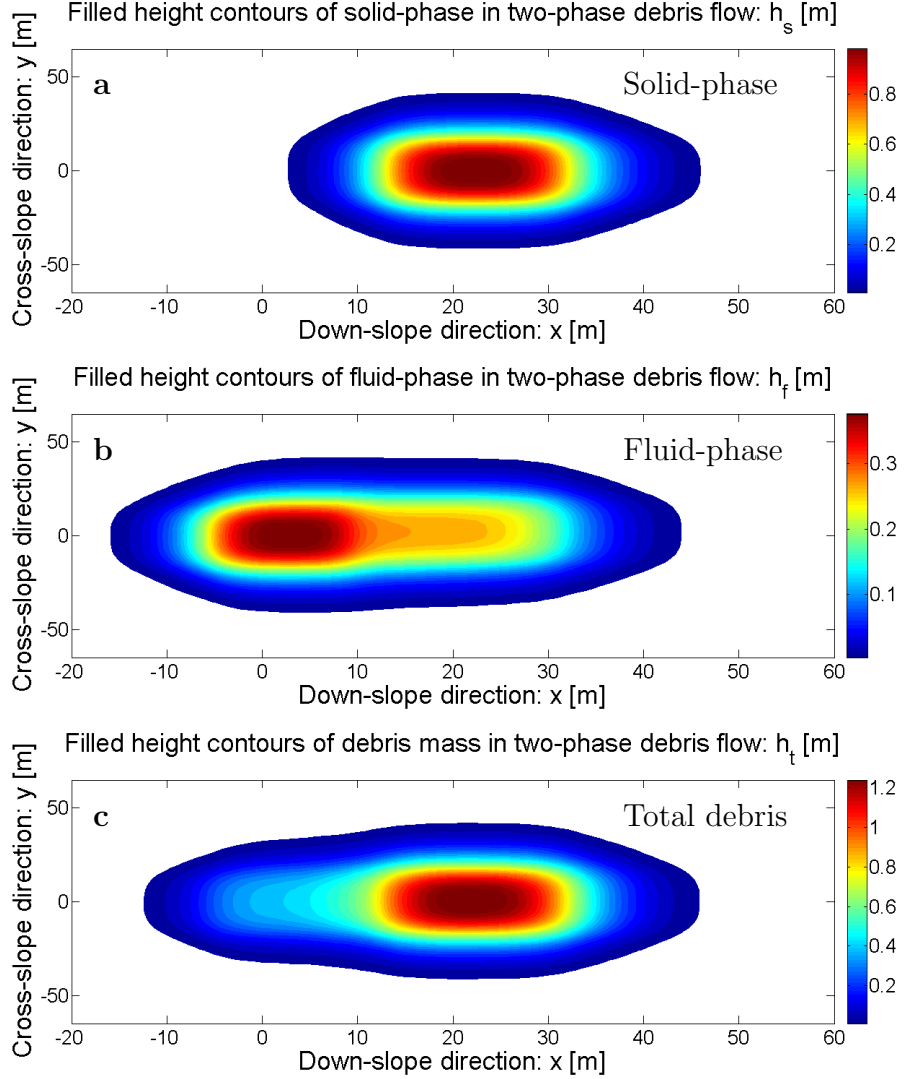


Figure 4.4: The three-dimensional geometry of the solid, fluid and total debris height at time  $t = 0.18$  s after the two-phase debris material is released from a hemispherical cap that moves down an inclined plane with inclination angle  $\zeta = 45^\circ$ ,  $\gamma = 1100/1100$ ,  $\mathcal{C} = 0.2$ ,  $\phi = 35^\circ$ ,  $\delta = 20^\circ$ ,  $\mathcal{P} = 0.5$ .

of both the solid and fluid heights, and thus, the total debris height. Since in neutrally buoyant flows, the frictions, e.g., in Coulomb and topographic pressure and also the drag, are largely reduced; this mobilizes the front of the debris bulk substantially farther, the tail lags behind and the flow is smoother when  $\gamma \rightarrow 1$ . As the debris bulk is fluidized, it travels longer distances with less dissipation of the frictional energy [84]. Although neutrally buoyant flows show largest mobility, naturally buoyant flows enhance the flow mobility, and the flows without buoyancy are substantially less mobile, the naturally buoyant flows, which appropriately describe the enhanced mobility in a real two-phase

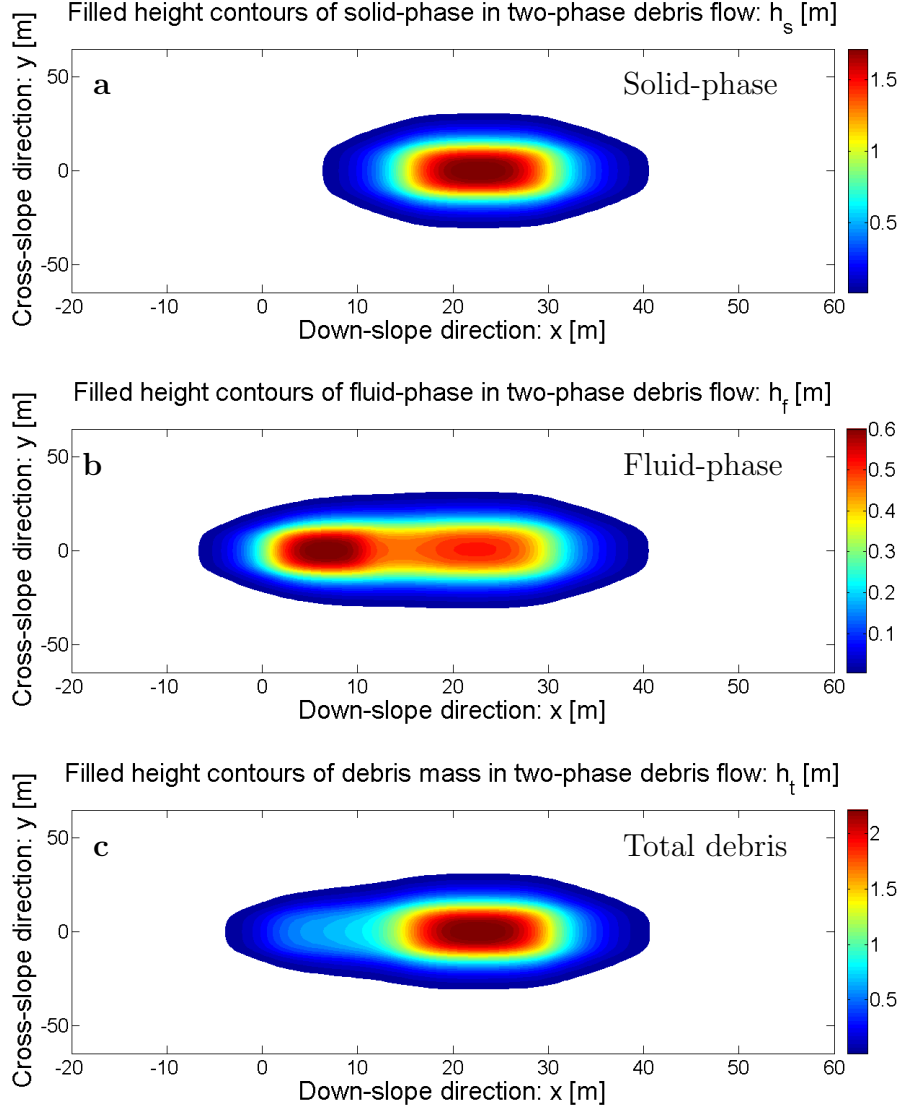


Figure 4.5: The three-dimensional geometry of the solid, fluid and total debris height at time  $t = 0.18$  s after the two-phase debris material is released from a hemispherical cap that moves down an inclined plane with inclination angle  $\zeta = 45^\circ$ ,  $\gamma = 1100/2000$ ,  $\mathcal{C} = 0.2$ ,  $\phi = 15^\circ$ ,  $\delta = 10^\circ$ ,  $\mathcal{P} = 0.5$ .

debris flow is more realistic [84, 91].

### 4.2.3 Effects of the Friction Parameters

Now, we decrease the friction parameters and keep other parameters as in Fig. 4.3 with the density ratio  $\gamma = 1100/2000$ ,  $\phi = 15^\circ$ ,  $\delta = 10^\circ$ ,  $\zeta = 45^\circ$ ,  $\mathcal{P} = 0.5$  and  $\mathcal{C} = 0.2$ . The results are shown in Fig. 4.5. Clearly, the fluid mass is more dispersed than the solid mass, now than in Fig. 4.3. The solid grains have less internal frictions (e.g., fine and

rounded solid grains) and the bed friction angle is also less (smooth channel bed) than in the previous figures. This represents a typical debris mass flow situation. The solid has the maximum flow height in the middle (panel **a**) but the fluid has dominant surge from middle to rear part and a small surge in the middle-front (panel **b**). However, the total debris bulk shows a densest strong head at the front and much less densest (more fluid than solid) and a long tail at the rear part. Such typical evolutions of the solid-dominated strong surge head followed by a largely fluid dominated, long and thin tail are often observed in natural debris flows [45, 53, 84, 94].

As compared with Fig. 4.5, the basal friction angle has been increased to  $\delta = 15^\circ$  in Fig. 4.8. This figures show that the basal friction angle has negative influence in the debris depth profile and geometry and mass distribution as a whole for both the solid, the fluid and the total debris mass. For smaller  $\delta$ , the solid mass can slide easily with less dissipation of frictional energy and less deformation. But for higher basal friction angle, the mass is relatively held by friction at the bed, thereby stretching and thinning the mass in downslope direction. The evolution and the increasing concentration of the fluid and the increasing concentration to the back is more pronounced in the rear part of Fig.4.8 than in Fig. 4.5 where  $\delta = 10^\circ$ . This can be explained, because as the mass is held relatively longer with the increased friction, and that the central part is dominated by the solid, this increases the drag. So, the fluid is compelled to be pushed and evolved in the rear part of the debris mass.

#### 4.2.4 Influence of Drag

Another important aspect in a real two-phase debris flow simulation is the influence of the drag. This is analyzed systematically in Fig. 4.6 and Fig. 4.7. In Fig. 4.6 and Fig. 4.7, where other parameters are the same as in Fig. 4.5, but, the drag interpolation parameter is chosen as  $\mathcal{P} = 0.9$  (Fig. 4.6), and  $\mathcal{P} = 0.1$  (Fig. 4.7), respectively. In Fig. 4.5,  $\mathcal{P} = 0.5$  was used. Figure 4.6 shows that, as the larger values of  $\mathcal{P}$  correspond to flow through the solid matrix, this induces more drag in the flow. Interestingly, due to the strong drag, the fluid has been strongly accumulated in the rear part of the debris body a very stronger fluid surge has been developed at the back (panel **b**). However, the total debris (panel **c**) again shows the densest frontal surge head, and that the tail is thin, elongated and fluidized (fluid dominated). But, in Fig. 4.7, nearly equally stronger double surges have been formed for the fluid component, one in the front and the other at the rear part. Otherwise, Fig. 4.5 and Fig. 4.7 show similar dynamical behaviour both for solid and fluid evolutions.

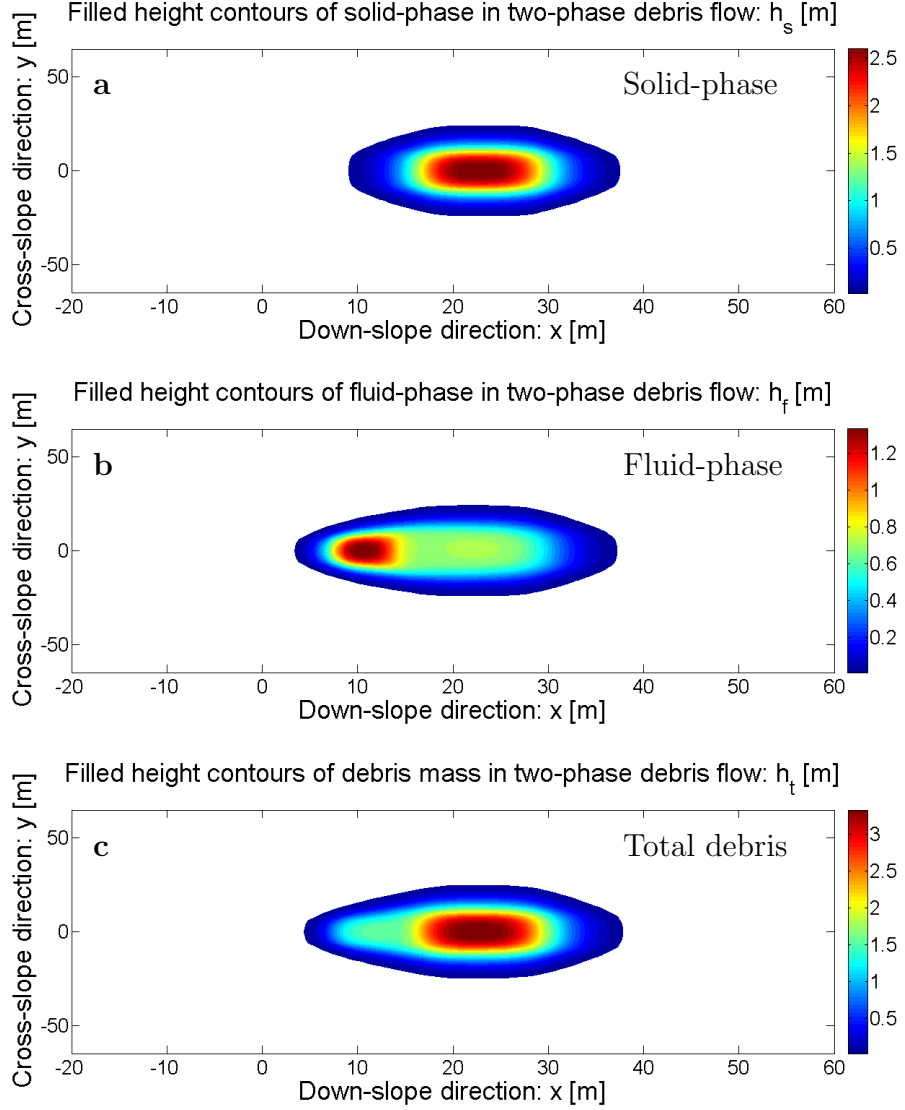


Figure 4.6: The three-dimensional geometry of the solid, fluid and total debris height at time  $t = 0.18$  s after the two-phase debris material is released from a hemispherical cap that moves down an inclined plane with inclination angle  $\zeta = 45^\circ$ ,  $\gamma = 1100/2000$ ,  $\mathcal{C} = 0.2$ ,  $\phi = 15^\circ$ ,  $\delta = 10^\circ$ ,  $\mathcal{P} = 0.9$ .

So, with the higher values of  $\mathcal{P}$ , i.e., the increased drag the advection of fluid in both directions (mainly in the down-slope direction) have been hindered contrary to the simulations with smaller values of  $\mathcal{P}$ . Hence, the drag interpolation parameter  $\mathcal{P}$  has negative effect in advection and the dispersion of the debris mass. But,  $\mathcal{P}$  has a positive effect in the height which follows from the mass balance. We mention that position and the solid, fluid and total debris mass distributions in Fig. 4.5 and Fig. 4.7 with  $\mathcal{P} = 0.5$  and  $\mathcal{P} = 0.1$  are similar; but these mass distributions in Fig. 4.6 are substantially different.

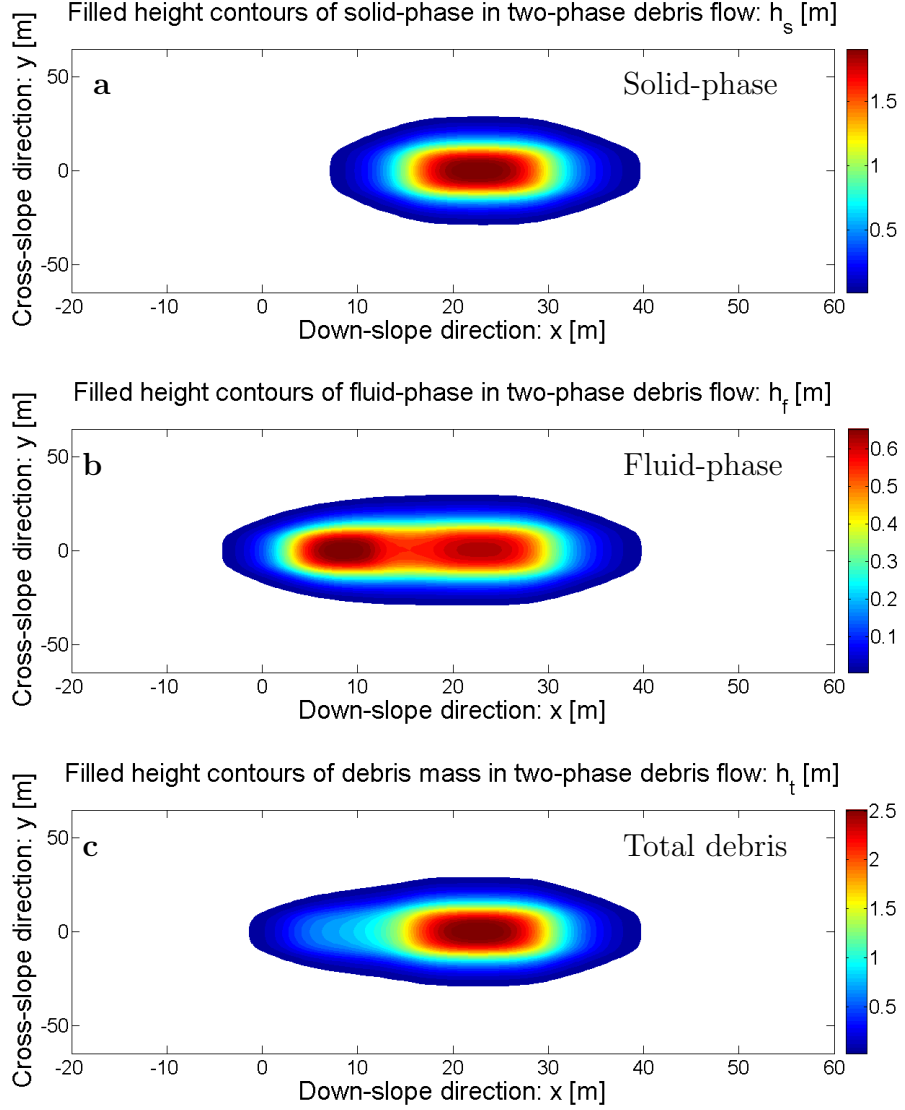


Figure 4.7: The three-dimensional geometry of the solid, fluid and total debris height at time  $t = 0.18$  s after the two-phase debris material is released from a hemispherical cap that moves down an inclined plane with inclination angle  $\zeta = 45^\circ$ ,  $\gamma = 1100/2000$ ,  $\mathcal{C} = 0.2$ ,  $\phi = 15^\circ$ ,  $\delta = 10^\circ$ ,  $\mathcal{P} = 0.1$ .

#### 4.2.5 Influence of the Virtual Mass

Next important aspect is the virtual mass coefficient that takes into account the increased kinetic energy of the ambient fluid due to the relative acceleration of the solid particle with respect to the fluid in the debris mixture. Figure 4.9 is produced with the virtual mass coefficient  $\mathcal{C} = 0.5$ , which is higher than in Fig. 4.5, where it was 0.2. The other parameters remain the same. In this situation, more fluid has been brought to the front in comparison to that in Fig. 4.5. Due to the higher virtual mass force, the fluid is also

advecting substantially (very less flowing back) in comparison to the other figures. The solid loses some inertia and it is relatively pushed back, mainly in the front. This results in the increased flow depth of the solid and fluid phases, and thus also of the total flow depth. This supports the fact that the solid mass brings along more fluid mass with them and the fluid is pumped to the front due to the increased virtual mass force [84].

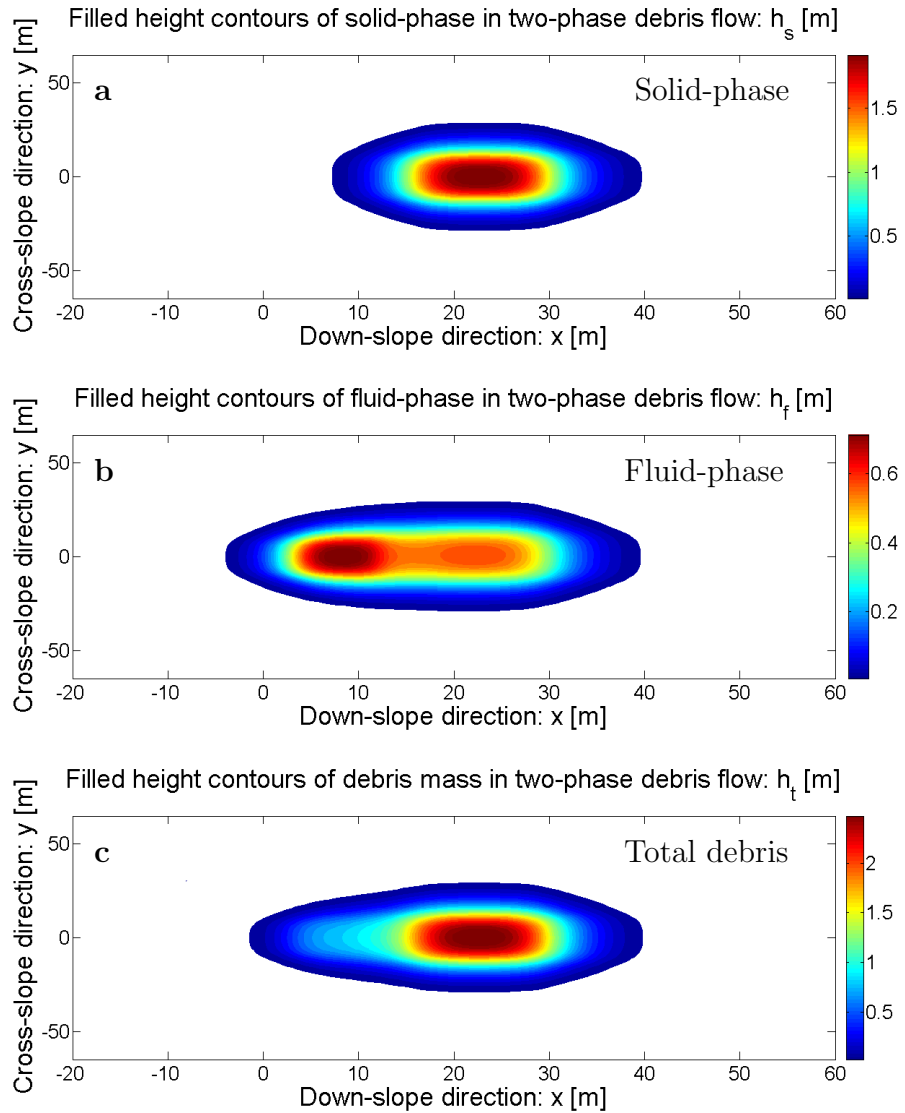


Figure 4.8: The three-dimensional geometry of the solid, fluid and total debris height at time  $t = 0.18$  s after the two-phase debris material is released from a hemispherical cap that moves down an inclined plane with inclination angle  $\zeta = 45^\circ$ ,  $\gamma = 1100/2000$ ,  $\mathcal{C} = 0.2$ ,  $\phi = 15^\circ$ ,  $\delta = 15^\circ$ ,  $\mathcal{P} = 0.5$ .

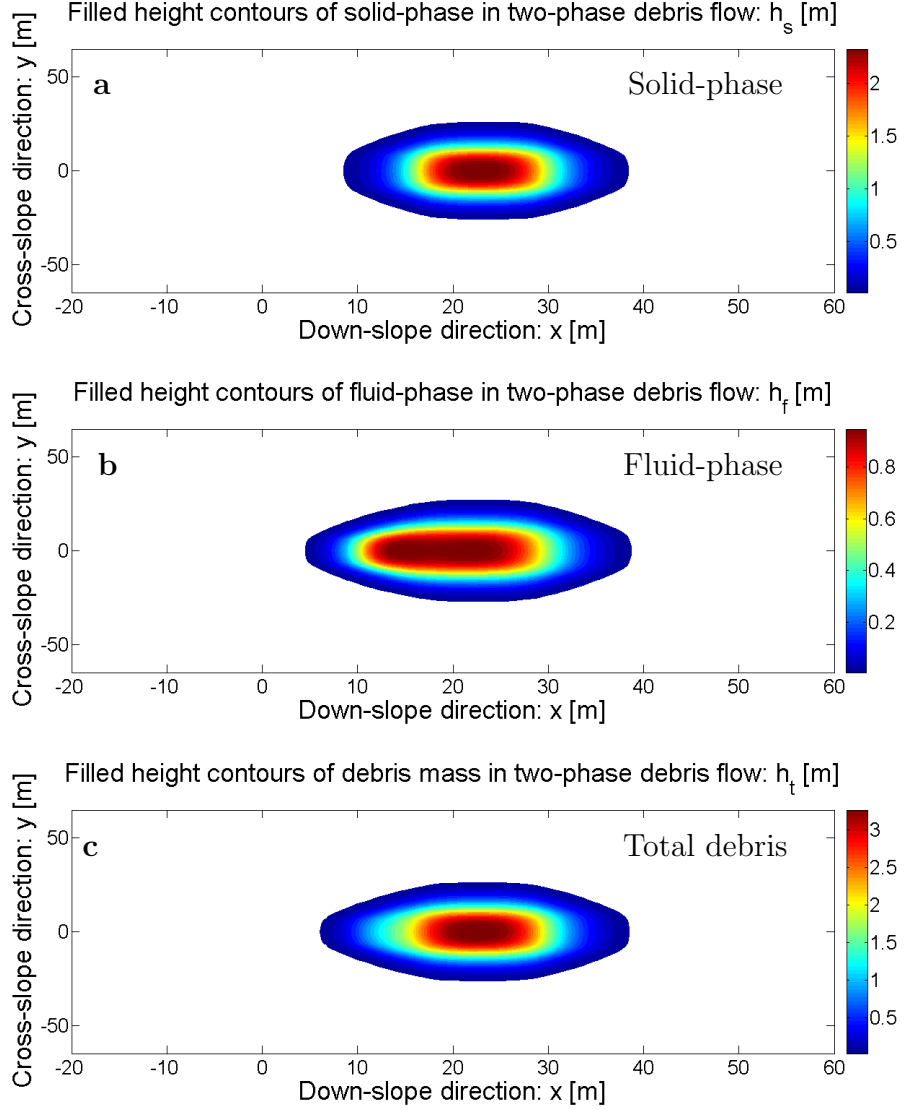


Figure 4.9: The three-dimensional geometry of the solid, fluid and total debris height at time  $t = 0.18$  s after the two-phase debris material is released from a hemispherical cap that moves down an inclined plane with inclination angle  $\zeta = 45^\circ$ ,  $\gamma = 1100/2000$ ,  $\mathcal{C} = 0.5$ ,  $\phi = 15^\circ$ ,  $\delta = 10^\circ$ ,  $\mathcal{P} = 0.5$ .

## 4.2.6 The Phase-Evolution

### A. Evolution of the Solid-Phase:

Perhaps, one of the most important aspects in the real two-phase debris flow simulation is the explicit, separate and simultaneous study of the time evolutions of the solid, fluid, and the total debris flow from the inception to the subsequent flows down-slope. The time evolution of the solid in different time slices:  $t = 0.006$  s,  $t = 0.06$  s,  $t = 0.12$  s and  $t = 0.18$  s is presented in Fig. 4.10. As the time elapses, the solid mass is dispersed in

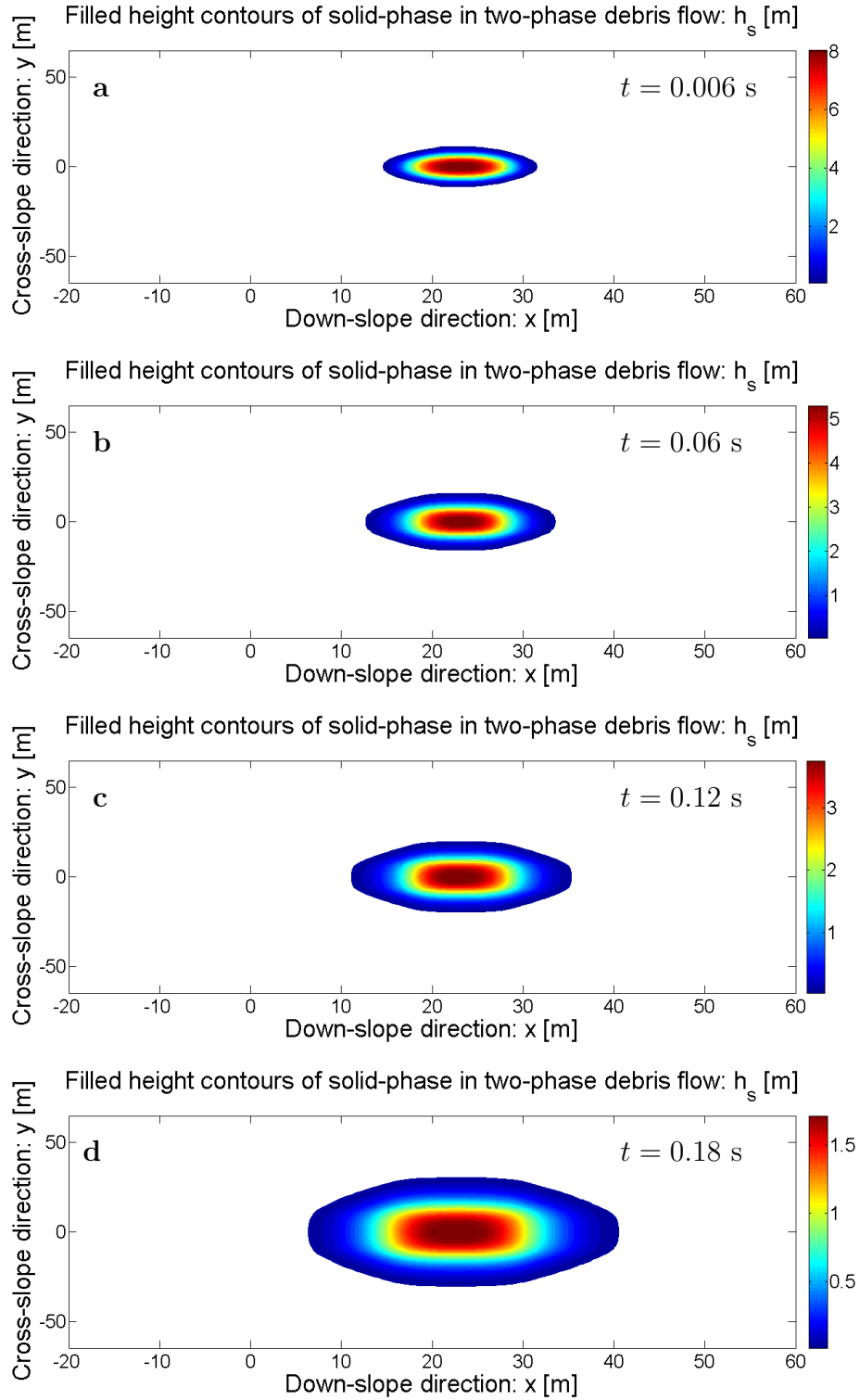


Figure 4.10: The evolution of the solid-phase at time slices:  $t = 0.006$  s,  $t = 0.06$  s,  $t = 0.12$  s and  $t = 0.18$  s after the two-phase debris material is released from a hemispherical cap that moves down an inclined plane with inclination angle  $\zeta = 45^\circ$ ,  $\gamma = 1100/2000$ ,  $\mathcal{C} = 0.2$ ,  $\phi = 15^\circ$ ,  $\delta = 10^\circ$ ,  $\mathcal{P} = 0.5$ .

all the directions and the solid heights are gradually decreasing. The solid mass is mainly stretching and cascading in the down-slope direction. However, a bit of solid is also moving back. This is due to the positive slope (in the back) of the free surface of the debris material in the initial configuration. The maximum of the solid height lies somewhere in the central part of the sliding mass, which is the characteristic of the solid deformation and the motion down a slope [94, 89].

### **B. Evolution of the Fluid-Phase:**

Another important point is to understand how the fluid component evolves, and how the fluid volume fraction is evolving as a two-phase debris mass slides down a slope. Figure 4.11 shows the time evolution of the fluid component. The fluid is also dispersing in all the flow directions. Nevertheless, the dispersion of the fluid is a bit more than solid, mainly, in the up-slope direction after  $t = 0.12$  s (panel **c**). A substantial part of the fluid is clearly advecting in down-slope direction, too. However, the interesting point here is that, as time elapses, the (relative) concentration of the fluid increases in the back, which is one of the major characteristics in a real two-phase debris flows that has been demonstrated here by considering a simple simulation based on the two-phase model equation due to Pudasaini (2012) [84]. The most striking aspect in Fig. 4.11 is the backward evolution of the fluid and the development of a strong fluid pocket, or the maximum surge in the rear part of the debris body. This special phenomenon clearly appears after  $t = 0.12$  s (panel **c**). As the solid and fluid mass in a debris flow show drastically different dynamics, a single phase or an effective single phase model may not be able to accurately describe debris flows.

### **C. Evolution of the Total Debris Bulk:**

Figure 4.12 shows the evolution of the total debris bulk in different time slices. The debris bulk, in aggregate, is advecting in the down-slope direction. The physically important aspect of this figure is the development of the total frontal surge head which increases quickly from the flow front, makes a peak in the middle-front, and the flow height decreases in the rear part, which is steadily decreasing, forming a long tail (panel **d**). The flow also disperses laterally. The surge shape stretches in down-slope direction and decreases in height as the time progresses and the flow travels further down-slope. The liquified tail (fluid component dominated) is highly elongated. It seems that the rear part takes some more time to move down-slope due to the support of the mass (mainly the solid) in the front and the material friction.

By applying the general two-phase mass flow model [84], and the high-resolution simu-

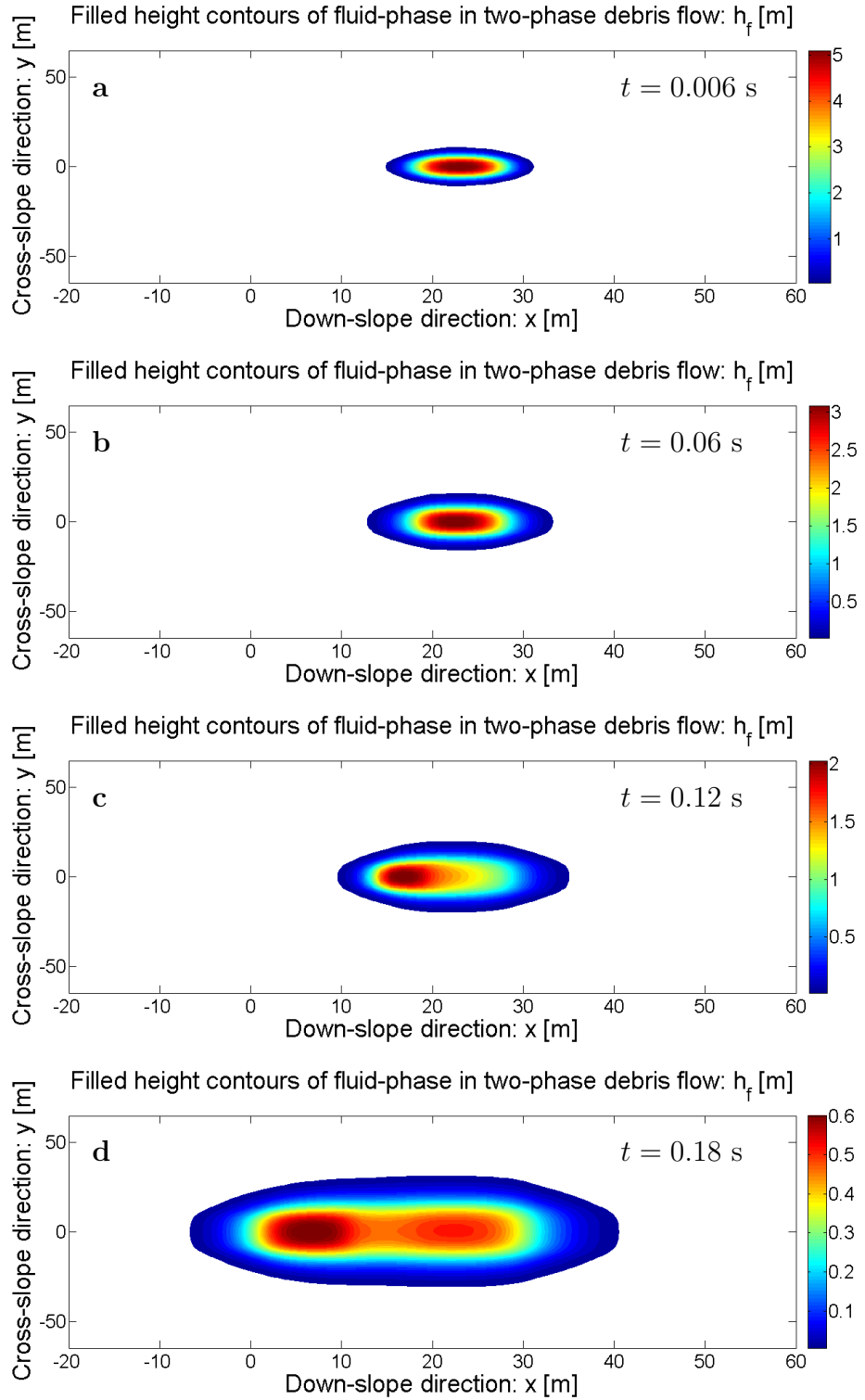


Figure 4.11: The evolution of the fluid-fluid at time slices:  $t = 0.006$  s,  $t = 0.06$  s,  $t = 0.12$  s and  $t = 0.18$  s after the two-phase debris material is released from a hemispherical cap that moves down an inclined plane with inclination angle  $\zeta = 45^\circ$ ,  $\gamma = 1100/2000$ ,  $\mathcal{C} = 0.2$ ,  $\phi = 15^\circ$ ,  $\delta = 10^\circ$ ,  $\mathcal{P} = 0.5$ .

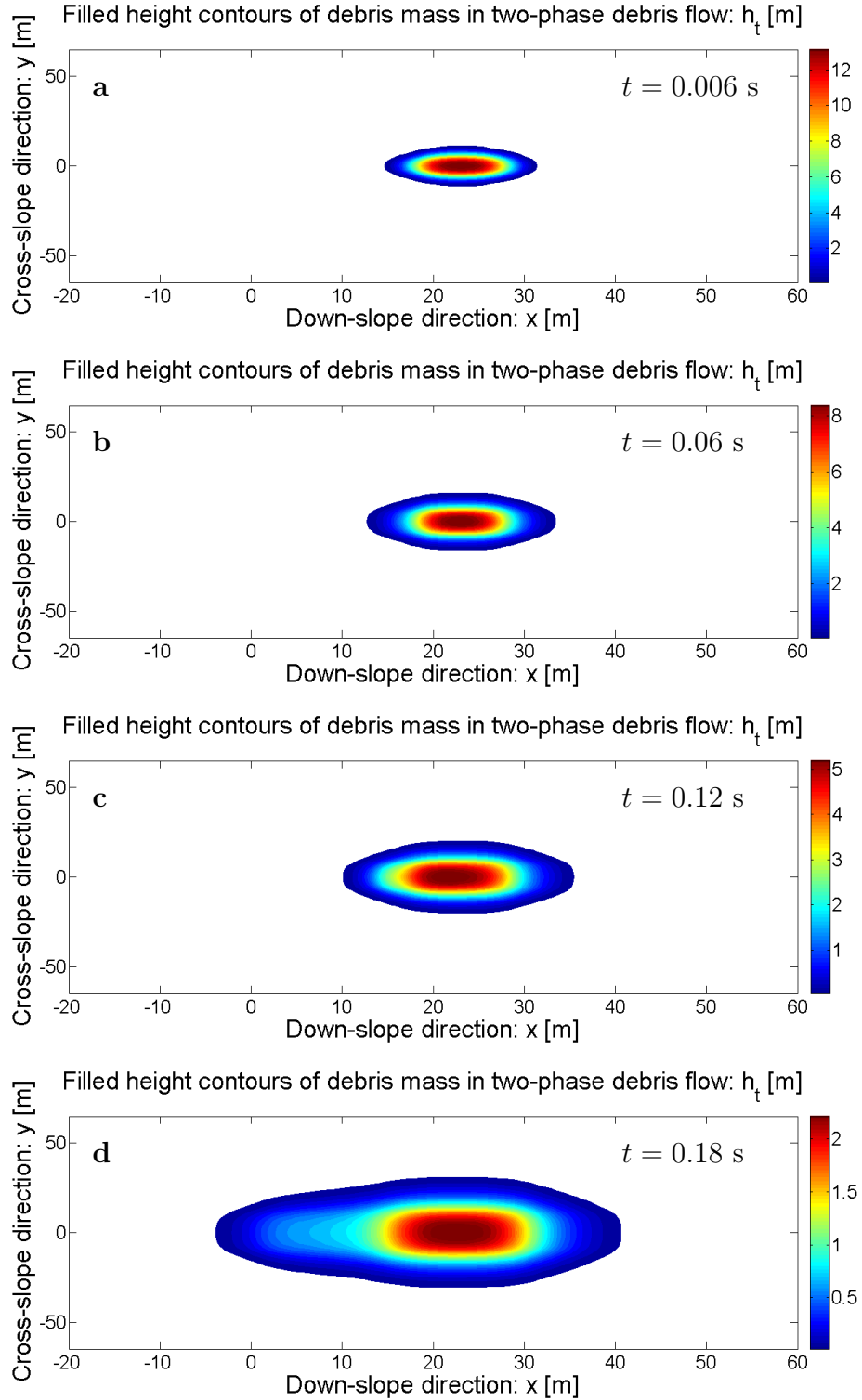


Figure 4.12: The evolution of the total debris mass at time slices:  $t = 0.006$  s,  $t = 0.06$  s,  $t = 0.12$  s and  $t = 0.18$  s after the two-phase debris material is released from a hemispherical cap that moves down an inclined plane with inclination angle  $\zeta = 45^\circ$ ,  $\gamma = 1100/2000$ ,  $\mathcal{C} = 0.2$ ,  $\phi = 15^\circ$ ,  $\delta = 10^\circ$ ,  $\mathcal{P} = 0.5$ .

lution tools [89], these basic simulation results are presented here for the first time for the three-dimensional and real two-phase debris flows in which explicit and simultaneous dynamic analyses have been carried out for both the solid, and the fluid components, and the total debris mixture as a whole. However, these simulations must be performed for different physical and geometrical parameters and for larger times. Further important aspect is to simulate the flow from the inception to the final deposition in the run-out zone. These simulations, when performed adequately, would form the basis for the application of the model and the simulation tool to the real two-phase and three dimensional debris flows in nature.

# Chapter 5

## Summary

In the beginning of the work, different types of geophysical mass flows and some examples of geo-hazards and their mitigation measures have been presented. Focus is made on the mass flow simulations. Mainly, a general two-phase debris-flow model proposed by Pudasaini (2012) [84] has been employed to simulate geometrically three-dimensional flow dynamics. Some features of the model equations and their reduction to other relatively simple models have been discussed. High-resolution shock-capturing numerical schemes with the Total Variation Diminishing Non Oscillatory Central Difference (TVD-NOC) method has been presented for the basic two-phase debris flow model. Novel simulation results have been presented for two-phase, and three-dimensional debris flows down an inclined slope that allows the flow to spread both in the down-slope and cross-slope directions. Simulations have been performed for different physical parameters, including the density ratio between the fluid and the solid phases, virtual mass coefficient, internal and basal friction angles, and the drag parameter that interpolates the solid- and fluid-like behaviour and the linear and quadratic drags. Simulation results reveal many fundamental physical phenomena that can be observed in real two-phase debris flows.

Simulation results show that, during the flow, the solid volume fraction dominates (the fluid volume fraction) in the middle-to-front part, whereas the fluid volume fraction dominates the middle-to-rear part of the debris body. However, this depends on the initial configuration, boundary conditions, and the evolving dynamics of the moving debris mixture. The simulation results show that the basal friction angle has negative influence in the debris depth profile. Moreover, with the increased virtual mass coefficient, the solid mass brings along more fluid mass with it and the fluid is pumped to the front. In the same way, for the larger values of the drag parameter, the fluid has strongly evolved and accumulated in the rear part of the debris body. In naturally buoyant flows, the total debris bulk shows a densest strong head at the front, and much less densest and a long tail

in the rear part. Importantly, a strong three-dimensional debris flow surge-head is developed quickly in the frontal part. Moreover, the height of the debris mass slowly decreases to the back, forming a long tail. These novel findings are consistent with observable phenomena in natural debris flows [45, 84, 94]. Among the different parameters considered here, the density ratio between the fluid and the solid mass in the debris material appear to be one of the most influential flow dynamical parameters. Also, we observed that the buoyancy has enhanced the mobility of debris mass. One of the most important aspects of this study is the simultaneous and separate simulations of the evolution of the solid, fluid and the total debris mass.

The basic simulation results presented here indicate the potential applicability of the full model equations (Pudasaini 2012) [84] and the unified computational strategy (Pudasaini and Miller, 2012b; Pudasaini, 2014) [85, 92] to adequately describe the complex dynamics of the real two-phase debris flows, avalanches, particle-laden, and dispersive flows in naturally three-dimensional slopes, channels and mountain topographies. Depending on the amount of the fluid in the initial and moving mass, phase interactions, and the overall dynamics of the mixture, the considered real two-phase mass flow model and the simulation strategies can directly be applied to a wide range of geophysical mass flows, including granular flows, snow and rock avalanches, and the flow of powders and grains in the pharmaceutical industries, as well as the debris flows and flash floods, including the GLOF, in mountain valleys and terrain regions.

The overall flow dynamics provides us with the different phase velocities, the effective density, the solid, fluid and total flow heights and several other physical aspects of the debris flows, from which we can calculate the momentum and the kinetic energy that the debris flows carry. With this, we can estimate the inundation areas in the hazard-prone zone and the dynamic impact of debris flow on civil structures in these areas. This allows us to properly construct advanced hazard mitigation planning, and enhanced safety measures against the potential natural disasters induced by landslides, debris flows, snow and rock avalanches and GLOF, that may be beneficial for the mountainous countries, like Nepal, with wide range of topographical variations and hazard potentials. Our results can be applied to appropriate mountain risk engineering, hazard mitigation and land use planning.

# Bibliography

- [1] C. Ancey. Plasticity and geophysical flows: A review. *J. Non-Newtonian Fluid Mech.*, 142(1-3):4–35, 2007.
- [2] M. Arattano, L. Franzi, and L. Marchi. Influence of rheology on debris flow simulation. *Nat. Hazards Earth Syst. Sci.*, 6:519–528, 2006.
- [3] R. Awal, H. Nakagawa, M. K. Fujita, Y. Baba, and H. Zhang. Experimental study on glacial lake outburst floods due to waves overtopping and erosion of moraine dam. *Annals of Disas. Prev. Res Inst. Kyoto University*, (53B):583–594, 2010.
- [4] R. A. Bagnold. Experiments on a gravity-free dispersion of large solid spheres in a Newtonian fluid under shear. *Proc. R. Soc. Lond., Ser. A*, 225:49–63, 1954.
- [5] S. R. Bajracharya and P. Mool. Glaciers, glacial lakes and glacial lake outburst floods in the Mount Everest Region, Nepal. *Annals of Glaciology*, 50(53):81–86, 2009.
- [6] N. J. Balmforth and I. Frigaard. Viscoplastic fluids: From theory to application. *J. Non-Newtonian Fluid Mech.*, 142:1–3, 2007.
- [7] N. P. Bhandary, R. K. Dahal, and M. Okamura. Preliminary understanding of the Seti River debris-flood in Pokhara, Nepal, on May 5th, 2012 - A report based on a quick field visit program. *ISSMGE Bulletin*, 6(4):9–18, 2012.
- [8] D. V. Boger and A. L. Halmos. *Non-Newtonian flow I- Characterization of fluid behaviour, Module C 2.1 American Institute of Chemical Engineers*. 1981. ISSN 0270-7632/81/1123-0001.
- [9] P. Brufau, P. Garcia-Navarro, P. Ghilardi, L. Natale, and F. Savi. 1D mathematical modelling of debris flow. *J. Hydraul. Res.*, 38(6):435–446, 2000. 435.
- [10] P. P. Cagueo, B. Turnbull, and B. Perry. Experiments on the dynamics of sub-aerial two-phase debris flows. *Geophysical Research Abstracts*, 15(3):237–258, 2013.

- [11] C. S. Campbell. Rapid granular flows. *Annu. Rev. Fluid Mech.*, 22:57–92, 1990.
- [12] C.L. Chen. Generalized viscoplastic modelling of debris flow. *J. Hydraul. Res.*, 114(3):237–258, 1988.
- [13] S. H. Chou, L. S. Lu, and S. S. Hsiau. Dem simulation of oblique shocks in gravity-driven granular flows with wedge obstacles. *Granular Matter*, 14:719–732, 2012.
- [14] P. Coussot and M. Meunier. Recognition, classification and mechanical description of debris flows. *Earth Science Reviews*, 40:209–227, 1997.
- [15] G. B. Crosta, S. Imposimato, and D. Roddeman. Numerical modelling of large landslides stability and runout. *Nat. Hazards Earth Syst. Sci.*, 3:523–538, 2003.
- [16] R. K. Dahal and N. P. Bhandary. *Excursion Guidebook for Kathmandu-Pokhara road (Prithvi Highway)*. The 11th International Symposium on Mitigation of Geodisasters in Asia (MGDA-11, Kathmandu, Nepal), Kathmandu, 2013.
- [17] A. Daido. On the occurrence of mud-debris flow. *Bull. Disas. Prev. Res. Inst.*, 21(187), 1971.
- [18] B. Domnik and S. P. Pudasaini. Full two-dimensional rapid chute flows of simple viscoplastic granular materials with a pressure-dependent dynamic slip-velocity and their numerical simulations. *J. Non-Newtonian Fluid of Mechanics*, 173-174:72–86, 2012.
- [19] B. Domnik, S. P. Pudasaini, R. Katzenbach, and S. A. Miller. Coupling of full two-dimensional and depth-averaged models for granular flows. *J. Non-Newtonian Fluid Mechanics*, 201:56–68, 2013.
- [20] D. A. Drew. Mathematical modelling of two-phase flow. *Ann. Rev. Fluid Mech.*, 15:261–291, 1983.
- [21] L. C. Evans. *Partial Differential Equations*. Providence: American Mathematical Society, 1998. ISBN 0-8218-0772-2.
- [22] T. Faug, B. Chanut, M. Naaim, and B. Perrin. Avalanches overflowing a dam: dead zone, granular bore and run-out shortening. *Annals of Glaciology*, 49:77–82, 2008a.
- [23] T. Faug, P. Gauer, K. Lied, and M. Naaim. Overrun length of avalanches overtopping catching dams: Cross-comparison of small-scale laboratory experiments and observations from full-scale avalanches. *Journal of Geophysical Research*, 113:F03009, 2008b.

- [24] E. D. Fernandez-Nieto, F. Bouchut, D. Bresch, M. J. Castro Daz, and A. Mangeney. A new Savage-Hutter type model for submarine avalanches and generated tsunami. *J. Comput. Phys.*, 227(16):7720–7754, 2008.
- [25] J. T. Fischer, J. Kowalski, and S. P. Pudasaini. Topographic curvature effects in applied avalanche modeling. *Cold Reg. Sci. Tech.*, 74-75:21–30, 2012.
- [26] M. Fort. Sporadic morphogenesis in a continental subduction setting: An example from Annapurna Range, Nepal Himalaya. *Z. Geomorph. N. F. Suppl.-Bd.*, 63:9–36, 1987.
- [27] Y. Forterre and O. Pouliquen. Flows of dense granular media. *Annu. Rev. Fluid Mech.*, 40:1–24, 2008.
- [28] R. W. Fox and A. McDonald. *Introduction to Fluid Mechanics*. Wiley, New York, 2001.
- [29] K. Fujita, A. Sakai, S. Takenaka, T. Nuimura, A. B. Surazakov, T. Sawagaki, and T. Yamanokuchi. Potential flood volume of Himalayan glacial lakes. *Nat. Hazards Earth Syst. Sci.*, 13:1827–1839, 2013.
- [30] J. M. N. T. Gray, M. Wieland, and K. Hutter. Gravity-driven free surface flow of granular avalanches over complex basal topography. *Proc. R. Soc. A*, 455:1841–1874, 1999.
- [31] R. Greve and K. Hutter. Motion of a granular avalanche in a convex and concave curved chute: Experiments and theoretical predictions. *Phil. Trans. R. Soc. A*, 342:573–600, 1993.
- [32] V. A. Hackley and C. F. Ferraris. *NIST Special Publication*, 946:1–31, 2001.
- [33] A. Harten. High resolution schemes for hyperbolic conservation laws. *J. Comput. Phys. Appl. Math.*, 49:357–393, 1983.
- [34] J. Huebl and H. Steinwendtner. Debris flow hazard assessment and risk mitigation, in: Felsbau. *Rock and Soil Engineering*, 1:17–23, 2000.
- [35] O. Hungr. A model for the run out analysis of rapid flow slides, debris flows, and avalanches. *Can. Geotechn. J.*, 32:610–623, 1995.
- [36] M. L. Hunt, R. Zenit, C. S. Campbell, and C. E. Brennen. Revisiting the 1954 suspension experiments of R. A. Bagnold. *J. Fluid Mech.*, 452:1–24, 2002.

- [37] K. Hutter and K. Jöhnk. *Continuum Methods of Physical Modeling: Continuum Mechanics, Dimensional Analysis, Turbulence*. Springer, Berlin, New York, 2004.
- [38] K. Hutter and L. Schneider. Important aspects in the formulation of solid-fluid debris-flow models. Part I. Thermodynamic implications. *Continuum Mech. Thermodyn.*, 22:363–390, 2010a.
- [39] K. Hutter and L. Schneider. Important aspects in the formulation of solid-fluid debris-flow models. Part II. Constitutive modelling. *Continuum Mech. Thermodyn.*, 22:391–411, 2010b.
- [40] K. Hutter, B. Svendsen, and D. Rickenmann. Debris flow modelling review. *Continuum Mech. Thermodyn.*, 8:1–35, 1996.
- [41] ICIMOD. *Glacial lakes and glacial lake outburst floods in Nepal*. ICIMOD, Kathmandu, 2011.
- [42] M. Ishii. *Thermo-Fluid Dynamic Theory of Two-Phase Flow*. Eyrolles, Paris, 1975.
- [43] M. Ishii and N. Zuber. Drag coefficient and relative velocity in bubbly, droplet or particulate flows. *AIChE J.*, 25:843–855, 1979.
- [44] R. M. Iverson. The physics of debris flows. *Rev. Geophys.*, 35(3):245–296, 1997.
- [45] R. M. Iverson and R. P. Denlinger. Flow of variably fluidized granular masses across three-dimensional terrain: 1. Coulomb mixture theory. *J. Geophys. Res.*, 106(B1):537–552, 2001.
- [46] G. S. Jiang and E. Tadmor. Nonoscillatory central schemes for multidimensional hyperbolic conservation laws. *SIAM J. Sci. Comput.*, 19:1892–1917, 1998.
- [47] A. M. Johnson. *A Model for Debris Flow*. Ph. D. Dissertation, Pa. State Univ., State College, 1965.
- [48] A. M. Johnson. *Physical processes in geology*. Freeman Cooper & Co., San Francisco, Calif, United States of America, 1970.
- [49] P. Jop, Y. Forterre, and O. Pouliquen. A constitutive law for dense granular flows. *Nature*, 441:727–730, 2006.
- [50] J. Kafle, P. Kattel, P. R. Pokhrel, K. B. Khattri, D. B. Gurung, and S. P. Pudasaini. Dynamic interactions between a two-phase submarine landslide and a fluid reservoir. *Int. J. Lsl. Env.*, 1(1):35–36, 2013.

- [51] J. Kafle, P. Kattel, P. R. Pokhrel, K. B. Khattri, D. B. Gurung, and S. P. Pudasaini. Dynamic interactions between a two-phase submarine landslide and a reservoir. 2014. (Submitted).
- [52] P. Kattel, J. Kafle, P. R. Pokhrel, K. B. Khattri, D. B. Gurung, and S. P. Pudasaini. Dynamics of three-dimensional, two-phase landslides and debris flows. *Int. J. Lslid. Env.*, 1(1):39–40, 2013.
- [53] P. Kattel, J. Kafle, P. R. Pokhrel, K. B. Khattri, D. B. Gurung, and S. P. Pudasaini. Dynamic simulations of three-dimensional, two-phase landslides and debris flows. 2014. (Submitted).
- [54] K. B. Khattri, P. R. Pokhrel, P. Kattel, J. Kafle, D. B. Gurung, and S. P. Pudasaini. Some new insights into the fluid flows in debris material and porous landscape. *Int. J. Lslid. Env.*, 1(1):39–40, 2013.
- [55] K. B. Khattri, P. R. Pokhrel, P. Kattel, J. Kafle, D. B. Gurung, and S. P. Pudasaini. Fluid flows in porous landscape and debris materials: Some new insights. 2014. (Submitted).
- [56] T. Koch, R. Greve, and K. Hutter. Unconfined flow of granular avalanches along a partly curved chute. II: Experiments and numerical computations. *Proc. R. Soc. A*, 445:415–435, 1994.
- [57] H. K. Kytoma. Viscous particle interactions and their effect on kinematic wave propagation. *Chem. Eng. Commun.*, 105(1):27–42, 1991.
- [58] P. Lax. Weak solutions of nonlinear hyperbolic equations and their numerical computation. *Comm. Pure Appl. Math.*, 7:159–193, 1954.
- [59] F. Legros. The mobility of long-runout landslides. *Eng. Geol.*, 63:301–331, 2002.
- [60] R. J. LeVeque. *Numerical Methods for Conservation Laws*. Birkhäuser, Basel, 1990.
- [61] K. A. Lie and S. Noelle. An improved quadrature rule for the flux-computation in staggered central difference schemes in multidimensions. *J. Sci. comp.*, 18:69–80, 2003.
- [62] C. E. Martinez. *Eulerian-Lagrangian two-phase debris flow model*. Ph. D. Dissertation, Florida International University, Miami, Florida, Nov. 2009.

- [63] C. E. Matrinez, F. Miralles-Wilhelm, and R. Garcia-Martinez. Quasi-three dimensional two-phase debris flow model accounting for boulder transport. *Italian Journal of Engineering Geology and Environment - Book*, 3:457–466, 2011.
- [64] B. W. McArdell, P. Bartelt, and J. Kowalski. Field observations of basal forces and fluid pore pressure in a debris flow. *Geophys. Res. Lett.*, 34:2009–2039, 2007.
- [65] M. Mergili, K. Schratz, A. Ostermann, and W. Fellin. Physically-based modelling of granular flows with Open Source GIS. *Nat. Hazards Earth Syst. Sci.*, 12:187–200, 2012.
- [66] GDR MiDi. On dense granular flows. *Eur. Phys. J. E*, 14(4):341–365, 2004.
- [67] M. Naaim, T. Faug, F. Naaim-Bouvet, and N. Eckert. Return period calculation and passive structure design at the Taconnaz Avalanche Path (France). *Annals of Glaciology*, 51(54):89–97, 2010.
- [68] H. Nessyahu and E. Tadmor. Non-oscillatory central differencing for hyperbolic conservation laws. *J. Comput. Phys.*, 87(2):408–463, 1990.
- [69] J. S. O’Brien and P. Y. Julien. Physical properties and mechanics of hyperconcentrated sediment flows. *ASCE Specialty Conference on the Delineation of Landslides, Floods and Debris Flows Hazards. ASCE, New York*, 260-279, 1985.
- [70] J. S. O’Brien, P. Y. Julien, and W. T. Fullerton. Two-dimensional water flood and mudflow simulation. *J. Hyd. Eng.*, 119(2):244–261, 1993.
- [71] M. Ouriemi, P. Aussillous, and E. Guazzelli. Sediment dynamics. Part 1: Bed-load transport by laminar shearing flows. *J. Fluid Mech.*, 636:295–319, 2009.
- [72] M. Pailha and O. Pouliquen. A two-phase flow description of the initiation of underwater granular avalanches. *J. Fluid Mech.*, 633:115–135, 2009.
- [73] D. A. Petrakov, O. V. Tutubalina, A. A. Aleinikov, S. S. Chernomorets, S. G. Evans, V. M. Kidyaeva, I. N. Krylenko, S. V. Norin, M. S. Shakhmina, and I. B. Seynova. Monitoring of Bashkara glacier lakes (Central Caucasus, Russia) and modelling of their potential outburst. *Nat Hazards*, 2011. doi: 10.1007/s11069-011-9983-5.
- [74] E. B. Pitman and L. Le. A two-fluid model for avalanche and debris flows. *Philos. Trans. R. Soc. A*, 363(3):1573–1602, 2005.

- [75] E. B. Pitman, A. K. Patra, D. Kumar, K. Nishimura, and J. Komori. Two phase simulations of glacial lake outburst flows. *J. Computational Science*, 4:71–79, 2013.
- [76] K. Platzter, P. Bartelt, and C. Jaedicke. Basal and shear normal stresses of dry wet snow avalanches after a slope deviation. *C. R. Acad. Sci. Paris*, 49:11–25, 2007.
- [77] P. R. Pokhrel, K. B. Khattri, P. Kattel, J. Kaffle, D. B. Gurung, and S. P. Pudasaini. Enhanced description of real two-phase landslides and debris flows. *Int. J. Lslid. Env.*, 1(1):75–76, 2013.
- [78] P. R. Pokhrel, K. B. Khattri, P. Kattel, J. Kaffle, D. B. Gurung, and S. P. Pudasaini. Real two-phase landslides and debris flows: Enhanced simulations. 2014. (Submitted).
- [79] A. D. Polyanin and V. F. Zaitsev. *Handbook of Nonlinear Partial Differential Equations*. 2004. ISBN 1-58488-355-3.
- [80] O. Pouliquen and Y. Forterre. Friction law for dense granular flows: Application to the motion of a mass down a rough inclined plane. *J. Fluid Mech.*, 453:133–151, 2002.
- [81] W. Prager and D.C. Drucker. Soil mechanics and plastic analysis or limit design. *Q. Appl. Math.*, 10(2):157–165, 1952.
- [82] S. P. Pudasaini. *Dynamics of Geophysical Mass Movements, Vol. I, and Vol. II*. 2007. Department of Geodynamics and Geophysics, University of Bonn, Germany (Lecture Notes).
- [83] S. P. Pudasaini. Some exact solutions for debris and avalanche flows. *Physics of Fluids*, 23(4):043301, 2011.
- [84] S. P. Pudasaini. A general two-phase debris flow model. *Journal of Geophysical Research*, 117:F03010, 2012. doi:10.1029/2011JF002186.
- [85] S. P. Pudasaini. Dynamics of submarine debris flow and tsunamis. *Acta Mechanica*, (Accepted) 2014.
- [86] S. P. Pudasaini and B. Domnik. Energy consideration in accelerating rapid shear granular flows. *Nonlin. Processes Geophys.*, 16:399–407, 2009.
- [87] S. P. Pudasaini, W. Eckart, and K. Hutter. Gravity-driven rapid shear flows of dry granular masses in helically curved and twisted channels. *Mathematical Models and Methods in Applied Sciences*, 13(7):1019–1052, 2003.

- [88] S. P. Pudasaini and K. Hutter. Rapid shear flows of dry granular masses down curved and twisted channels. *J. Fluid Mech.*, 495:193–208, 2003.
- [89] S. P. Pudasaini and K. Hutter. *Avalanche Dynamics: Dynamics of Rapid Flows of Dense Granular Avalanches*. Springer, Berlin, New York, 2007.
- [90] S. P. Pudasaini and M. Krautblatter. A real two-phase mechanical model for rock-ice avalanches. *Geophysical Research Abstracts*, 14, 2012. EGU2012-2660.
- [91] S. P. Pudasaini and S. A. Miller. Buoyancy Induced Mobility in Two-phase Debris Flow. *American Institute of Physics Proceedings*, 1479:149–152, 2012a.
- [92] S. P. Pudasaini and S. A. Miller. A real two-phase submarine debris flow and tsunami. *American Institute of Physics Proceedings*, 1479:197–200, 2012b.
- [93] S. P. Pudasaini and S. A. Miller. The hypermobility of huge landslides and avalanches. *Engineering Geology*, 157:124–132, 2013.
- [94] S. P. Pudasaini, Y. Wang, and K. Hutter. Modelling debris flows down general channels. *Nat. Hazards Earth Syst. Sci.*, 5:799–819, 2005.
- [95] M. E. Reid, R. M. Iverson, M. Logan, R. G. Lahusen, J. W. Godt, and J. P. Griswold. Entrainment of bed sediment by debris flows: Results from large-scale experiments. *Italian J. Eng. Geol. Env.*, 2011. doi: 10.4408/IJEGE.2011-03.B-042.
- [96] S. B. Savage and K. Hutter. The motion of a finite mass of granular material down a rough incline. *J. Fluid Mech.*, 199:177–215, 1989.
- [97] S. B. Savage and K. Hutter. Dynamics of avalanches of granular materials from initiation to run-out. Part I: Analysis. *Acta Mech.*, 86:201–223, 1991.
- [98] R. H. Sharma and R. Awal. Hydropower development in Nepal. *Renewable and Sustainable Energy Reviews*, 21(2):684–693, 2013.
- [99] A. B. Shrestha, M. Eriksson, P. Mool, P. Ghimire, B. Mishra, and N. R. Khanal. Glacial lake outburst flood risk assessment of Sun Koshi basin, Nepal. *Geomatics, Natural Hazards and Risk.*, 1(2):157–169, 2010.
- [100] L. E. Silbert, D. Ertas, G. S. Grest, T. C. Halsey, D. Levine, and S. J. Plimpton. Granular flow down an inclined plane: Bagnold scaling and rheology. *Phys. Rev. E*, 64(57):051302–1–151302–14, 2001.

- [101] A. H. P. Skelland. *Non-Newtonian Flow and Heat Transfer*. John Wiley and Sons Inc., 1967.
- [102] T. Sochi. *Pore-Scale Modeling of Non-Newtonian Flow in Porous Media*. Ph. D. Dissertation, Imperial College London, 2007.
- [103] M. Somos-Valenzuela and D. C. McKinney. Modeling a glacial lake outburst flood (GLOF) from Palcacocha Lake, Peru. Center for Research in Water Resources, The University of Texas at Austin, September 2011.
- [104] R. Sosio, G. B. Crosta, and O. Hungr. Complete dynamic modelling calibration for the Thuewieser rock avalanche (Italian Central Alps). *Eng. Geol.*, 100:11–26, 2008.
- [105] A. L. Strom and O. Korup. Extremely large rockslides and rock avalanches in the Tien Shan Mountains Kyrgyzstan. *Landslides*, 3:125–136, 2006.
- [106] Y. C. Tai. *Dynamics of Granular Avalanches and Their Simulations with Shock-capturing and Front-Tracking Numerical Schemes*. Ph. D. Dissertation, Darmstadt University of Technology, Darmstadt, Germany, 2000.
- [107] Y. C. Tai, J. M. N. T. Gray, K. Hutter, and S. Noelle. Flow of dense avalanches past obstructions. *Annals of Glaciology*, 32:281–284, 2001.
- [108] Y. C. Tai and C.Y. Kuo. A new model of granular flows over general topography with erosion and deposition. *Acta Mechanica*, 199:71–96, 2008.
- [109] Y. C. Tai, S. Noelle, J. M. N. T. Gray, and K. Hutter. Shock-capturing and front-tracking methods for granular avalanches. *J. Comput. Phys.*, 175:269–301, 2002.
- [110] T. Takahashi. The occurrence and flow mechanism of debris flow. *Tsuchi to Kiso*, 26:45–50, 1978.
- [111] T. Takahashi. Debris flow. *Annu. Rev. Fluid Mech.*, 13:57–77, 1981.
- [112] T. Takahashi. *Debris Flow*,. IAHR-AIRH Monograph Series A, Balkema, Rotterdam, Netherlands, 1991.
- [113] T. Takahashi. *Debris Flow: Mechanics, Prediction and Countermeasures*. Taylor and Francis, New York, 2007.
- [114] M. P. Tsai, Y. C. Hsu, H. C. Li, H. M. Shu, and K. F. Liu. Application of simulation technique on debris flow hazard zone delineation: A case study in the Daniao tribe, Eastern Taiwan. *Nat. Hazards Earth Syst. Sci.*, 11:3053–3062, 2011.

- [115] V. Vilmek, J. Klimes M. L. Zapata, Z. Patzelt, and N. Santillan. Influence of glacial retreat on natural hazards of the Palcacocha Lake area, Peru. *Landslides*, 2:107–115, 2005.
- [116] Y. Wang, K. Hutter, and S. P. Pudasaini. The Savage-Hutter Theory: a system of partial differential equations for avalanche flows of snow, debris and mud. *ZAMM*, 84(8):507–527, 2004.
- [117] M. Wieland, J. M. N. T. Gray, and K. Hutter. Channelized free surface flow of cohesionless granular avalanche in a chute with shallow lateral curvature. *J. Fluid. Mech.*, 392:73–100, 1999.
- [118] R. Worni, M. Stoffel, C. Huggel, C. Volz, A. Casteller, and Brian Luckman. Analysis and dynamic modeling of a moraine failure and glacier lake outburst flood at Ventisquero Negro, Patagonian Andes (Argentina). *Journal of Hydrology*, 444-445:134–145, 2012.
- [119] N. Zahibo, E. Pelinovsky, T. Talipova, and I. Nikolkina. Savage-Hutter model for avalanche dynamics in inclined channels: Analytical solutions. *J. Geophys. Res.*, 115, 2010. B03402, doi:10.1029/2009JB006515.
- [120] T. Zwinger, A. Kluwick, and P. Sampl. *Avalanche Flow of Dry Snow over Natural Terrain. Part II: Numerical Simulation*. In K. Hutter, N. Kirchner (eds): *Dynamic Response of Granular and Porous Materials under Large and Catastrophic Deformations*. Springer, Berlin, New York, 2003.